Skoltech
Skolkovo Institute of Science and Technology

Skolkovo Institute of Science and Technology

NANOSCALE PHASE SEPARATION AND TRANSFORMATIONS IN THE SILICON-OXYGEN AND RELATED SYSTEMS

Doctoral Thesis

by

PATRICK AGGREY

DOCTORAL PROGRAM IN MATERIALS SCIENCE AND ENGINEERING

Supervisor
Professor Alexander M. Korsunsky

Co-Supervisor
Dr. Alexey I. Salimon

Moscow - 2023

I hereby declare that the work presented in this thesis was carried out by myself at Skolkovo Institute of Science and Technology, Moscow, except where due acknowledgement is made, and has not been submitted for any other degree.

Candidate (Patrick Aggrey)

Supervisor (Prof. Alexander M. Korsunsky)

Abstract

The development of nanostructured silicon-based materials from siliceous precursors could address many challenges faced by their bulk counterparts, placing this area of research at the forefront of modern materials science and engineering. Despite the immense amount of work carried out to-date, further study is needed to address fully the issues related to material production and performance optimization via in-depth scrutiny of specific synthesis conditions. The present study considered the effects of thermally induced phase transformations in the Si-O system on the synthesis and properties of silicon-based nanomaterials in the form of powders and porous consolidates. The thermally induced transformations in diatom-derived silica carried out at 1100^oC led to significant variation in color, powder characteristics and phase composition, but the nanoporous network of diatom-derived silica was preserved after the thermal treatments. The roasted and calcined powders showed unclogged pores, reduced crystallite sizes and small surface areas. This combination of microstructural aspects made the materials suitable candidates for battery applications. Indeed, cyclic electrochemical testing as a negative electrode material in a Li-ion battery exhibited the discharge capacity of $255mAhg^{-1}$ for roasted powder-based anode and the discharge capacity of $340mAhg^{-1}$ for calcined powder-based anode, thus significantly superior to their amorphous counterpart value of $168mAhg^{-1}$.

The powder characteristics of nanostructured silicon produced via the Magnesiothermic Reduction Reaction (MRR) of pristine (amorphous) and calcined/roasted (crystalline) diatom-derived silica precursors were studied. Among all the silicon powders, the one recovered from the calcined silica precursor showed nano-scale morphology identical to that of the precursor powder and the smallest crystallite size (approximately 16nm). Interestingly, the crystalline silica powders showed lower onset and exothermic peak temperatures compared to their amorphous counterpart. As a result, the morphology of the Si powders recovered from crystalline silica showed more nanoscale features from their precursor than Si obtained from amorphous silica. Inspired

by this facile MRR route, a textured silicon surface was successfully created on a single crystal silicon wafer. This porous layer may offer a way to overcome structural stability concerns for silicon-based Lithium-ion battery anodes. Furthermore, the same porous layer could be overcoated with anti-reflective amorphous carbon films to reduce the surface reflectivity of silicon surfaces. Although significant progress has been reported in this area via the application of surface texturing techniques and photo-friendly thin film coatings, the advantage of the approach reported is that it combines two facile and environmentally safe synthesis processes to achieve optical properties comparable to those of black silicon (BSi).

In a further aspect of this study, a high purity silicon coating with the average thickness of 17µm was formed via the *in situ* magnesiothermic reduction reaction (MRR) of diatomaceous earth at $750^{o}C$ followed by phase separation between polyacrylonitrile (PAN)/tetraethyl orthosilicate (TEOS) to create porous amorphous carbon (a-C) film. These thin films were subsequently carbonized at $850^{o}C$ resulting in a textured porous Si/a-C film nanocomposite. Unlike textured silicon surfaces obtained by chemical etching of polished wafer, the new a-C coated textured silicon surfaces showed high broadband absorption in excess of 60% in the range 300-1700nm that compares extremely well with literature reports.

In summary, the work reported in this Thesis drew on a wide range of materials characterization techniques, and opened the possibilities for producing nanostructured silicon materials with a vast range of functionalities in a facile, eco-friendly and cost-effective way.

Publications

1. **Aggrey P**, Abdusatorov B, Kan Y, Salimon IA, Lipovskikh SA, Luchkin S, Zhigunov DM, Salimon AI, Korsunsky AM. *In situ formation of nanoporous silicon on a silicon wafer via the magnesiothermic reduction reaction (MRR) of diatomaceous earth.* Nanomaterials. 2020 Mar 25;10(4):601.

2. Korsunsky AM, Bedoshvili YD, Cvjetinovic J, **Aggrey P**, Dragnevski KI, Gorin DA, Salimon AI, Likhoshway YV. *Siliceous diatom frustules–A smart nanotechnology platform*. Materials Today: Proceedings. 2020 Jan 1;33:2032-40.

3. **Aggrey P**, Nartey M, Kan Y, Cvjetinovic J, Andrews A, Salimon AI, Dragnevski KI, Korsunsky AM. *On the diatomite-based nanostructure-preserving material synthesis for energy applications*. RSC advances. 2021;11(51):31884-922.

4. Salimon AI, Sapozhnikov PV, Everaerts J, Kalinina OY, Besnard C, Papadaki C, Cvjetinovic J, Statnik ES, Kan Y, **Aggrey P**, Kalyaev V. *A Mini-Atlas of diatom frustule electron microscopy images at different magnifications*. Materials Today: Proceedings. 2020 Jan 1;33:1924-33.

5. **Aggrey P**, Salimon AI, Abdusatorov B, Fedotov SS, Korsunsky AM. *The structure and phase composition of nano-silicon as a function of calcination conditions of diatomaceous earth*. Materials Today: Proceedings. 2020 Jan 1;33:1884-92.

6. **Aggrey, P**., Salimon, I. A., Salimon, A. I., Somov, P., Statnik, E., Zherebtsov, D., & Korsunsky, A. M. (2022). Tunable broadband absorption in continuous and porous textured Si/C bilayers: A comparative study. *Optical Materials*, *133*, 113048.

7. Salimon, A. I., Cvjetinovic, J., Kan, Y., Statnik, E. S., **Aggrey, P**., Somov, P. A., ... & Korsunsky, A. M. (2023). On the Mathematical Description of Diatom Algae: From Siliceous Exoskeleton Structure and Properties to Colony Growth Kinetics, and Prospective Nanoengineering Applications. *The Mathematical Biology of Diatoms*, 63-102.

Acknowledgements

Faithful is He who began this good work in me and has brought it to a successful end. I would like to express my profound gratitude to my scientific (Professor Alexander M. Korsunsky) and co-advisor (Dr Alexey I salimon) for their belief in me and full support during the entire PhD program. I would not have been able to complete this project without the support of colleagues in HSM and CEST. Lastly, big thanks to all family and friends who supported me in one way or the way during this program. Your support paid off. Thank you and God bless you all.

Table of Contents

List of Symbols, Abbreviations

DE – Diatomaceous Earth

MEMS – Microelectromechanical Systems

ARC – Anti-reflective Coating

PAN – Polyacrylonitrile

TEOS – Tetraethylorthosilicate

DMF – Dimethylformamide

THF – Tetrahydrofuran

DI – Deionized Water

EV – Electric Vehicle

MRR – Magnesiothermic Reduction Reaction /Metallothermic Reduction Reaction

TGA – Thermal Gravimetric Analysis

DSC – Differential Scanning Calorimtery

DTA – Differential Thermal Analysis

XRD – X-ray Diffraction

FIB – Focused Ion Beam

SEM – Scanning Electron Microscopy

AFM – Atomic Force Microscopy

KPFM – Kelvin Probe Microscopy

V_{CPD} – Contact Potential Difference

Si@PD – Silicon recovered from pristine diatom-derived silica

Si@CD – Silicon recovered from calcined diatom-derived silica

Si@RD – Silicon recovered from roasted diatom-derived silica

BSi – Black Silicon

c-Si – Bulk/mono/single crystalline Silicon

a-C – Amorphous carbon

Si@DE – Silicon recovered from Diatomaceous Earth

Si@SB – Silicon recovered from Silica Nanoballs

SSA – Specific Surface Area

IR – Infrared

VIS – Visible

SEI – Solid Electrolyte Interface

FFC Cambridge – Fray–Farthing–Chen Cambridge

PVDF – Polyvinylidene fluoride

List of Figures

13

14

15

List of Tables

Chapter 1. Introduction

The silicon-oxygen system arguably forms the backbone of the modern glass and ceramics technology. Silica and silicate materials and their related products found widespread applications across the breadth of technology, notably in the photovoltaic and semiconductor industries. The ready availability, high abundance, low cost, eco-friendliness and ease of processing are among the many advantageous attributes of these materials. However, certain shortcomings and challenges are encountered with bulk materials from this family that may limit their performance in optical, photovoltaic, electrochemical and other devices. This chapter discusses recently reported nanostructuring approaches and the significance of this processing route for silicon-based materials in energy related applications.

The challenges faced with silicon based solar cells and anode materials are related to their microstructure. The metallurgical grade of bulk silicon is widely used in the photovoltaic and semiconductor industry. However, the low reported photovoltaic efficiencies have been widely attributed to the weak light-matter interaction. In bulk silicon solar cells, undesirable surface reflections represent a major setback. As outlined below, the discovery of nanostructured silicon surfaces and anti-reflective coatings (ARC) allowed reducing unwanted surface reflections leading to significantly improved performance.

Although the very high lithiation capacity of silicon-based anodes makes them a potential game changer for electrochemical energy storage, in their bulk form they possess low mechanical stability due to very large expansion upon lithiation. Also in this regard, nanoscale structuring was found to be beneficial for optimizing the performance in silicon-based battery anodes and other energy applications. A summary of the recent progress in nanostructured silicon-based materials is presented and followed by an overview of the remaining thesis.

1.1 The Si-O System

The extraction of pure elements and their specific alloys from naturally occurring stable compounds has played a pivotal role in science and technology development over many years, especially the recovery of silicon-based materials from silica. Silicon dioxide (SiO_2), popularly known as silica or free silica is a type of silicate with only silicon and oxygen atoms. Free silica is the most common stable equilibrium compound in the Si-O system and makes up ca. 75wt.% of the earth crust [1]. On the binary Si-O pressure-temperature phase diagram shown in Figure 1, the presence of silica in several low- and high-pressure/temperature polymorphic phases is noted; *quartz, cristobalite, tridymite, coesite and stishovite.* Among these silica polymorphs, quartz is thermodynamically the most stable phase under ambient conditions and the major constituent of free silica, making up 12-14wt.% of the lithosphere [2]. A combination of excellent physical, chemical and mechanical properties makes quartz one of the most widely used materials in the Si-O system, with a broad spectrum of industrial applications [3-6]. Like quartz, the two high temperature silica polymorphs (cristobalite and tridymite) are also widely used in several industries such as cement replacement, glass ceramics, and road and building construction. As far as the high-pressure silica polymorphs (coesite and stishovite) are concerned, there is little information about their application due to their limited availability.

Over the last decades, a lot of attention has been given to silicon-based materials recovered from the Si-O system, including elemental silicon (Si). Pure Si is widely known for its application in solar cells, and as the backbone of the semi-conductor industry [8,9]. The fundamental part of modern technology hinges on the micro- and nano- chips made from the metallurgical grade of silicon. Unlike metals and non-metals which serve the purpose of electrical conduction or insulation only, conduction in semiconductor Si can be tuned to control electrical current. In practice, this is achieved by doping pure Si with elements such as phosphorus or boron. Aside from the fascinating semiconducting properties, Si is known to have very high theoretical capacity for

electrochemical energy storage [10], which makes it a perfect candidate for negative electrodes in lithium ion (Li-ion) batteries.
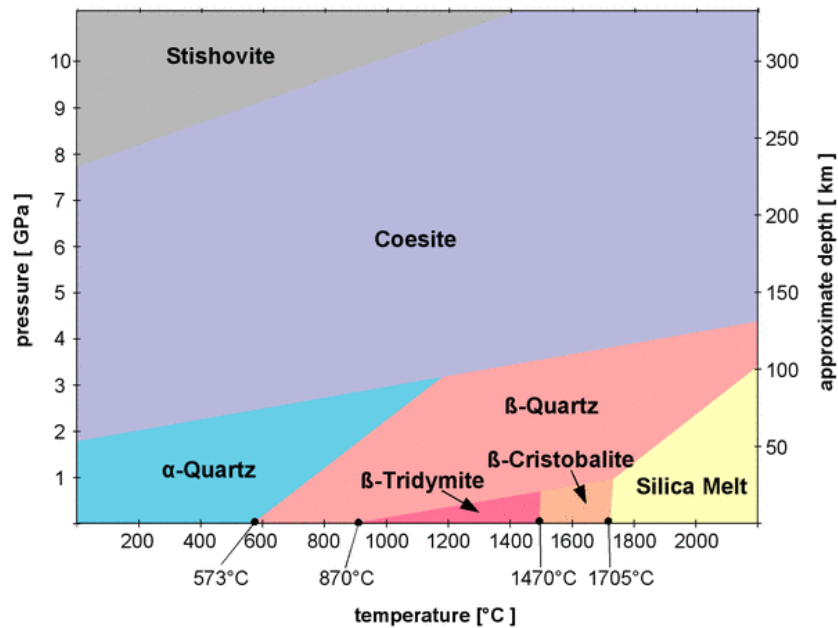
Figure 1 Binary Si-O pressure-temperature phase diagram [7]

Compared with the current commercial negative electrode, graphite, Si has a theoretical capacity an order of magnitude higher (4200mAh/g vs 372mAh/g) [10], but the process of lithiation is associated with several phase transformations and accompanied by very significant volume change that leads to the rapid fragmentation of Si anode. The attractiveness of using silicon in numerous applications can be understood by its ready availability at moderate price both in its purified form as single crystal wafers and polycrystals, and also after controlled doping with n- and p-type elements. Silicon-based devices can be made to possess a vast range of capabilities for sensing and detection, control, actuation, etc., along with eco-friendliness and ease of integration with other devices. Nevertheless, the use of silicon in applications such as solar cells, batteries and thermoelectric energy generators have witnessed some setbacks attributed to the lack of technological solutions for achieving specific nanoscale morphologies in bulk silicon [11-13]. In Si based anodes the threefold volume changes during lithiation (up to about

300% have been reported) lead to internal stresses, electrode pulverization, loss of electrical contact between the active material and the current collector, all of which eventually result in poor reversibility and rapid decline in capacity [14]. These setbacks are particularly characteristic of bulk silicon, but also apply to ball-milled Si obtained from bulk Si. For this reason, several attempts have been made to prepare nanostructured silicon-based anodes to harness the full potential of silicon in battery technology. These new approaches to nanostructuring Si-based anodes offer better accommodation of volume changes (strain gradients) from the surface to center as shown in Figure 2. As shown in Figure 2, ball-milled Si particles disintegrate during the lithiation process while the porous Si powder can accommodate the volume changes during lithiation.
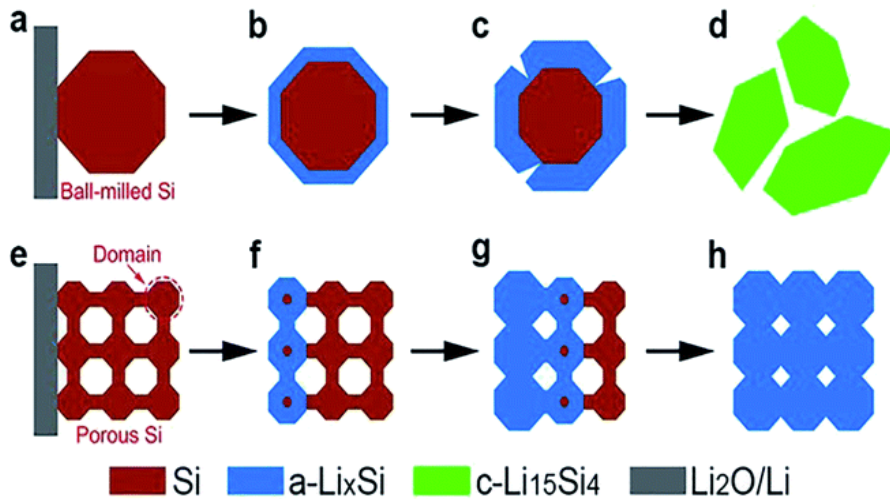
Figure 2 Schematic illustration of lithiation evolution in ball-milled Si and porous Si nanoparticles. (a–d) Response pattern of ball-milled Si from the surface-to-center during lithiation. (e–h) Response pattern of porous Si particle from the surface-to-center during lithiation [14].

Observations of similar kind have been reported for the potential use of bulk silicon as a thermoelectric material. Here also, bulk silicon has not found widespread applications due to the difficulty in generating a temperature gap across it. In a

21

semiconductor made up of covalent bonds efficient heat transfer occurs by lattice vibrations. This reduces the temperature gradient that can be achieved and thus limits the ability to generate significant voltage required in thermoelectrics. Once again, the nano-structuration of silicon has been studied as a way to resolve issues related to its potential use in thermoelectric energy generators [12,15-17].

The widespread use of bulk silicon is also reported in photovoltaic applications. In spite of this technology gaining great commercial attention, a number of drawbacks persist. Notable among these is the high surface reflectivity of silicon-based solar cells [18-20]. Progress has been reported in this area in a form of a number of review papers on the improved surface reflectance of silicon-based solar cells with a nanostructured surface [21-23].

All these reports point to the importance of silicon nano-structuration in energy applications. The approaches to nano-structuration proposed here focus on controlling the transformations within the Si-O system. The study of the interdependence of the structure, processing and property of materials emphasizes the need for a deeper understanding of the transformations within the Si-O system to obtain silicon-based materials with desired nano-scale morphologies to remedy the current challenges in battery storage, photovoltaics and other energy applications. This study seeks to identify and employ changes in the powder properties of diatom-derived silica after thermally-induced phase transformation for the production of silicon powder and consolidates for applications in battery storage and optical devices. The currently existing techniques for producing nano-silicon consolidates in the form of nano-wires, nano-sheets and nano-pillars are cost-intensive, require complex machinery set-up and often involves the use of expensive and harmful chemicals. The approach outlined in this study covers the direct use of thermal pre-treatments to modify diatom-derived silica powder properties for improved electrochemical performance of silica-based battery anodes and also optimize the chemical reduction of silica to nanostructured silicon powders as negative electrodes for Li-ion batteries. Another extension of the study presents a straightforward, cost-effective and eco-friendly path to producing nanostructured silicon coatings aimed at

improving the optical properties of their bulk counterpart and providing a suitable platform for other functional materials for photocatalysis, gas sensing and piezoelectric energy generation.

1.1.1 Transformations in the Si-O System

The equilibrium phases in the binary Si-O system are located in specific temperature and pressure regions beyond which transformation to other forms are possible. The phase transformations within the Si-O system have been well documented and specific temperatures and pressures necessary for such transitions are well detailed [7]. The most common equilibrium phase in this system is amorphous silica and the majority of phase transformation from this phase leads to different crystalline silica polymorphs at specific temperatures and pressures.

A classic example of the importance of phase transformations in the Si-O system is the crystallization of free silica to quartz. Quartz is widely used as piezo-sensors and in microelectromechanical systems (MEMS) due to its piezoelectric ability [24,25]. In the Si-O system, quartz is the only phase with a crystallographic orientation that induces the piezoelectric effect. Like quartz, cristobalite is reportedly the only silica polymorph that exhibits the auxetic effect [26]. These examples highlight the importance of phase transformation for materials development in the silicon-oxygen and related systems. To induce phase transformations in unary, binary or multi-component systems, specific temperatures and pressures are required. Apart from specific temperatures and pressures, the relationship between the lattice parameters of the parent and new phases is another important condition for phase transformations. Generally, phase transformations are more feasible when the parent and new phase show small lattice mismatch. For instance, the preferred transformation of opal-A ($SiO_2.nH_2O$), the main amorphous constituent of diatom-derived silica to cristobalite instead of tridymite at temperatures suitable for the latter has been attributed to the similar lattice parameters in both phases [27]. Most importantly, phase transformations are accompanied with physical and chemical changes in the material due to the high temperatures used. For example, to obtain cristobalite from

diatom-derived silica, high temperatures between 800-1200°C are typical required [27]. These high temperature treatments can purify the material by decomposing inorganic and organic impurities. Significant variations in volume, color, crystallite, pore and grain sizes are reportedly known to accompany phase transformations in material systems [28,29].

Lately, researchers have sought to exploit the accompanying effects of phase transformations as a way to modify materials properties for specific applications [30-33]. For most practical applications, performance is highly dependent on the physical and chemical properties of the material, particularly in the case of powders. As such, changes in these properties can affect performance to a large extent. A practical example is the case of thermal energy storage (TES) materials, where changes in the pore volume affect the absorption capacity of the supporting material [32,34]. Temperature induced phase transformations in materials are often accompanied with noticeable changes in the materials properties including pore size and volume. In porous powders such as diatom-derived silica, clogged pores have been reportedly unclogged using high temperature heat treatments. Apart from inducing phase transformations, the heat supplied is typically high enough to decompose most organic and inorganic impurities occupying these pores. Recently, this was observed in a study by Qian et al [35], where the absorption capacity of the supporting diatom-derived silica powder increased after calcination.

Besides porosities, the specific surface area, particle and crystallite sizes are other critical powder characteristics modified via heat treatments [28,29]. These powder characteristics are considered crucial for specific application where diffusion, adsorption and absorption are predominant. For instance, in lithium ion (Li-ion) batteries, a short lithium diffusion length is necessary to increase the charge/discharge rate capabilities [36]. This is known to be achievable through ultra-small particle and crystallite size of the active material and was recently demonstrated in a study by Blanco et al [37]. In their study, the electrochemical performance of diatom-derived silica based anode was remarkably improved by decreasing the particle size from 17μm to 470nm. The drastic decrease in particle size was achieved by mechanical means. While mechanical forces

provide quick and minimum energy to modify powder characteristics, it is only limited to particle size and surface area changes. Also, mechanical grinding/milling may not be an appropriate technique as far as the preservation of porosities is concerned. The reduction of particle size normally compromises the porous network. This may not be ideal for application where both porosities and small particle size are required.

The ability to change particle and crystallize sizes, surface areas, and crystal structure without substantial damage to the porous network of diatom-derived silica powders makes high temperature induced phase transformations in the Si-O system a fascinating area of study. Along with the direct effects of thermally-induced phase transformations on the silica powder characteristics, there could be indirect effects on the properties of silicon-based materials recovered from heat-treated silica precursors. It has been reported that the powder characteristics of silica precursors affect the properties of recovered Si to a large extent [29,38]. Although different silica precursors have been successfully reduced to silicon based materials, there is no study on the relationship between the chemical reduction kinetics of amorphous and crystalline forms of silica. An in-depth understanding of the effects of thermally-induced phase transformation on the kinetics of silica reduction reactions could provide an ideal technological solution to obtain silicon based materials with desired nanoscale features. For these reasons, it is imperative to investigate the effects thermally–induced phase transformations in the Si-O and related systems.

1.1.2 Silica Reduction and Related Materials

The recovery of elemental silicon and related silicon-based materials such as SiC, Mg_2Si, and SiGe with desirable nanoscale morphologies is crucial for the development of next generation materials for energy harvesting, conversion and storage. Emerging energy materials are required to possess nano- to micro- structures to meet several functionalities of specific applications. For instance, in lithium ion-batteries, silicon based anodes are required to deliver high capacity and structural stability, but presently that is not easily achievable. Silicon based materials with specific nanoscale

morphologies are highly sought after as far as structural stability in Li-ion batteries are concerned. A combination of good structural stability and high capacity can power the next generation of Li-ion batteries for full implementation in electric vehicles (EV's). Currently, the commercial graphite anode used is unable to provide enough energy density for EV's and future consumer electronics. Lots of chemical, thermal, electronic or mechanical challenges experienced during service operations have been attributed to the lack of nanoscale morphologies in bulk materials, incapable of addressing multi-functional task. Another notable example is the potential use of silicon as a thermoelectric material [12,15-17]. Apart from the widespread application of bulk silicon in photovoltaics and semi-conductors, it has received no practical application as far as thermoelectric energy generation. To generate energy using the thermoelectric effect, a temperature gradient is required which is impossible in silicon. Heat at one end is almost entirely transferred to the other end by lattice vibrations due to the nature of their chemical bonds. Without a significantly high temperature gradient, it is difficult to generate significant voltage in thermoelectrics. The introduction of nanoscale features in silicon has been reported as an effective heat transfer control measure to create temperature gradients required for thermoelectric energy generation [12,15-17]. These accounts highlight the need for synthesis techniques capable of producing silicon based materials with desired nanoscale morphologies.

Generally, silicon-based materials such as Si and SiC are produced via the carbothermal process [39-41] seen in Figure 3. This technique employs carbon as the reductant and reaction temperatures can go as high as 2200 °C. Although useful for the commercial production of high purity metallurgical grade of silicon, the carbothermal process is not highly regarded as the best approach to achieve nanoscale morphologies in silicon-based materials. This high temperature process poses a huge concern for silica precursors with nanoscale morphology. At high temperatures, particles may agglomerate and pores may disappear which leads to silicon-based materials without nanoscale features from the precursor.
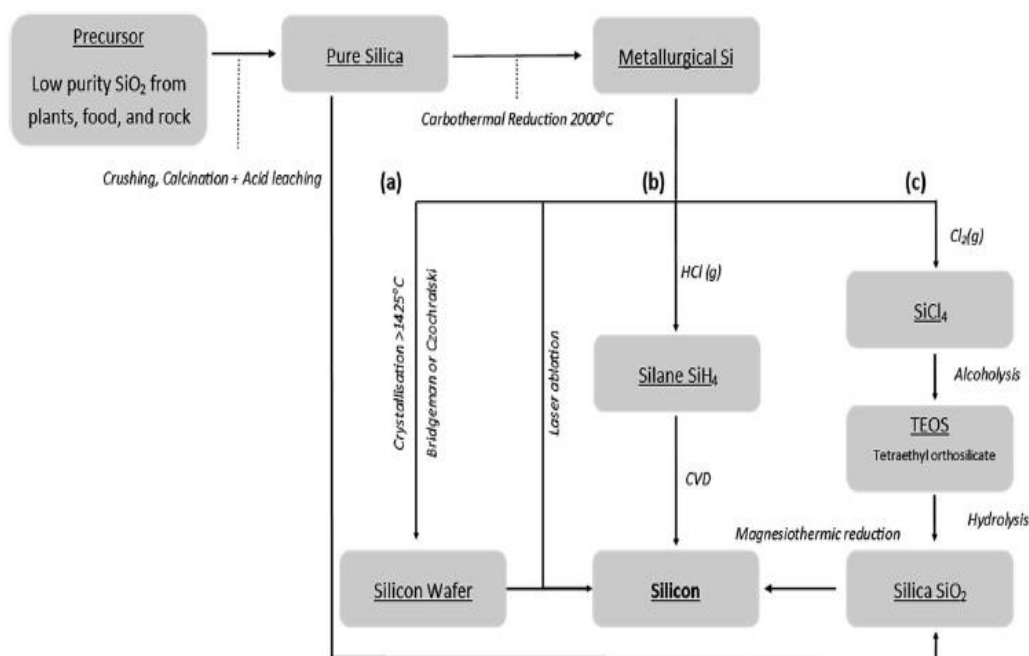
Figure 3 Flowchart of bulk silicon synthesis including magnesiothermic reduction

For these reasons, other forms of displacement reactions are highly sought after. This quest has witnessed a number of new synthesis techniques, with immense attention given to the metallothermic reduction reaction (MRR). A mini review by Xing *et al.* provides a historical view of the process and highlights current trends [42]. This displacement reaction type employs highly reactive metals to produce a wide range of products from stable compounds such as oxides, sulfides and halides. Materials obtained from the MRR are metals, alloys and composites. Typical reactive elements used in the MRR are lithium, sodium, magnesium, aluminum and intermetallics like Mg_2Si for the reduction of oxides and sulfides [42]. MRR is highly touted as an appropriate route to reduce diatom-derived silica and other silica precursors with nanoscale morphologies to nanostructured silicon-based materials due to the low synthesis temperatures desirable for the preservation of such morphologies. A number of different modifications to this technique have been recently reported, giving rise to the conventional and non-conventional MRR [43].

27

Lately, it has become increasingly important to understand the kinetics of metallothermic reduction reactions as a way to provide further control over the outcome of the synthesis process. Indeed, these studies have explored different reductants, temperatures, time, heat scavengers, and mixing ratio with interesting conclusions drawn from them [36]. As at the present time, very little is known about the exact onset temperature of metallothermic reduction of silica. There is also a lack of proper consensus on the ideal state of the silica precursor (crystalline or amorphous) as little to no information about their differences currently exist in literature. The re-arranging of bonds through displacive and reconstructive phase transformations is known to affect bond lengths and angles which eventually affect the materials bond strength. Additionally, the amorphous to crystalline transition in the Si-O system is accompanied with significant changes in the powder properties which could influence the chemical reduction kinetics to a some extent. Investigating this area of research in the Si-O system could provide a better understanding of the metallothermic reduction of silica and contribute immensely towards the production of silicon-based materials with desired nanoscale features.

1.2 Overall Aims of the Thesis

Considering the vast range of applications that benefit from the Si-O system, an in-depth understanding of the direct and indirect effects of thermally-induced phase transformation on the properties silica and recovered silicon-based materials remains a pivotal part in their industrialization. Recently reported effects of thermally-induced transformations have shown that such phenomena are accompanied with notable changes which could be exploited for the creation of materials with nanostructured functionalities that meet the requirements of modern and emerging technologies.

The aims of this study are to understand the effects of different heat treatments on silica powder characteristics, the chemical reduction of silica to silicon and the powder characteristics of recovered silicon based materials. The study seeks to answer some general questions below:

- What effects do the heating environments have on thermally-induced phase transformations in the Si-O system?

- How do thermally-induced phase transformations in the Si-O system affect the properties of recovered silicon-based materials?

- Does the structure of silica (crystalline or amorphous) affect the chemical reduction process (onset and peak temperature) and how does it influence the morphology of recovered silicon-based materials?

- What is the relationship between thermally-induced phase transformations and the performance of the silica and recovered silicon based materials (optical and electrochemical, etc.)

- Could metallothermic reduction of silica be exploited to create silicon nanostructures on substrates such as silicon wafer and how do their performance (optical / electrochemical properties) compare with their bulk counterparts?

Chapter 2 Literature Review

2.1 Theoretical Background

This chapter provides a brief review of the underlying literature which defines the scope of this study. It comprises literature on the principal material, protocols and their relevant application areas.

2.2 Hydrous Siliceous materials

Siliceous materials are present in many known forms and mainly consist of major phase silica with impurities such as metallic oxides and organics [44]. These include the three known crystalline polymorphs namely; quartz, cristobalite and tridymite, cryptocrystalline forms, fibrous forms, granular forms, hydrous and anhydrous forms. One type of the hydrous silica forms that has caught a lot of attention recently is diatomaceous earth (DE) due to it naturally formed neat nanoporous structure [45]. Otherwise known as diatom-derived silica or diatomite, DE is nature's perfect gift as far as the search for nanoporous silica precursors for silicon-based materials is concerned. DE is reported to be the only siliceous material with such neatly formed nanoporous network.

Diatom-derived silica and opal are known types of hydrated silica [29]. Diatom-derived silica (opal, $SiO_2 \cdot nH_2O$) is a naturally occurring and environmentally friendly siliceous sedimentary rock which is formed from the fossilized remains of diatom frustules [43]. Diatoms are single-celled aquatic algae which belong to the class of golden-brown algae [46]. Diatomite consists of almost entirely silica, with other components like alumina, and iron oxide. Although quite abundant throughout the world, it is difficult to come across pure diatomite. DE has interesting properties, which has inspired application in various fields. Some interesting properties of diatomite are low density, high porosity, high surface area, absorptive capacity, abrasiveness, insulating properties, inertness, and high silica content. Diatomite has found applications in fields like filtration, absorbents, functional additives, natural insecticide, and soil amendment

[43]. Other known application include dental fillings, seed coating, oil drilling compounds, adhesives, sealants, specialty concrete, and paper. As a good source of highly nanoporous silica, diatomite could be one of the best silica precursors for producing silicon based materials with interesting nanoscale morphologies

2.3 Pre-Treatment Techniques

Thermal and mechanically-driven pre-treatments have witnessed growing utilization in the development of silicon-based materials due to their ability to modify the structure and properties of materials for specific applications. In general, thermally-driven treatments such as drying, microwave heating, calcination and roasting have been widely reported as far as diatom-derived silica related studies are concerned [43]. Thermal pre-treatments are frequently used because they can modify several powder characteristics (color, particle size, specific surface area, pore size and volume, crystalline state and crystallite size changes). Contrarily, mechanically-driven pre-treatment can modify few powder characteristics (specific changes in the particle size, surface area and pore size and volume). Nonetheless, treatments by means of applied mechanical forces have been reported in some diatom-derived silica studies.

2.3.1 Mechanical Pre-treatment

Mechanical pre-treatments normally involve high energy ball milling and some recent studies utilized this pre-treatment step in their work [28,47,48]. Typically, ball-milled DE shows significant changes in the particle size, pore size and specific surface area. Other material attributes such as crystallinity, phase composition and color changes are least affected by ball milling. Even though ball milling of diatom-derived silica has not received much attention like counterpart thermal processes, recent reports suggest this as a crucial step for some specific applications. A study by Blanco et al. [28] reported the role ball-milling played on the electrochemical properties of a diatom-derived silica negative electrode. In their work [28], the ball milled diatom-derived silica powder

showed an increase in specific surface area from $1.2m^2g^{-1}$ (pristine DE) to $17.3m^2g^{-1}$ for the milled DE. Additionally, the mean particle size of the ball-milled DE powder was significantly reduced to 470nm from 17mm for the pristine powder. They also reported an increased presence of mesopores in the ball-milled powder compared to the pristine powder. Blanco et al. [28] indicated that although the mesopores could have been present in the pristine powder, they became accessible after ball milling. Interestingly, the powder characteristics of the ball-milled powder improved the electrochemical performance of the negative electrode. The DE-based negative electrode prepared from the milled powder showed a higher capacity of $750mAhg^{-1}$ (milled) than the pristine powder ($550mAhg^{-1}$). This was attributed to the shortening of the Li-ion diffusion path and the increased surface area of the powders achieved through particle size reduction. Ball milling offers a cheap and simple way to modify the powder characteristics of diatom-derived silica for specific applications. When combined with thermal pre-treatments this may lead to materials with interesting properties.

2.3.2 Thermal Pre-treatment

Compared to mechanical pre-treatments, thermal treatments can offer more changes in the powder characteristics. However, this is accompanied with high cost and long treatment time. It must be noted that, low vacuum drying and microwave heating do not effect serious changes in the powder characteristics. High temperature thermal treatments such as calcination and roasting lead to significant changes in the powder characteristics. Diatom-derived silica powders are usually dried in low vacuum between 80–100 ^{o}C prior to roasting and calcination. This is usually done to reduce the moisture content of the powder. Microwave heating is another low temperature thermal pre-treatment which modifies the powder properties to some extent [49,50], notably particle size increment and an unclogged pore structure. As far as diatom-derived silica is concerned, calcination involves a high temperature (500–1200°C) treatment under controlled environment (limited flow of oxygen). On the contrary, roasting is performed on powders in the presence of oxygen within the same temperature range as calcination

Calcination and roasting are known to cause a wide range of changes in the powder characteristics including color changes, phase composition crystallite size and particle size [27,29]. In several diatomite related reports, either pristine (dried powder) or calcined/roasted powder (dried and calcined/roasted) were successfully reduced to silicon-based materials [17,51-55]. The different powder properties of pristine and heat-treated diatomite present sufficient basis for selecting the best silica precursor for silicon production, yet no consensus currently exist as recently raised by Korsunsky et al[56]. Pristine diatom-derived silica is amorphous while the heat-treated counterpart is crystalline (mostly cristobalite). Understanding their individual reaction kinetics could provide sufficient justification for selecting the most appropriate precursor and controllable synthesis parameters. Thanks to some comparative studies some guidelines could be drawn for selecting the most appropriate silica source for applications in filtration, cement production, thermal energy storage and photocatalyst [31-33,57,58]. As far as these applications are concerned scientific data is available for selecting the best silica unlike areas such battery technology, supercapacitors and thermoelectrics.

2.4 Metallothermic reduction reaction

The possibility of producing silicon-based materials via chemical reduction of silica with low melting point reductants is a major breakthrough for the nanostructuration of silicon-based materials. This displacement reaction gained popularity in the scientific domain after Sandhage et al. reported on the magnesiothermic reduction of diatom frustules to porous silicon [59]. Following the report by Sandhage et al [59], several groups have successfully replicated this approach to create silicon nanostructures, nanoporous films, nanocrystals, and 1D nanostructure [60-64].

$$SiO_2 \ (s) + 2Mg \ (g) \rightarrow Si \ (s) + 2MgO \ (s) \qquad\qquad (1)$$

Majority of reports focused in this area used magnesium as the reductant due to the low melting temperature, low cost, ready availability and low toxicity of the alkaline

earth metal. This approach offers a lower temperature to reduce silica to silicon with nanoscale morphologies via the chemical reaction in equation (1). The reported temperature range for the MRR of diatomite is between 500 and 950°C. A study by Lai et al, revealed that Mg is an effective reducing agent even below its melting point; however, there is a huge structural damage and change in morphology accompanied with this reductant [65]. Aluminium (Al) however, was an effective reducing agent at its melting point or above, but it offered a better structural and morphological control than Mg. It was also reported that calcium (Ca) was an ineffective reducing agent for Silica. Due to this, Lai et al. suggested an ideal reducing mixture of 70% Mg and 30% Al to offer the least amount of morphological damage. The silica reduction reaction for the ideal reducing mixture reportedly proceeded at a temperature much lower than when using Mg or Al individually. A number of other parameters which affect the size and structure of silicon-based materials obtained from the MRR of silica have also been outlined in a comprehensive review by Entwistle et al. [36]. The following conditions have been identified as critical for the outcome of the metallothermic reduction of silica to silicon-based materials.

2.4.1 Reaction time

The duration of the MRR process varies among existing literature. The reaction times reported are from 30 minutes up to 12 hours [66-68]. It has been reported that the relationship between the reaction time and the silicon yield reaches a plateau for times above 2 hours that corresponds to the completion of the reaction. Lui et al. also reported on the reaction time and temperature of metallothermic reduction of nonporous silica [69]. They observed the formation of silicon at shorter reaction times with very high reaction temperatures. It is reported that at the reaction temperature of 600°C, crystalline silicon was formed but in the case of a lower temperature, 400°C, no silicon was obtained despite allowing the reaction to proceed overnight. The onset temperature of MRR depends on the source of silica, and this is reported to be between 400 to 500°C [70,71]. Wuo et al. reported on the effect of reaction times 2 and 5 hours on the morphology of

the recovered silicon [72]. Both reaction times reportedly had minor effect on the morphology of the recovered silicon [72].

2.4.2 Reaction Temperature

The MRR is a highly exothermic reaction and this means the actual reaction temperature could become higher than the designated temperature. With very high temperatures, around the melting point of both silica and silicon (1700 and 1414°C), significant modification of on the morphology can be expected. Excessive heat could destroy the natural architecture of the silica precursor, while also causing agglomeration of the silicon domains into larger crystals. Barreti et al recently reported that between 750 and 950°C, temperature has little effect on the silicon yield [63,70]. However, they reported that high temperatures yield more Si when the Mg stoichiometric ratio is increased above 2:1. Also at 750°C, a significant amount of Mg_2Si is formed than at 950°C. This has been attributed to the solid state reaction between SiO_2 and Mg_2Si favored by the accelerated kinetics due to the high temperatures. Since this solid state reaction is diffusion controlled, longer reaction times and higher temperatures favor the reaction presented in equation (2), thereby increasing Si yield.

$$SiO_2 \text{ (s)} + Mg_2Si \text{ (s)} \rightarrow 2Si \text{ (s)} + 2MgO \text{ (s)} \qquad (2)$$
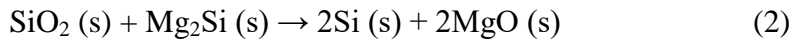
Xie et al. reported that temperatures between 700 to 900°C can reduce the formation of Mg_2SiO_4 compound [67]. High temperatures also increase the Mg vapor pressure at the SiO_2/Mg interface which favors the formation of MgO over Mg_2SiO_4. Furthermore, reaction temperatures between 500 and 800°C reportedly lead to a decrease in surface area and pore volume [65].

2.4.3 Heating Rate

Another crucial reaction condition is the ramping or heating rate. It has a strong effect on silicon morphology. With faster heating rates, large amounts of heat do not have enough time to dissipate through the sample, thus resulting in high local temperatures. This could lead to the occurrence of nearby reactions. It can as well cause the fusion of recovered silicon and the loss of small pores [36]. Also, MgO can be coated with the recovered silicon, and this could lead to MgO contamination even after etching. Porosities between 200 and 300nm have been reported for such silicon products with macroporous structure [36]. This makes slower heating rates a preferable option. Lui et al. reported on the effect of heating rate on the morphology of silicon [71]. The effect of 40^oC min^{-1} and 5^oC min^{-1} up to 650^oC for the MRR of rice husk derived silica was investigated. A heating rate of 40^oCmin^{-1} was reported to produce mainly macroporous silicon particles with a specific surface area (SSA) of $54m^2g^{-1}$ and negligible pores below 20nm. The 5^oCmin^{-1} heating rate however, produced partially interconnected mesoporous silicon nanoparticles with SSA of 245 m^2g^{-1}. Porosity of 10nm width was observed in the sample produced with 5^oCmin^{-1} heating rate.

With the help of Thermal Gravimetric Analysis (TGA) and Differential Thermal Analysis (DTA), Lui et al. confirmed the presence of a strongly exothermic reaction between $400-450^oC$. There was no reaction below 400^oC, suggesting that fast heating rates could be applied until this temperature. Shi et al. studied the effects of heating rates 5, 3, and 1^oCmin^{-1} on silicon recovered from rice husk-derived [73]. In their study, the high heating rates (3 and 51^oCmin^{-1}) were observed to fuse silicon particles together and remove micropores. This eventually resulted in a further decrease in pore volume and surface area. Heating rates of 1^oCmin^{-1} were observed to prevent significant changes in the Si morphology. X-ray diffraction analysis also confirmed larger MgO and Si crystallites at faster heating rates combined with increased Mg_2Si content and Mg_2SiO_4 [73]. The formation of Mg_2SiO_4 was attributed the mismatches at the SiO_2 / Mg interface caused by fast heating rates.

2.4.4 Molar Ratios

The Mg:Si ratio is another crucial parameter for the reaction yield and side reactions. It has been reported that an increase in the molar ratio above the stoichiometric level of 2:1 decreases the silicon yield and promotes the formation of Mg_2Si. It was recently reported that maximum silicon yield was achieved by using excess Mg of 5wt.% (2.1 Mg: 1 SiO_2 stoichiometry) [63,70]. Besides the effects on the silicon yield, the Mg:Si molar ratio is known to affect the purity as well. It is known that Mg impoverishment at the Mg/SiO_2 interface is beneficial for obtaining high purity silicon, as by-product Mg_2SiO_4 is not formed. This was also evidenced in a study by Chen et al., where an increasing Mg molar ratio reduced the formation of Mg_2SiO_4 [74].

2.4.5 Powder Mixing

Effective powder mixing is crucial because a homogeneous distribution of Mg and silica ensures minimal diffusion lengths for the reaction and consequently improves the kinetics. A maximum silicon yield of 64% was reportedly obtained after magnesiothermically reducing rice husk-derived silica at 650 ^{o}C, with reactants well mixed and particles dispersed [71,73]. On the contrary, a silicon yield as low as 4.2wt% was observed when powders where reduced without mixing. Interestingly, the reaction with 64% Si yield terminated without any unreacted silica but a significant portion of precursor silica remained unreacted in the low Si yield reaction. It is reported that increased reaction duration for the unmixed powders yielded far less Si than the well mixed powder at less reaction time. This was attributed to a poor distribution of reactants necessitating the need for thorough mixing. Also, increasing the Mg grain size from fine powder (325 mesh), chips (4-30 mesh), and foil shows a decline in the reduction rate as a result of drastic decline in proper mixing of reactants [65].

2.4.6 Heat Scavengers

Undoubtedly, the heat released during the magnesiothermic reduction of silica is detrimental to the both the particle size and structural morphology of silicon. For large batch size, a low heating rate has been reported to be efficient since a huge amount of heat is accumulated in such reactors [71]. Recovered silicon with a mesoporous structure was reportedly produced from biosilica on a 30g reaction scale by Batchelor et al. [75]. This was achieved with the help of NaCl. In this case NaCl served as a heat scavenger, by consuming the excess heat released during the reaction. A similar approach was reported by Luo et al. [76]. It is an already established fact that, the actual temperature of the reaction is higher than the designated temperature. As the temperature increases, NaCl melts at 801°C, consuming the excess heat due to its high enthalpy of formation. Luo et al observed that samples without heat scavenger NaCl had local temperatures above 1300°C. However, NaCl inclusion maintained the local temperature between 800 and 1100°C. Any further increase in the ratio of NaCl did not reduce the temperature due to limitations in the degree of mixing. In a related study, the silica precursor was pre-coated with NaCl and that was beneficial for controlling the morphology of the recovered silicon [77,78]. NaCl inclusion has also been reported to reduce the presence of Mg_2Si in the silicon produced [79].

2.4.7 Crystallite Size

The characteristic properties of the recovered silicon depend on the nature of the precursor silica. It has already been established that, reaction temperature and time have significant effects on the silicon crystallite size. High reaction temperatures and long reaction time facilitate sintering of silicon crystallites as a result of the excess energy involved in the synthesis process [80]. Xing et al., reported that a higher porosity and higher surface area of the precursor silica resulted in small silicon crystallites [38]. This has been attributed to the insufficient mass transport which impedes the coarsening of silicon crystallites. The particle size distribution of precursor silica is another powder

characteristic that has a huge influence on the silicon crystallites formed. Silica with small particles reportedly leads to small silicon crystallites and vice versa.

2.4.8 Other Reduction Routes

The search for optimal ways of synthesizing nanostructured silicon based materials from silica has led to the introduction of other interesting chemical reduction routes identical to the MRR process. Liang et al., reported a new reduction route called "Deep Reduction and Partial Oxidation" [81]. This is a two-step reduction strategy to produce mesoporous silicon as schematically shown in Figure 4. The non-conventional technique involves the deliberate synthesis of Mg_2Si and MgO followed by a partial oxidation in an oxygen-rich atmosphere as indicated in the equations (3) and (4) below.

$$Mg\ (g) + SiO_2 \rightarrow 2\ MgO + Mg_2Si \tag{3}$$
$$Mg_2Si + 2MgO + O2 \rightarrow 4MgO + Si \tag{4}$$

This non-convention MRR process has been reportedly used to synthesize silicon with a yield of 90% from a batch size of 10g. In addition to the very high silicon yield, this route also benefitted from little to no oxidation of the silicon product. It is reported that silicon oxidation was not significant at temperatures below $800^{o}C$, but a thin SiO_2 layer was formed on the surface of Si. Interestingly, the presence of such native oxide layer is desirable for electrochemical performance by improving the quality of the solid electrolyte interface (SEI) layer formed and offering better structural stability compared with silicon [82,83].

Another non-conventional route developed is captured in the studies by Choi and Lia et al. [65,84]. Both studies combined magnesium and aluminium as reductants for the metallothermic reduction of silica. Cho et al. [84] synthesized Si/Al_2O_3 composite by firstly reducing silica via the aluminothermic reduction at 900 ^{o}C and subsequent magnesiothermic reduction of the product from the first reduction reaction. This is known to be beneficial for synthesizing Si/ Al_2O_3 nanocomposites. The presence of Al_2O_3 in

silicon-based anodes is particularly known to be beneficial for the overall electrochemical performance by buffering the huge volume expansion and providing a stable SEI layer. The protocol used by Cho et al. [84] is captured in equations (5) and (6)

$$4Al + 3SiO_2 \rightarrow 2Al_2O_3 + 3Si \qquad (5)$$
$$Al_2O_3 + 3Mg \rightarrow 4MgO + Al \qquad (6)$$
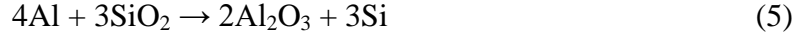
In another related study, Lai et al. [65] utilized both aluminium and magnesium as reductants in a single-step silica reduction process. Based on their findings, an eutectic mixture composed of 70% magnesium and 30% aluminium was proposed as the ideal reductant to initiate the reduction process at a low temperature 450°C. This technique reportedly favors the formation of amorphous silicon with minimal microstructural damage which is beneficial for lithium-ion battery applications.

Figure 4 Schematic representation of the unconventional MRR (Deep reduction and Partial oxidation) [81]

2.5 Textured Silicon Surfaces

Silicon substrates have a range of fascinating properties which makes them attractive as a platform for many active materials. As a semiconductor material, silicon substrates allow for ease of fabricating microelectronic devices with many possibilities. In conventional terms, silicon substrates are widely known for their applications in the semiconductor and photovoltaic industry. However, a combination of high surface reflection and excessive light transmission at longer wavelengths remains a major setback. The fabrication of nanostructured, textured or modified surfaces has been widely

40

studied to improve the performance of materials, especially Si substrates in a several application [85-94]. Textured Si surfaces in particular have been widely studied to overcome the high surface reflectivity of silicon substrates. A high surface reflection in silicon substrates is one of the main factors that accounts for the low efficiencies reported for silicon-based solar cells. To address this setback, recent studies have focused on synthesizing nanostructured silicon surfaces by conventional electrochemical techniques including HF etching, stain etching, metal assisted chemical etching, laser irradiation, and the molten-salt Fray–Farthing–Chen Cambridge (FFC Cambridge) process [95]. The majority of nanostructured silicon surfaces reported have been often referred to as black silicon due to their dark visual appearance. Black silicon (BSi) is a nanostructured silicon wafer surface, best described as an array of uniform peaks and valleys. BSi is widely known for the significant suppression of unwanted surface reflections and simultaneous enhancement of scattering and absorption of light on device surfaces [95].

Although, significant progress has been made with the discovery of BSi, several drawbacks have been reported [95]. For example, it is presently difficult to apply the electrochemical etching technique to larger wafer surfaces area, thus restricting it applications to areas where miniature samples are used. In the case of metal-assisted chemical etching, metal contamination is a major problem which often requires additional purification processes. Apart from metal contamination of the nanostructured surface, some techniques can cause significant damage to the substrate silicon wafer. The recently developed FFC Cambridge process requires a relatively high temperature and renders the silicon substrate prone to Mo and other metals contamination. Also, one common setback of these conventional techniques is the high cost, complexity and environmental unfriendliness. The conventional techniques typically require the removal of material from the surface of the substrate [95].

Apart from the superior optical properties offered by textured Si surfaces, there is growing interest in their use as a platform for active materials such as ZnO, carbon-based materials, TiO_2 for sensing applications [91,92]. Textured Si surfaces generally have high surface areas which is required for such applications. Not long ago, Sternard et al [85]

41

demonstrated the influence silicon microstructures exert on the electrochemical performance of single crystalline silicon (c-Si). Using an electrochemical etching technique, the surface of a c-Si was modified and subsequently used as a negative electrode in a Li-ion battery. The textured Si surface reported by Sternard et al [85] showed excellent electrochemical performance coupled with an impressive structural stability. The recent successes with textured silicon surfaces shows the critical role they play in functional applications and the quest for low cost, eco-friendly and facile synthesis routes to create them remains a top priority.

2.6 Phase Separation

Phase separation is a common process in materials development and crucial for understanding microstructural evolution, especially in metallurgy. The development of alloys is as a result of phases reacting differently under given conditions. For instance, pearlite formation in steel is due to the separation of lamella consisting of a carbon-rich iron (*cementite*) phase and a carbon-deficient iron (*Ferrite*) phase from a homogenous austenite phase upon furnace cooling. As the name implies, phase separation is the process of de-mixing between two materials upon transition from a homogeneous mixture, most often upon aggregate state change from liquid to solid. The immiscibility point presents a wide range of possibilities for synthesizing materials with desired microstructures. Lately, this phenomenon has been used in the development of porous materials for membrane applications [96-99]. Most importantly, the phase separation technique could be used to create of uniformly dispersed micro- to nano-particulate composites, homogenously dispersed silica micro-to nanospheres and hierarchically porous polymer and carbon materials as schematically shown in Figure 5.

Recently Lee et al.[100], synthesized silica nanospheres, porous polymer and carbon membranes via the phase separation technique between Polyacrylonitrile (PAN) and Tetraethyorthosilicate (TEOS) in their respective solvents. It was shown that, depending on the mixing ratio between the polymer and silica precursors, the size and diameter of the spheres and membranes could be controlled. This technique promises a

facile and cheap way to synthesize functional carbon-based materials and Si/C nanocomposites with interesting nanoscale features.
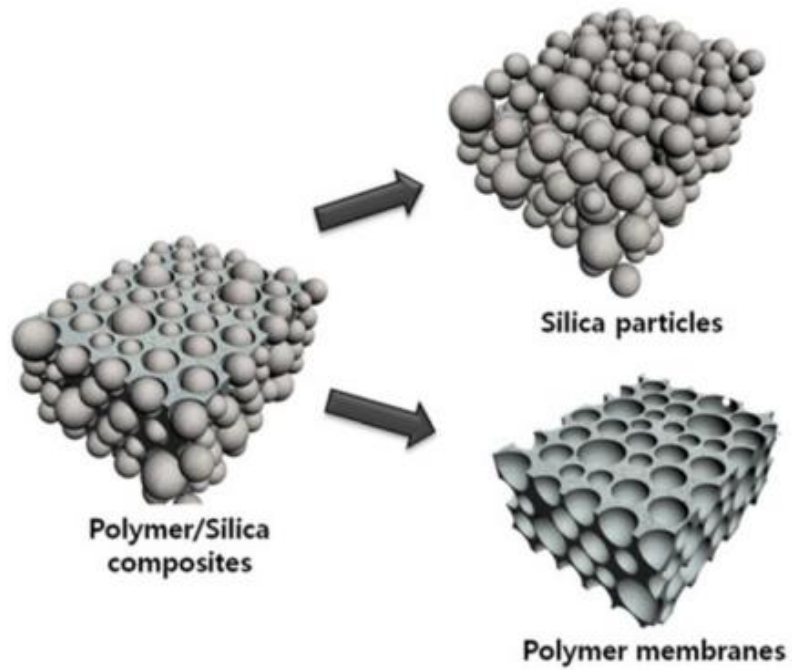
Figure 5 Schematic illustration of silica spheres and polymer membranes that can be obtained from the phase separation technique

Chapter 3. Materials and Methodology

In this chapter, the materials and synthesis protocols used to obtain different silica precursors and their corresponding silicon-based materials are outlined and accompanied with state of the art characterization techniques for structure and properties studies. The synthesis processes showed high repeatability following several repetitions. To induce near-complete crystallization in amorphous silica, the powders were roasted and calcined separately at 1100^oC for 4 hours. The different heat treatment procedures showed remarkable visual differences accompanied with significant changes in the particle and crystallite sizes. In terms of their porosity, the pores in the roasted and calcined silica appeared unclogged. This is particularly important for the absorption capacity of diatom-derived silica. The powders were subsequently reduced in a Mg environment at $600\ ^oC$ for 6 hours to obtain silicon with nanoscale morphologies. To obtain ultra-high purity silicon, the as-reduced powders were purified via HCl and HF washing.

The metallothermic reduction of silica was further explored to create a textured Si surface which followed the same purification process to obtain ultra-high purity silicon coating. The initial results confirmed the possibility of creating silicon coating via in-situ magnesiothermic reduction of silica on silicon substrates but posed further research question which were addressed through reaction kinetics studies. This led to an in-depth understanding of the unconventional surface texturing process and a consequent optimization of the process. The practicable textured Si surfaces were subsequently investigated for their optical properties. The chapter also details the use of the phase separation technique as facile approach to functionalize the surface of textured silicon by creating micro to nano-porous amorphous carbon coatings on top.

3.1 Diatom-derived silica

In this study, diatom-derived silica was used as the main silica precursor due to its neatly formed nanoporous structure. The high porosity of diatomite makes it a suitable candidate for applications including filtration, absorption and a supporting material or

template for active materials for specific applications [43]. Food grade diatomite obtained from QUANTUM Ltd., Nikolsk, Penza region, Russia was used in this study. Microstructural studies confirmed the nanoporous nature of the powder. The chemical composition of the powder used is presented in Table 1. The powder was dried in a vacuum oven at 100 ^{o}C to remove water as diatom-derived silica is a hydrous siliceous material.

Table 1 Chemical composition of Diatomite powder

Component	SiO_2	Al_2O_3	Fe_2O_3	MgO	K_2O	Na_2O
Quantity (wt. %)	86%	5.5%	2.5%	0.78%	1.39%	0.22%

3.2 Heat Treatments

Heat treatments of diatom-derived silica have been widely studied to understand the effects they have on the phase composition and microstructure. Roasting and calcination are common heat treatments undertaken to modify the morphology of diatomite for conventional application as filtration aids and supporting material in thermal energy storage. Fundamentally, roasting is performed in open air at high temperatures below the melting point of the material but calcination typically involves heating under controlled environment (absence or limited amount of air). As a result of the different heating environments, roasting and calcination promote different physical transformation. For instance, roasting normally involves dehydrating an ore but moisture is driven out during calcination. Additionally, roasting leads to the release of toxic, metallic and acidic compounds whereas only CO_2 is given out during calcination. In this work, pristine diatom-derived silica powder were calcined and roasted at 1100 ^{o}C for 4 hours before the thermite reduction process. The heating temperature chosen is consistent with cristobalite transformation from amorphous silica. The entire heating procedure lasted 4 hours in order to limit the extent of morphology damage as heating diatom-derived silica at elevated temperatures has the tendency to destroy the neatly formed porous network. The pristine, roasted and calcined powder were subsequently

45

characterized using particle size analyzer, BET porosimeter, SEM, and XRD, TGA/DSC, and Raman Spectroscopy.

3.3 Powder Characterization

The pristine and heat treated silica precursors together with their corresponding recovered Si powders were characterized with the state of the art techniques below. These characterization techniques provided sufficient insight into the microstructure, phase composition, thermal properties and powder characteristics of the powders.

3.3.1 Particle Size and Pore Size Studies

To understand the effects of thermally-induced transformation on the silica powder characteristics, the particle size distribution, powder surface area and pore size measurements were performed on the Fritsch Particle Analyzer and the Quantachrome Nova 2200e (Anton Paar, Graz, Austria) machines respectively. The pore size and specific surface area measurements were preceded by a degassing process performed at 200 °C for 1000 min

3.3.2 Microstructural Studies

Microstructural analysis of the powders and porous consolidates were performed on the Helios dual beam system (Thermo Fisher Scientific, Waltham, MA, USA) that combines a scanning electron microscope with a Focused Ion Beam. The topography of the textured silicon surfaces was observed, and Focused Ion Beam (FIB) cross-sectional milling was performed at the sample tilt angle of 52° after applying a protective platinum coating. Energy Dispersive X-ray spectroscopy (EDS) analysis was carried out to determine the elemental composition of the samples.

3.3.3 X-ray Diffraction Analysis

The phase composition of the powders and textured surfaces were investigated using the Bruker D8 Advance Diffractometer (Bruker, MA, USA) with Cu Kα1 (λ=1.54 Å). The phase composition of the samples was investigated using the MATCH phase identification software.

3.3.4 Raman Spectroscopy Studies

The Raman spectra of the samples were collected at room temperature using DXR2xi Raman Imaging Microscope (Thermo Fisher Scientific, MA, USA) with an excitation source of 532 nm line of an Ar-ion laser.

3.3.5 TGA and DSC

The thermal behavior of the silica precursor and the reaction kinetics of their respective magnesiothermic reduction of silica were studied using the TG-DTA-MS STA-449 apparatus (NETZSCH Scientific Instruments Limited, Selb, Germany). Here, the differential thermal analysis (DTA) was performed on diatomite separately in dry air and argon flow (50ml/min) from room temperature to 1500 ^{o}C with a heating rate of 10 K/min^{-1}. The thermal profiles of the magnesiothermic reduction of pristine and heat treated silica were performed under the flow of argon at 5 K/min^{-1} and 10 K/min^{-1}.

3.4 Magnesiothermic Reduction Reaction

Metallothermic reduction reactions have gained a lot of attention as far as the synthesis of nanostructured silicon-based materials from silica is concerned. This technique offers a low temperature synthesis route which is critical for controlling the morphology of the reaction product. To initiate the metallothermic reduction reaction, a reductant with low melting temperature is placed in the same inert environment (preferably argon) with a silica precursor and heated to temperatures slightly above or

below the melting point of the former. To the best of our knowledge, only two types of the metallothermic reductions reactions have been reported to date. These are the magnesiothermic and aluminothermic reduction reactions, where both names are indicative of the reductant used. Lai et al explored the calciothermic reduction of silica owing to its favorable thermodynamic parameter (ΔG= -168.5 kJmol-1), similar to both magnesiothermic (ΔG= -135.9 kJmol-1) and aluminothermic (ΔG= -157.8 kJmol-1) reduction of silica [65]. Despite its thermodynamic feasibility, the reaction terminated without the formation of silicon. The authors attributed this to a relatively high diffusion barrier due to the large size of the calcium atoms that prevents the reaction from occurring. Further work in this direction is needed to exploit the possibilities with the thermodynamically feasible calciothermic reduction reaction of silica. Based on the underlying knowledge of metallothermic reduction reactions, the following protocols were developed to synthesize silicon powders with nanoscale morphologies and porous consolidated Si coatings.

3.4.1 Silicon Powder from Diatom-derived silica

The conventional MRR process of mixing precursor silica powder with the reductant was followed in this work. The reduction protocol applied is given below as following:

- Reaction mixture of silica and magnesium in a mass ratio of 2:1 was prepared by mixing the individual powders together in a ceramic mortar.
- The well-mixed powder was loaded into a corundum crucible and heated at 600 $^{\circ}$C for 6 hours.

The as-reduced powders were purified via a purification process as follows:

- As-reduced powders were rinsed in 1M Hydrochloric (HCl) acid severally using a centrifuge followed by distilled (DI) water washing.
- The resulting powder was cleansed with 5% Hydrofluoric (HF) acid using a centrifuge and followed by DI water washing.

- The final powder obtained was dried in a petri dish in a vacuum oven at 70 $^{\circ}$C overnight.

The purification steps are standard procedure for obtaining ultra-high purity silicon powders and depend on time. A significant amount of time is needed to completely rinse all by-products formed during the reduction reaction. To make the purification process effective, it is essential to crush and mill the as-reduced powders which often appear compact. This creates enough surface area accessible by the dissolving solvent. The main by-products rinsed in this stage are magnesium oxide (MgO), magnesium silicide (Mg_2Si) and unreacted silica.

3.4.2 In situ formed Silicon nanoflakes

An efficient solution to the poor optical properties of silicon substrates is through surface modification. Indeed, this approach has been explored by many researchers and has led to the discovery of black silicon (BSi) [101-106]. Black silicon is typically produced via several electrochemical routes and has been reported to significantly reduce unwanted surface reflection on silicon substrates. The progress made with BSi however comes with several challenges such as cost, scalability and environmental concerns. As these setbacks continue to persist, it is increasingly important to look for cheaper, scalable and eco-friendly approaches to modify silicon substrates. This study sought to create nanostructured silicon coatings on silicon substrates via the magnesiothermic reduction of silica as schematically shown in Figure 6. The preliminary steps taken to achieve this are as follows:

- The three silica (pristine, roasted and calcined) and magnesium powders were mixed separately in a mass ratio of 2:1.
- Slurry of the reaction mixture (SiO_2 and Mg) was prepared in a petri dish using ethanol. To achieve homogeneity, the slurry was mixed several times.
- The slurry was quickly transferred to the surface of an n-type silicon wafer with (001) orientation (Terra Group OOO, Moscow) via pipetting and allowed to dry.

49

Prior to this, the silicon wafer surface was cleansed with 5% HF to remove any oxide layer and rinsed severally with DI water.

- The silicon wafer with the dried reaction mixture was reduced under the flow of argon in an electric furnace at 700 °C for 2.5 hours.

- After the thermite reaction, the loose residual powder on the silicon substrate was gently brushed off. The as-synthesized coating was purified using the same purification step as with the silicon powders and dried in vacuum at 70 °C overnight.
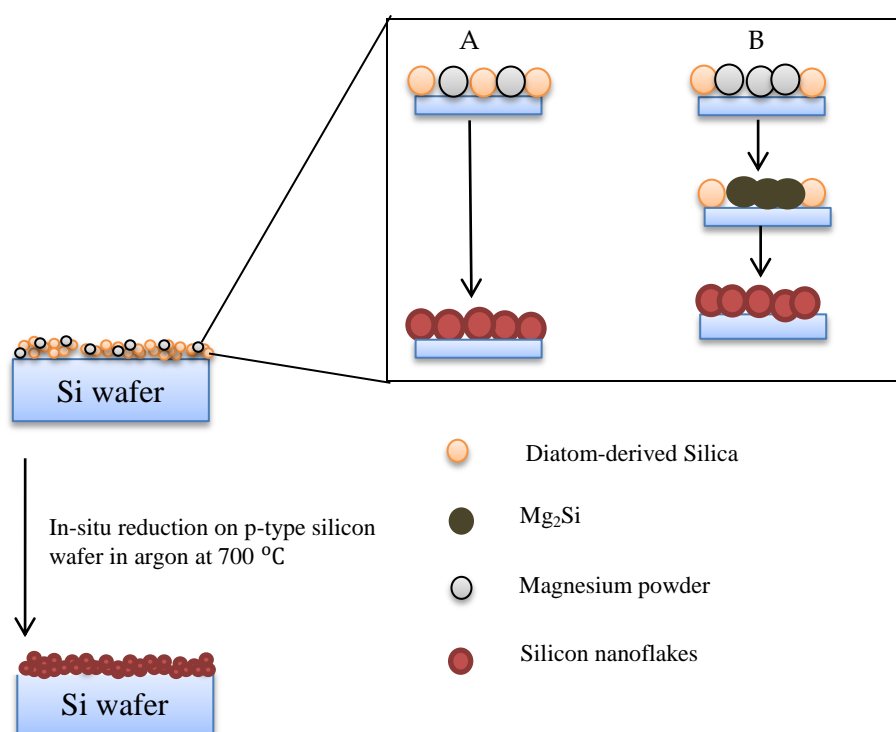
Figure 6 Schematic representation of strategy used to produce silicon nanoflakes. Zoom in: illustrating possible surface reactions that lead up to silicon coating formation

The surface of the silicon substrate was coated with coffee-brown nanoporous silicon clusters after the reduction and purification processes. Early results showed a proof of concept but required further work to tackle a major drawback with the

uniformity of the modified surface. To address this, the effects of some critical reaction parameters on the uniformity of the *in situ* formed Si coating were studied. The reaction temperature and reactant mixing ratio were investigated at constant reaction duration (6 hours).

3.5 Phase Separation

As far as the synthesis of materials with micro- to nano- structures is concerned, it is critical to have greater control over the process. Even though majority of synthesis processes are feasible, the outcome may not be easily predicted due to the insufficient control over the process. Phase separation is an ideal technique for the synthesis of materials with uniform and hierarchical porosities, as well as powders with homogenous particle size distribution. The technique offers greater control over size and composition of the target material. Although this technique is a fundamental to the development of alloys and compounds, the recent focus has been aimed at creating materials with desired architectures. In this study, the immense possibilities with the phase separation technique were explored for the creation of hierarchically structure materials for tailored applications. The pathways taken are given as follows.

3.5.1 Porous Carbon Anti-Reflective Coating

Conventionally, the phase separation technique offers a route to produce porous polymer membranes, silica micro- to nano- spheres and a nanocomposite based on both material classes. Using this principle, porous amorphous carbon anti-reflective coatings on a textured Si surface were formed via the phase separation between polyacrylonitrile (PAN) and tetraethyl orthosilicate (TEOS) in their respective solvents. The technique presents a facile approach to functionalize textured Si surfaces and consequently compensate for optical losses encountered in the longer wavelength range of the EM spectrum. To understand the effects of the morphology on the optical properties, different amorphous carbon microstructures were analyzed as provided in the formulations in

Table 2. Fibers of polyacrylonitrile (PAN) purchased from Tekhsnabeksport, Inc., (Saratov, Russia) were used as the carbon precursor. The PAN fibers were dissolved in dimethylformamide (DMF) obtained from Komponent-Reaktiv Ltd (Moscow, Russia). As the silica precursor, tetraethyl orthosilicate (TEOS) solution was prepared by dissolving in HCl and tetrahydrofuran (THF). Both TEOS and THF were purchased from Komponent-Reaktiv Ltd (Moscow, Russia). The synthesis protocol is schematically shown in Figure 7 and was carried out as following:

- The polymer solution was prepared by dissolving 3 wt. % PAN in DMF.
- An aqueous TEOS solution was prepared by mixing the precursor with 0.024 M hydrochloric acid (HCl) in a ratio 6:2.3.
- The aqueous TEOS/HCl solution was mixed with THF in a 1:3 ratio and stirred for 2 hours.
- The TEOS/HCl/THF and PAN/DMF solutions were mixed in a desired ratio (1:1, 1:2, and 1:3).
- The resulting solution was pipetted on the nanostructured Si surface and dried in a vacuum oven at 60°C.

After the drying process, the solid material (PAN/Silica) obtained was further treated to obtain a porous carbon membrane as provided below.

- The PAN/Silica nanocomposite on the textured Si surface was etched in 5% HF to remove the dispersed silica spheres and rinsed severally in DI water.
- The resulting porous PAN film on the textured Si surface was dried in a vacuum oven at 70°C overnight.
- The dried porous PAN on the textured Si surface was carbonized at 850°C under the flow of argon in an electric furnace for 3 hours.

Table 2 Notation of different Si/a-C nanocomposite surfaces with their respective R value for a-C.

Samples	Crystalline Si (C-Si)		Silicon nanoflakes from DE (Si@DE)		Silicon nanoflakes from DE (Si@SB)	
	Name	R-value	Name	R-value	Name	R-value
PAN	C-Si/a-C	1.03	Si@DE/a-C	1.03	Si@SB/a-C	1.06
1 PAN solution: 1 TEOS solution (1:1)	C-Si/a-C (1:1)	1.03	Si@DE/a-C (1:1)	1.02	Si@SB/a-C (1:1)	1.03
3 PAN solution: 1 TEOS solution (3:1)	C-Si/a-C (3:1)	1.03	Si@DE/a-C (3:1)	1.01	Si@SB/a-C (3:1)	1.02

NB: All samples followed the same carbonization process (850°C for 5 hours)
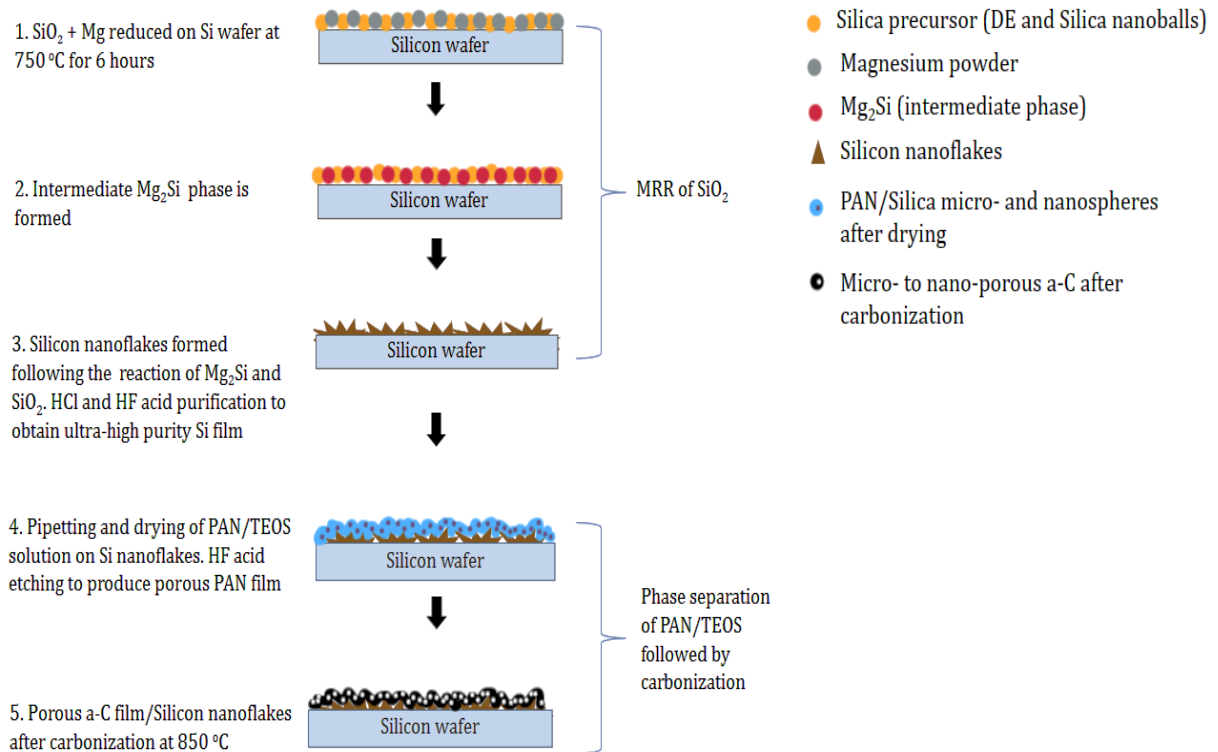
Figure 7 Flow chart of synthesis process (bi-layer nanocomposite Si/a-C)

3.6 Optical Properties of Textured Si and Nanocomposite Si/C Bi-layers

The preliminary reflection spectrum was obtained using the Optical Spectrum Analyzer BOSA 440 (Aragon Photonics, Zaragoza, Spain) in the infrared (IR) region. The initial results obtained was only limited to the infrared range due the coverage range of the device. The subsequent absorption measurements were performed using the PVE300 Photovoltaic Device Characterization System (Bentham, Reading, UK), namely the DTR6 integrating sphere, and the TMc300 monochromator. This device provided a broader span of the optical property measurement.

3.7 Atomic Force Microscopy Studies

The conductivity type of the textured silicon surfaces were studied via Atomic Force Microscopy (AFM). Kelvin Probe Force Microscopy (KPFM) measurements were performed in a 2-pass amplitude modulation mode with the 30 nm second pass height on Cypher ES Atomic Force Microscope (Oxford Instruments, Abingdon, UK) under dry Ar atmosphere ($O_2 < 0.1$ ppm, $H_2O < 0.1$ ppm) in dark and under illumination with a blue laser ($\lambda = 405$ nm). Si AFM probe with conductive W_2C coating, 245 kHz first resonance frequency, and 9.4 N/m spring constant was used. The contact potential difference (VCPD) measured between the silicon nanoflakes/silicon wafer and the AFM probe was used to estimate samples' work function.

3.8 Electrode Preparation and Electrochemical Measurement

The battery anodes prepared in this work followed the standard electrode preparation provided as follows:

- Slurries containing 50 wt% active material (SiO_2 or Si), 35 wt% carbon black and 15 wt% polyvinylidene fluoride (PVDF) were properly mixed in a mortar and tape casted onto 18 μm thick Cu foils. The electrodes were dried under vacuum overnight at 110 °C and then transferred to an Ar-filled glove box.

- Coin cells were assembled using lithium foil (0.75 mm thick) as the counter electrode and 1 M LiPF$_6$ in 50 : 50 vol% EC : DEC electrolyte (Sigma Aldrich).

The electrochemical performance of the electrodes was evaluated by performing galvanostatic charge–discharge tests between 0.002 V and 2 V *versus* Li$^+$/Li, at 50 mA g^{-1} and 100 mA g^{-1} using the Biologic potentiostat/galvanostat. All measurements were carried out at room temperature.

Chapter 4. Results and Discussion

Thermally induced phase transformation in the Si-O system showed remarkable effects on the silica powder characteristics and recovered silicon. More importantly, the different heat treatment environments showed distinct effects on the powder characteristics despite showing the same crystalline phase (cristobalite). The crystallite size varied significantly for the roasted (11.44 nm) and the calcined powder (8.58 nm) and this could lead to different electrochemical performance. When tested as anode materials, the calcined diatom-derived silica powder showed the best discharge capacity of 340mAhg^{-1} amongst the three silica types (255mAhg^{-1} for roasted and 168mAhg^{-1} for the pristine powders). These notable changes in powder characteristics also influenced the onset and peak temperatures of the magnesiothermic reduction of silica. The crystalline silica powders offered lower onset and exothermic peak temperatures compared to the amorphous counterpart. Interestingly, the silicon crystallite sizes showed a similar decreasing trend from amorphous to crystalline state like their silica precursor (27.46nm for si@pristine, 16.14nm for si@calcined and 22.93nm for si@roasted).

Apart from particle and crystallite size differences, the individual heating environments showed contrasting color changes, with reasons confirmed through EDS and Raman spectroscopy studies. The recovery of high purity silicon powder and textured surfaces from the metallothermic reduction of diatom-derived silica was confirmed XRD, EDS and Raman spectroscopy studies. The textured silicon presented in the subsequent sections had a structure comparable to BSi and subsequent investigation of its optical properties showed superior absorption and low surface reflection. After further functionalization via the phase separation technique, bi-layer textured Si and amorphous carbon coating showed the best optical response compared to both textured and c-Si surfaces. Along with the superior optical properties, the nanocomposite coatings showed a strong correlation between upper-layer coating morphology and the optical properties, suggesting a potential to tune the optical properties to a desired need.

4.1 Silica Powder Characteristics as a function of Calcination and Roasting

Thermal pre-treatments of silica powder have been widely studied in recent literature because they induce phase transformations coupled with changes in physical/chemical properties of the powder [17,27,29,32,34]. These physical changes include color, pore size and particle size. Heat treatment of diatom-derived silica is particularly a necessary processing step as far as application as filter aid in the food and pharmaceutical industries are concerned. Heat treatment of silica precursors comes in several forms, with calcination and roasting among the most widely known techniques. It is worth mentioning that prior to such treatments, drying of powders is mostly performed. Unlike roasting and calcination where high temperatures are used, drying normally takes place at low temperatures and does not lead to significant changes in the powder characteristics. Drying is normally performed to remove water from the powder. Diatom-derived silica used in this study underwent calcination and roasting treatments and the corresponding changes in powder characteristics were analyzed. Aside from inducing physical changes, these heat treatment procedures have also been widely reported to be an effective purification step. Pristine diatom-derived silica is largely composed of free silica but contains significant amount of impurities commonly trapped within the pores which limit their applicability. The purification of diatom-derived silica via high temperature treatment was recently demonstrated in a study by Qian et al [35].

4.1.1 Modifications in Color, Chemical Composition, Particle and Crystallite Sizes

The diatom-derived silica precursor used in this study exhibited clear color changes after the high temperature treatments. These color changes showed direct dependence on the treatment environment and corroborated previous findings in existing literature [31,32,57,107]. The distinct colors for the calcined and roasted diatom-derived silica powders were accompanied with significant modification in the particle size distribution, pore size and surface area. After calcination, the brown colored pristine powder turned greyish. Oppositely, the roasted powder had a copper red appearance and compact as shown in Figure 8b. Such color changes in diatom-derived silica have been

reported and are known to be largely influenced by the presence of specific Fe ions in the pristine powder which undergo valence changes during heat treatments [108,109].

The chemical composition of the calcined and roasted powders provides further proof of the valence changes responsible for coloration. Although both calcined and roasted powders showed the presence of cristobalite, they exhibited different color changes after the heat treatment. The reason for the drastic change in color from brown to copper-red for roasted powder could be attributed to the oxidation of Fe_2O_3 to Fe_3O_4. From the EDS spectra in Figures 9 and 10, the quantity of Fe in the calcined powder was smaller than for the roasted powder. This can be attributed to the higher relative abundance of Fe cations in Fe_3O_4 than in Fe_2O_3 since most quantitative measurements just focus on the relative abundance of the cations in the sample.
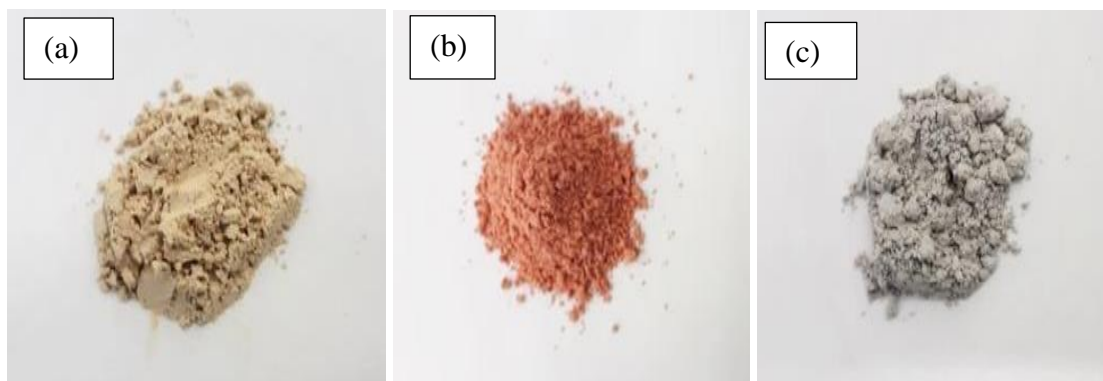
Figure 8 Diatomite Powders 1 (a) Pristine DE, (b) Roasted DE, and (c) Calcined DE

Color changes may not present any beneficial or negative impacts as far as the development of silicon based materials are concerned but it remains undesirable for diatom-derived silica applications as filter-aids [27,31,107,110]. The use of fluxes has been widely reported to prevent or limit coloration during calcination of diatom-derived silica for filtration purposes [27,31,107,110]. Fluxes such as Na_2CO_3, NaCl, NaOH, KCl and KOH have been reported to hinder coloration during high temperature treatments by displacing Fe ions and oxides within the Si-O mesh structure. As a result, the Fe ions get confined in a silicate upon cooling. This weakens the effects of the Fe ions and oxides on

the color of the heat treated powder. Indeed, the phenomenon of color changes during heat treatment is a physico-chemical process and the addition of the right chemical component could inhibit this process. The results from the present study suggest that coloration during heat treatment is a function of previously reported conditions of time and temperature as well as chemical supplements (fluxes) and the heat treatment environment. It is obvious from the present results that, the limited flow of oxygen during the heat treatment process significantly limits the effects of Fe ions and oxides and could optimally prevent coloration of diatom-derived silica as filter-aids when combined with fluxes.
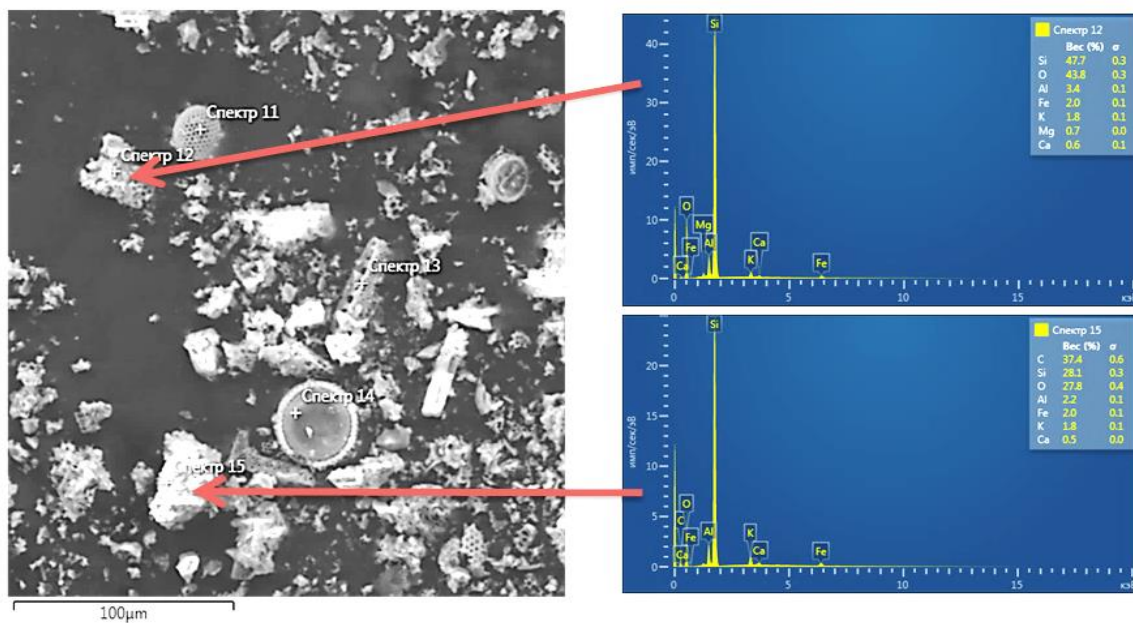
Figure 9 EDS analysis of roasted diatomite powder.

Coloration of diatom-derived silica during heat treatments is accompanied with structural changes which have rather more important effects on other applications. Unlike color changes, modifications in the powder characteristics and morphology are critical not only for conventional applications but for the development of silicon-based materials for several applications. Particularly, high temperature treatments have been widely reported as an efficient way to eliminate unwanted material from the porous network of

59

diatom-derived silica [35]. Blocked pores reduce the efficiency of diatom-derived silica for filtration purposes, and also limit the loading capacity for active materials such as phase change materials for thermal energy storage applications.
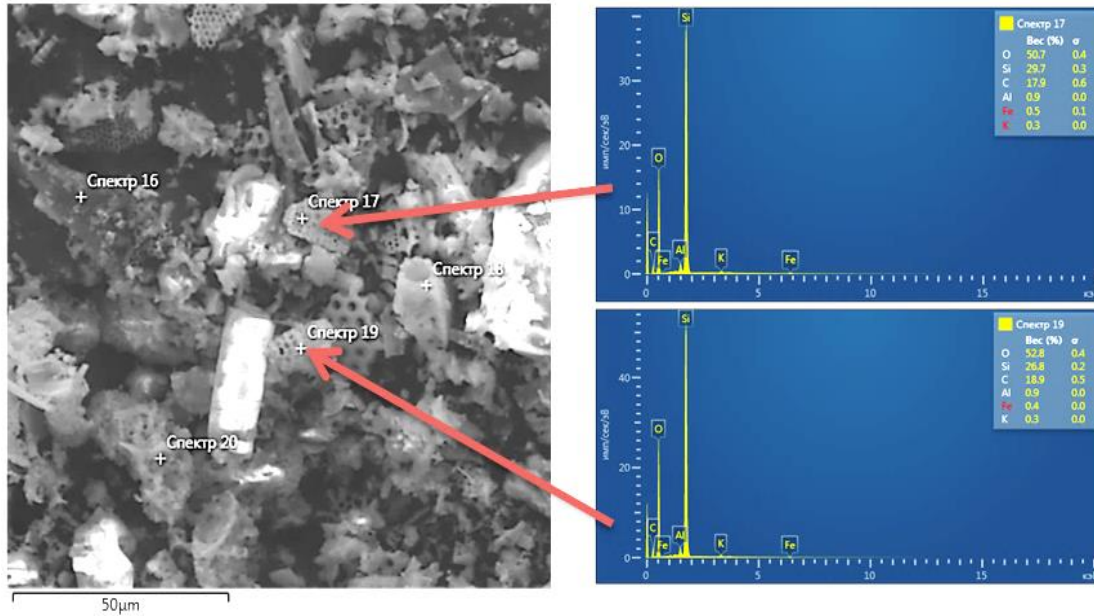
Figure 10 EDS analysis of calcined diatomite powder.

Lately, such heat treatment procedures have been implemented in the preparation of nanocomposite phase change materials, and bio-templated materials for applications in TES, supercapacitors and photocatalysis [32,33,34,111]. Most organic substances found within the pores of diatom-derived silica are mostly volatilized during heat treatments which increase the specific surface area [35]. Even though this remains an important approach for purifying diatom-derived silica powders, the possibility of damaging the frustules remains a major issue. In view of this, an optimal heat treatment temperature of not more than 1000 $^{\circ}$C has been recommended for the removal of impurities. Another setback of heat treatments is the inability to fully eliminate impurities such as oxides trapped within the pores. To optimize diatom-derived silica purification, it is recommended to combine acid washing with heat treatments. Qian et al [35] visualized plenty of the pores in their calcined diatom-derived silica powder after sulfuric acid

washing. In essence, acid washing is more effective for the removal of impurity oxide which blocks pores just like organic matter. Unlike organic matter, which easily decomposes during heat treatments, oxides are hardly removed. Benefitting from the reaction of metal oxides with acids, impurity oxides can be easily removed via acid washing severally. This observation led Qian et al [35] to a conclusion that impurity oxides constitute majority of the materials occupying the pores in diatom-derived silica.

It is an already established fact that majority of phase transformations in the Si-O system are thermally induced and extreme thermal treatments can potentially cause significant structural changes, especially in diatom-derived silica. For the purpose of achieving near complete transformations in this system, temperatures higher than the recommended where used in the present studies. Indeed, as previously mentioned these high temperatures lead to a partial or total collapse of the frustules and the results obtained confirmed this. In spite of this, there appears to be fascinating advantages of such complete transformations.

The partial or complete collapse of diatom frustules during extremely high temperature treatment has been found to lead to remarkable changes in the powder particle and crystallite sizes. The powder particle size distributions of the pristine and heat treated diatom-derived silica powders are shown in Figure 11 below. The d_{90} estimated from the particle size distribution curves for the pristine, calcined and roasted powders showed significant differences. The calcined powder also had a d_{90} relatively smaller than the pristine powder as seen from Figure 11(d). The roasted powder had d_{90} significantly higher than 10 µm. In a report by Ediz et al, a similar phenomenon was observed [31]. The average particle size d_{50} decreased in the calcined powder and slightly increased in the roasted counterpart. Such changes in powder characteristics are desirable for energy applications specifically battery anodes, where small particle and crystallite sizes are recommended to improve efficiency. The changes in powder particle size distribution were accompanied with variations in the surface area and pore size. As can be seen from Table 3, the surface area of the diatom-derived silica powder decreased after the roasting and calcination treatment. The roasted powder showed the smallest

surface area among the three precursors. The pristine and roasted powders showed similar pore radii, while an increase in pore radius was seen in the calcined powder.
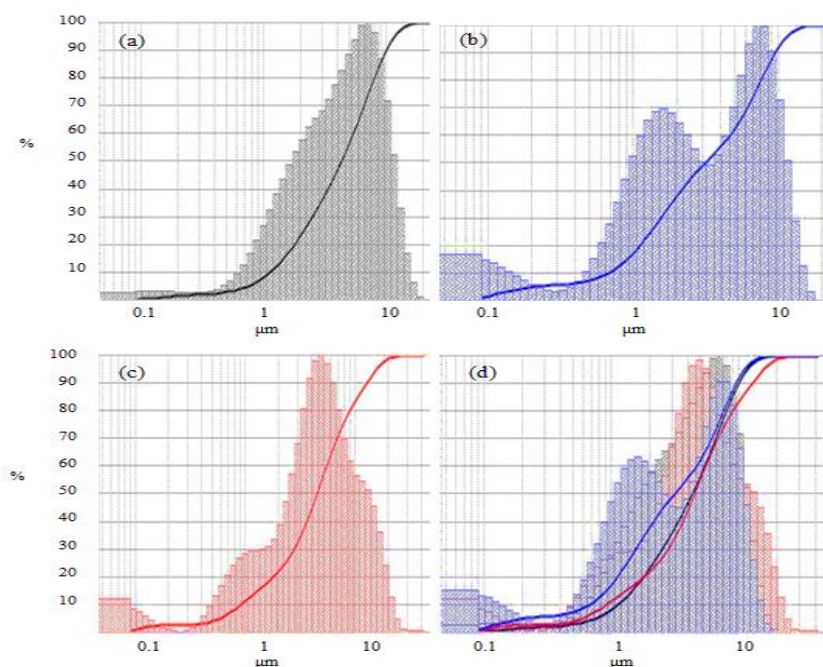
Figure 11 Powder particle size distributions of diatom-derived silica a) Pristine b) Roasted c) Calcined d) all three samples

Table 3. Surface area and Pore radius of different Diatom-derived silica precursors

Samples	Surface area, m^2/g	Pore radius, nm
Pristine diatom-derived silica	100.256	1.69
Roasted diatom-derived silica	37.66	1.69
Calcined diatom-derived silica	77.21	1.87

In anode materials, small particle and crystallite size is vital for optimizing the electrochemical performance of batteries [36]. Recently, a study by Blanco et al demonstrated the effects of particle size on the electrochemical performance of SiO_2/C

nanocomposite as a potential anode material for Li-ion batteries [28]. Here [28], they investigated the effects of ball milling of DE on the electrochemical properties of the negative electrode. The ball milled DE powder showed an increase in specific surface area from 1.2 m^2g^{-1}(pristine DE) to 17.3 m^2g^{-1}. Also, the mean particle size of the ball-milled DE powder was significantly lower (470nm) than the pristine diatom-derived silica (17µm). They also reported an increased presence of mesopores in the ball-milled powder compared to the pristine powder. Blanco et al [28] indicated that although the mesopores could have been present in the pristine powder, they became accessible after ball milling. The powder characteristics reported for the ball-milled powder subsequently influenced the electrochemical performance of the DE-based negative electrode. The negative electrode prepared from the milled diatom-derived silica powder reportedly showed a higher capacity of 750 mAhg^{-1} (milled) than the pristine powder (550 mAhg^{-1}) and this difference was attributed to the shortening of the Li-ion diffusion path and the increased surface area of the powders achieved through particle size reduction.

It is evident from the study by Blanco et al that particle size reduction is an effective tool to improve electrochemical performance in devices and ball milling offers a cheap and simple way to achieve [28]. Although ball milling is ideal for particle and crystallite size reduction, this technique cannot induce any transformations in the Si-O system. As such, the potential of heat treatments to induce transformations and simultaneously reduce particle and crystallite sizes may be ideal for obtaining powders with distinct phases and microstructure.

4.1.2 Phase Composition and Thermal Transformation in Diatom-derived silica

Pristine diatom-derived silica is mostly composed of Opal, as evidenced in the XRD pattern presented in Figure 12a. Naturally occurring diatom-derived silica is amorphous as characteristically shown by the broad "hump" in the diffraction pattern in Figure 12a.
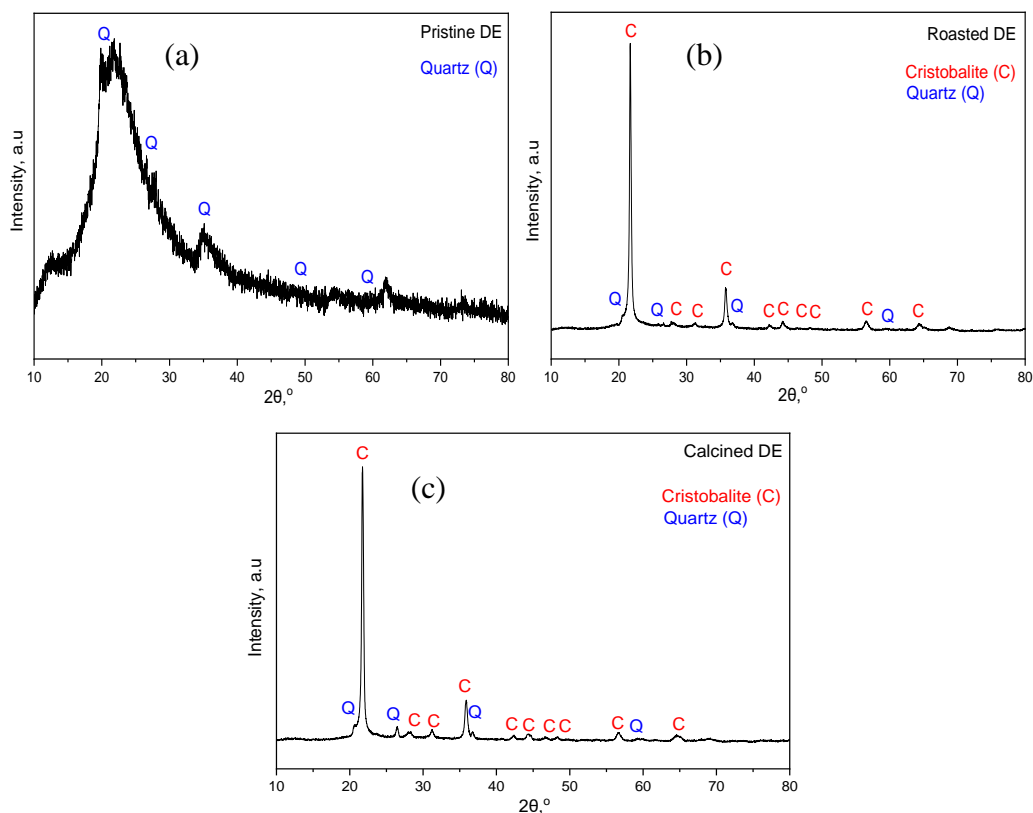
Figure 12 XRD patterns of diatom-derived silica precursors a) Pristine b) Roasted c) Calcined

Also present in the powder, was crystalline quartz together with impurities such clay minerals, iron oxide, carbonate minerals and organic matter, as reported [112] and shown in Table 1. Both heat treatments procedures promoted cristobalite transformation which is confirmed by the very intense peak at 2 theta value of 21.91^{o} in Figure 12b and c. The roasted powder contained 97.37% cristobalite whereas the calcined powder contained 84.53%. From Table 4, 15.47% of quartz was found in the calcined powder. It is not immediately clear the reason for this difference but the present results highlight the effects of heating environments on the phase composition of heat-treated diatom-derived silica.

The main crystalline phase (α-cristobalite with space group $P4_12_12$) in the calcined and roasted diatom-derived silica powders had crystallite sizes of 8.58 nm and

11.44 nm respectively for the as shown in Table 5. The crystallite sizes of the recovered silicon powders were estimated using the Scherrer equation in equation (7), from the FWHM of (101) peak of cristobalite detected by XRD. In equation (7), T is the crystallite size, K is a constant (0.9), λ is the wavelength of the x-ray source, β is the FWHM and θ is the Bragg angle.

$$T = \frac{K\lambda}{\beta \cos\theta} \tag{7}$$

The limited flow of oxygen (argon environment) appears to not only limit coloration but is equally suitable for obtaining small cristobalite crystallites. Coupled with a drastic color change from the brownish diatomite powder to a copper red powder, a bigger crystallite size was obtained for the roasted powder. A similar trend is seen in the recovered Si crystallite sizes for both heat treated powders as shown in Table 6.

Table 4. Phase composition and lattice parameters of powders

Sample	Phase composition, %			Parameters of the crystalline phases			
				Quartz		Cristobalite	
	Opal	Quartz	Cristobalite	a, nm	c, nm	a , nm	c, nm
Pristine DE	76.71	23.29	-	0.4193	0.5405	-	-
Roasted DE	-	2.63	97.37	0.4193	0.5405	0.4971	0.6928
Calcined DE	-	15.47	84.53	0.4193	0.5405	0.4971	0.6928

Table 5. Estimated cristobalite crystallite size

Samples	FWHM (deg)	Scherrer crystallite size /nm
Roasted DE	0.266 ± 0.002	11.44 ± 0.001
Calcined DE	0.354 ± 0.006	8.58 ± 0.05

4.1.3 Thermal Transformation in Diatom-derived silica

The results obtained from the thermal analysis of diatom-derived silica in air and argon are shown in Figure 13. There was no significant weight loss differences observed for the roasted and calcined powders. Initial weight loss of approximately 2.9% was recorded for both roasted and calcined powders measured up to 200°C. This was followed by a second weight loss of almost 1.9% for both powders measured 200°C to 1500°C. Unlike the similar weight losses recorded, the DTA curves for the different heating environments showed totally different transformations that take place during the heating process. In the roasted powder, two exothermic peaks at 493.4^{o}C and 1082.6^{o}C were observed. The calcined powder had exothermic peaks at 753.1^{o}C, 1046.4^{o}C and 1376.7^{o}C. Peaks corresponding to temperatures of about 1082.6 ^{o}C for the roasted powder and 1046.4 ^{o}C and 1376.7 ^{o}C for the calcined powder may be attributed to transformation from opal to cristobalite. In the roasted powder, the exothermic peak at 493.4 ^{o}C may be attributed to the oxidation of organic matter in the powder. It is unclear why the same transformation did not occur in the calcined powder, however, it is clear that limited flow of oxygen impedes the decomposition of organic matter. The peak at 753.1 ^{o}C could also be attributed to the decomposition of the inorganic impurities in both roasted and calcined powders.
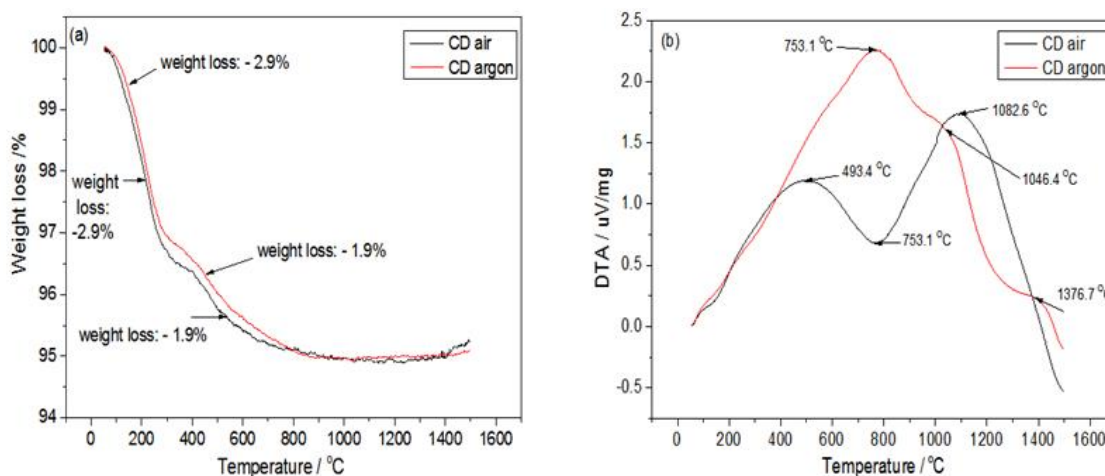
Figure 13 Thermal analysis of as-purchased diatomite in air and argon a) weight loss b) DTA curves

4.1.4 Raman Spectroscopy and Microstructural Analysis of Diatom-derived silica

The Raman spectra of the pristine and heat treated powders are presented in Figure 14 (a, b and c). There were no peaks observed in the pristine powder as shown in Figure 14a. Pristine diatom-derived silica is amorphous and this could explain the absence of peaks in the Raman spectrum. The presence of cristobalite in both calcined powders was evidenced at Raman peaks around 106 cm^{-1}, 228 cm^{-1} and 407 cm^{-1} as shown in Figure14 (b and c).In the case of the roasted powder, extra Raman peaks from magnetite and hematite contributions at 255cm^{-1}, 611cm^{-1}, 673cm^{-1}, 1070cm^{-1} and 1330cm^{-1} are seen as shown in Figure 14b.The contribution of magnetite and hematite peaks in the roasted powder agrees well with the EDS results and provides substantial explanation of the color changes during the roasting process.
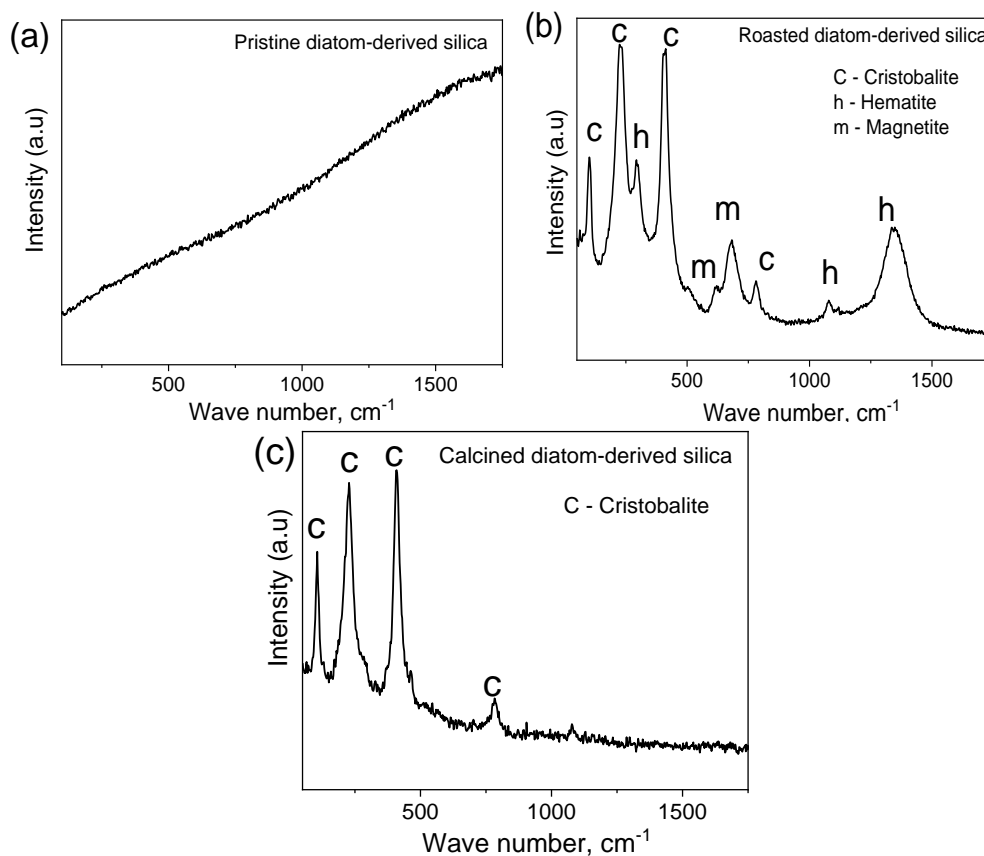
Figure 14 Raman spectra of diatom-derived silica powders a) Pristine b) Roasted c) Calcined

67
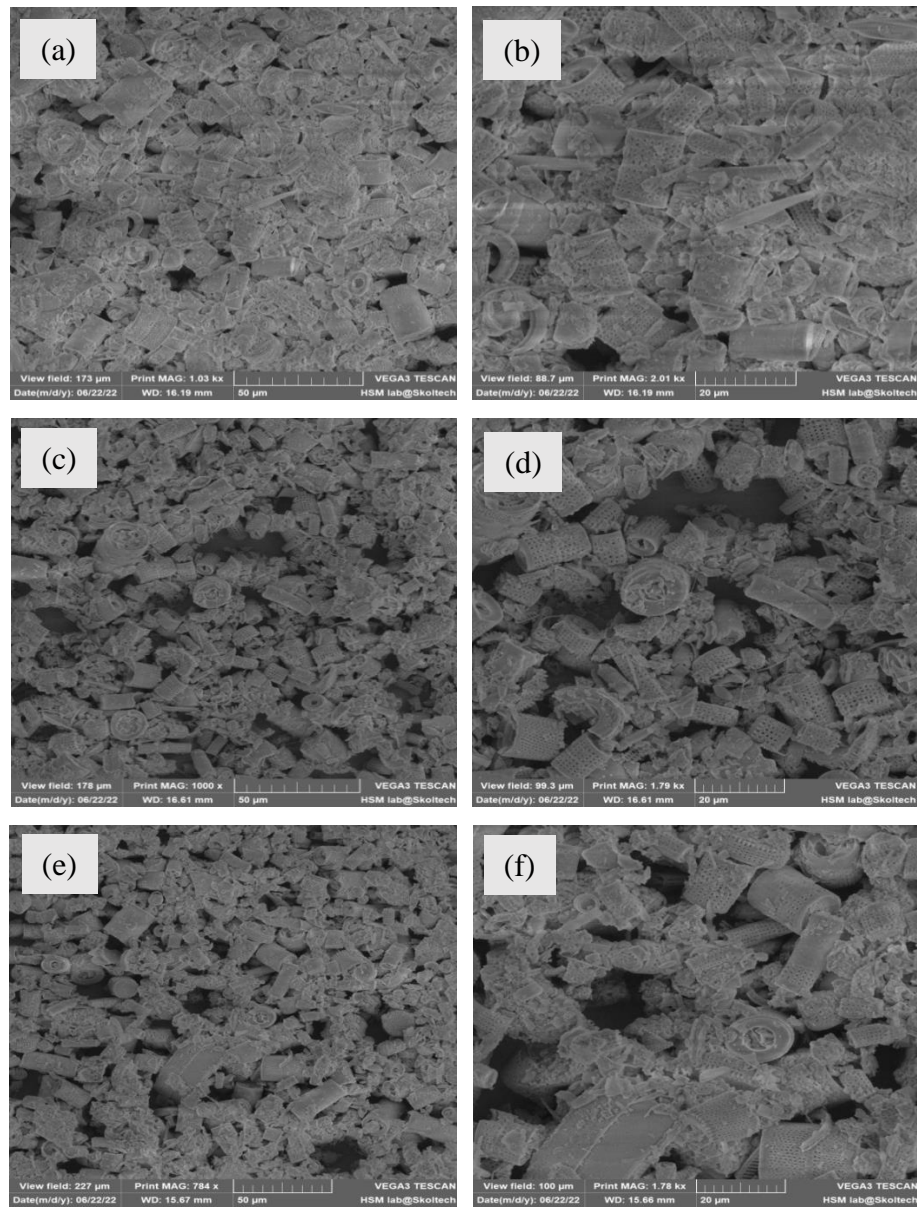
Figure 15 SEM images of diatom-derived silica powders (a and b) Pristine (c and d) Roasted (e and f) Calcined

The microstructure and nano-scale morphology of diatom-derived silica are shown in Figure 15. Despite the expectations that high temperature treatment may cause the collapse of the natural nano-scale architecture of diatomite, SEM analysis of the roasted and calcined powders show that the nano-scale morphology was preserved. What

is more, the roasted and calcined powders appear to have unclogged pores and there is clear indication of the removal of impurities. The porous nature of the heat-treated powders agrees well with the BET pore radii results.

4.1.5 Onset and Exothermic Peak Temperatures of Diatom-derived silica Reduction Reactions

The onset silica reduction temperatures for the three diatom-derived silica powders were studied owing to the significant changes in their powder characteristics after the thermally-induced phase transformation. The measurement was carried out at 2 different heating rates to understand the effects on the onset temperatures for the individual powders. The pristine powder exhibited the highest onset temperature for both heating rates at ~550°C. Both heat-treated powders showed low onset reduction temperatures for the 2 heating rates at ~510°C (roasted) and ~490°C (calcined). As far as the effects of heating rates are concerned, there are no clear differences with the onset temperatures for the respective powders. However, the exothermic peak temperatures for the powders varied significantly with respect to the heating rates. At 10°C/min, all the silica-reduction reactions had exothermic peaks at lower temperatures compared to reactions at 5°C/min as seen in Figure 16a and b.
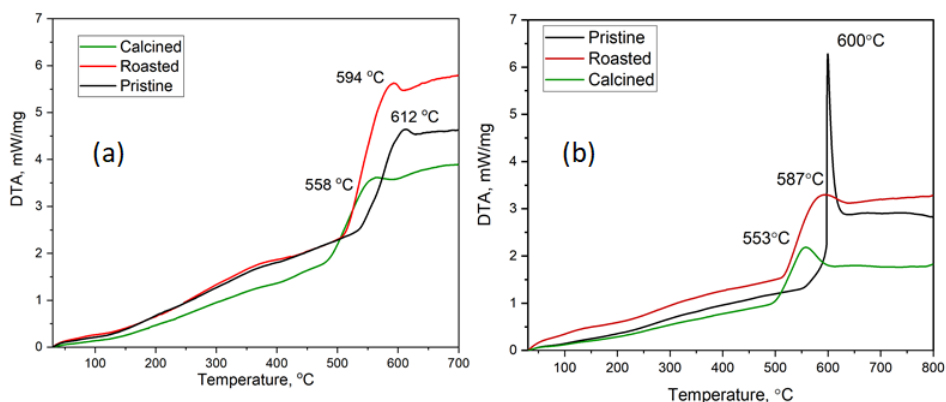
Figure 16 Thermal analysis of magnesiothermic reduction of silica precursors at (a) 5°C/min and (b) 10°C/min

The roasted and calcined powders had exothermic peak temperatures at 594 and 558°C (5°C/min) and 587 and 553°C (10°C/min) respectively. The pristine powder had exothermic reaction peaks at 612°C (5°C/min) and 600°C/min (10°C/min). The effects of thermal treatments of diatom-derived silica on the kinetics of silica reduction reactions illustrated in Figure 16 can be attributed to the significant changes in powder characteristics following the heat treatment regimes. The roasted and calcined powders, regardless of their color differences, had the same crystalline phase (cristobalite). It is known that during the transformation from amorphous silica to cristobalite, there is an increase in the O-Si-O bond angle [113]. As far as the different onset and exothermic peak temperatures are concerned, increase in bond angle is the unlikely cause as it rather leads to shorter bond lengths and eventually stronger bonds. The most likely reason could be differences in the powder characteristics such as reduced particle and crystallite sizes. These powder characteristics could facilitate magnesium diffusion and promote reduction at much lower temperature.

The limited flow of oxygen (argon environment) appears to be critical for obtaining cristobalite with smaller crystallite size. This could be due to the incomplete cristobalite transformation during the calcination process. In the roasted powder, where near-complete cristobalite transformation was obtained, additional energy during the heating process may lead to increased crystallite size. It is clear that, as far as full cristobalite transformation is concerned, roasting is ideal. Calcination on the other hand offers partial cristobalite and quartz phases with smaller crystallite size. Such small silica crystallite may be suitable for applications where diffusion is paramount. The removal of impurities during these heat treatment procedures is an important factor as far as powder characteristics are concerned. It is known that impurities like clay minerals, iron oxide, carbonate minerals and organic matter affect the powder characteristics including specific gravity, bulk density and porosity [112]. They are responsible for an increase in both specific gravity and bulk density and also cause a reduction in porosity of diatomite. Interestingly, most of these impurities are decomposed during calcination and roasting

70

and could account for a relatively better porous structure in the calcined samples than the pristine sample.

4.1.6 Electrochemical charge/discharge curves of Diatom-derived silica Anodes

The effects of thermally induced transformation on the electrochemical performance in diatom-derived silica anodes material were studied. Figure 17 illustrates the calcined diatom-derived silica anodes showed excellent cycling performance against lithium, while the pristine powder showed poor performance after preliminary measurements. Both crystalline powders exhibited superior electrochemical performance (340mAh/g for calcined and 255mAh/g for the roasted powder). Unlike in the amorphous silica anode (168mAh/g) where the specific capacity showed minimal increment with increasing cycle number, the crystalline powders showed remarkable increase in the specific capacity with increasing cycles. All silica powders showed high columbic efficiencies above 95%. Similar capacities and columbic efficiencies have been reported for uncoated silica anodes [28]. The improved electrochemical cycling of the crystalline diatom-derived silica based anodes could be attributed to fast lithium diffusion which is facilitated by small silica crystallites after the thermally-induced phase transformation. The gradual increase in specific capacity is typical for SiO_2 anodes and it has also been attributed to the growth of the electroactive area which is cause by SiO_2 electrochemical milling [28]. Silica is known to be a convertible oxide which undergoes reversible and irreversible conversion reactions to produce silicon, lithium oxide and lithium silicates. As such the reaction between Li-ion and SiO_2 does not involve intercalation, alloy/dealloying or conversion. Lithiation of SiO_2 reportedly leads to the formation of Si, Li_2O and Li_4SiO_4 formation and these phases are known to partially contribute to the overall increase in specific capacity [28]. The formation of such phases during lithiation could account for the increased specific capacity for all the diatom-derived silica anodes. That notwithstanding, the crystalline and amorphous silica forms show dissimilar increasing pattern and this could be attributed to the powder properties and as well as the quantity and kinetics of formation of these phases. Besides the different powder

71

characteristics between the pristine and heat-treated powders, it is unclear the reason for the poor electrochemical performance of the former.
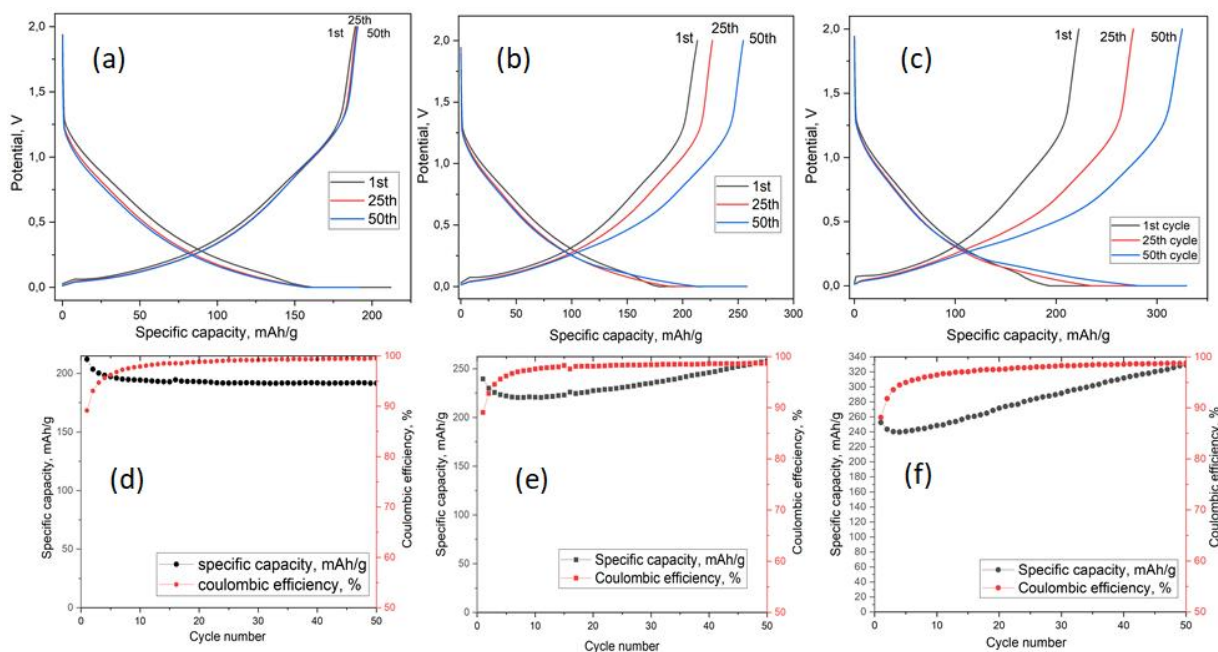
Figure 17 Charge/discharge curves and columbic efficiencies of Diatom-derived silica anodes (a and d) pristine (b and e) roasted and (c and f) calcined

The results presented in this section revealed the effects of thermally-induced phase transformation on several physical and chemical properties of diatom-derived silica. Indeed, both calcination and roasting facilitated significant changes in the powder properties and most importantly highlighted the effects of particular heating environments. The calcined silica powder show superior powder characteristics such as smallest crystallite size, decreased particle size, unclogged pores and most importantly, this powder displayed the lowest on-set and peak exothermic temperature for MRR. Further, Li-ion battery anodes prepared from the calcined powder show the best electrochemical performance. Based on the preliminary results, the calcination of diatom-derived offers the best powder properties for silicon production and direct use as pre-treatment step for silica based anodes when compared to roasted and pristine counterparts. On the other hand, roasting of silica could substitute calcination in cases

72

where controlled heating is impossible. Roasting offers a cheaper and straightforward way to modify the powder properties. Both calcination and roasting offer unclogged pores by decomposing impurities trapped within the pores. The roasted powders showed better powder characteristics, electrochemical performance and lower on-set reduction temperature than the pristine powder.

4.2 Nanostructured Si recovered from different precursors

One of the key research areas in diatom-related studies is the recovery of silicon from this siliceous precursor. Diatom-derived silica serves as an ideal silica precursor due to its fascinating nanostructure. The naturally formed neat nanostructure is highly recommended to remedy challenges faced with silicon-based materials in various applications [17,35,51,52,114,115,116]. Here, the phase composition, powder characteristics and morphology of silicon recovered from the pristine, roasted and calcined diatom-derived silica powders were studied. The significant changes observed in the silica precursors as a result of the different thermal treatments influenced the morphology of the recovered Si powder to a large extent. An in-depth understanding of the effects of such thermal pre-treatments could provide sufficient information for the synthesis of silicon-based materials to meet certain functional applications. A recent review on magnesiothermic reduction of diatom-derived silica captured the effects of reaction time and temperature on the crystallite size of product silicon [36]. Increasing reaction temperature and time tend to increase crystallite size by providing more energy to induce sintering and grain growth for silicon crystallites. Another interesting study identified higher porosity and surface area as critical for obtaining silicon with small crystallite size [38].

Silica precursors with high porosity and surface area are thought to be a hindrance to mass transport during the reduction process which slows down coarsening of the silicon crystallites. It is clear from this report that powder characteristics of precursor diatom-derived silica are crucial for creating silicon-based materials with specific properties. In this study, a similar trend is observed, as different silica precursors led to

silicon with powder characteristics. In Tables 6 and 7, the crystallite sizes, pore radius and surface area of the silicon powders obtained from the individual Si powders are provided. The smallest silicon crystallite size was obtained from the calcined diatom-derived silica with the pristine diatom-derived silica powder offering silicon with the biggest crystallite size. As earlier reported, precursor powders with high porosity and surface area provide the right counter mechanism to prevent coursing of the silicon crystallite by impeding mass transport. The effectiveness of both thermal pre-treatment procedures in unclogging frustules leads to a highly porous powder which explains which heat-treated silica the ideal precursor for producing nanostructured Si. The recovered Si powders are denoted as Si@ (PD, RD or CD) for silicon recovered from pristine, roasted and calcined diatom-derived silica respectively.

Table 6. Estimated silicon crystallite size

Samples	FWHM (deg)	Scherrer crystallite size /nm
Si@PD	0.143 ± 0.003	27.46 ± 0.09
Si@RD	0.172 ± 0.006	22.93 ± 0.06
Si@CD	0.244 ± 0.016	16.14 ± 0.02

Table 7 Surface area and Pore size of different recovered Si powders

Samples	Surface area, m^2/g	Pore size, nm
Silicon @ PD	60.27	1.68
Silicon @ RD	32.64	2.17
Silicon @ CD	10.22	4.7

4.2.1 Phase Composition and Microstructure of Recovered Silicon

The post-reduction powders appeared coffee brown as shown in Figure 18b and contained Si, MgO, NaCl and unreacted SiO_2. The XRD patterns provided in Figure 19 confirmed the presence of Si, MgO, NaCl and unreacted SiO_2. It is evident from Figure 19 (a) that pristine diatom-derived silica is amorphous as no peaks of cristobalite are seen, unlike in the case of both calcined and roasted forms of the powder in Figure 19 (b

and c). Clearly, the role of the heat scavenger in limiting the formation of Mg_2Si and Mg_2SiO_4 through temperature management is seen here. It has been reported that such unwanted by-products are facilitated by several reactions conditions including temperature. Scavenging excess heat from the highly exothermic reduction reaction not only improves chances of structural control but ultimately determines the composition of the post-reduction powder.
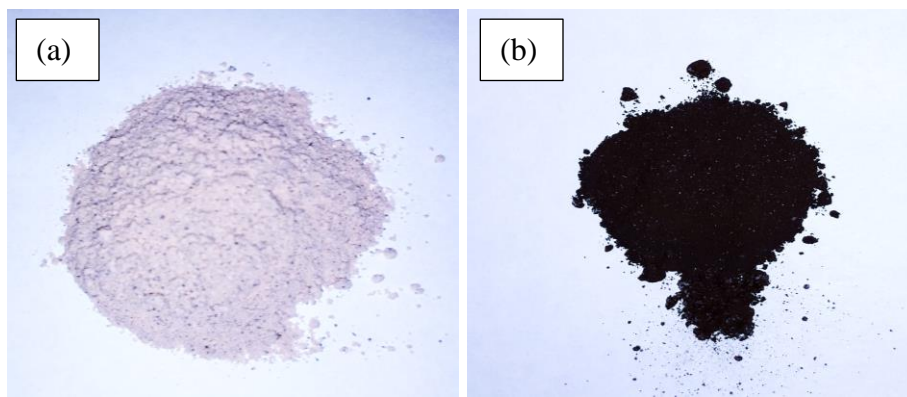
Figure 18 Reaction powder (SiO_2+Mg+NaCl) (a) before reduction (b) after reduction

It must be mentioned that in some related cases, where Mg_2Si was sought, no heat scavenger was used as its use could retard the formation of the former. For all the post-reduction powders, a purification process involving several steps of 1M HCL and 5% HF etching were performed, followed by rinsing in distilled water. The resulting purified powders were dried in a vacuum oven overnight at 85^oC. The analysis of the powders with XRD confirmed the presence of major phase Si with 28.4^o, 47.3^o, 56.1^o, and 76.4^o reflections, corresponding to (111), (220), (311) and (331) planes of diamond-structured silicon with traces of unconverted silica. The crystallite sizes of the recovered silicon powders were estimated using the Scherrer equation in equation (7).
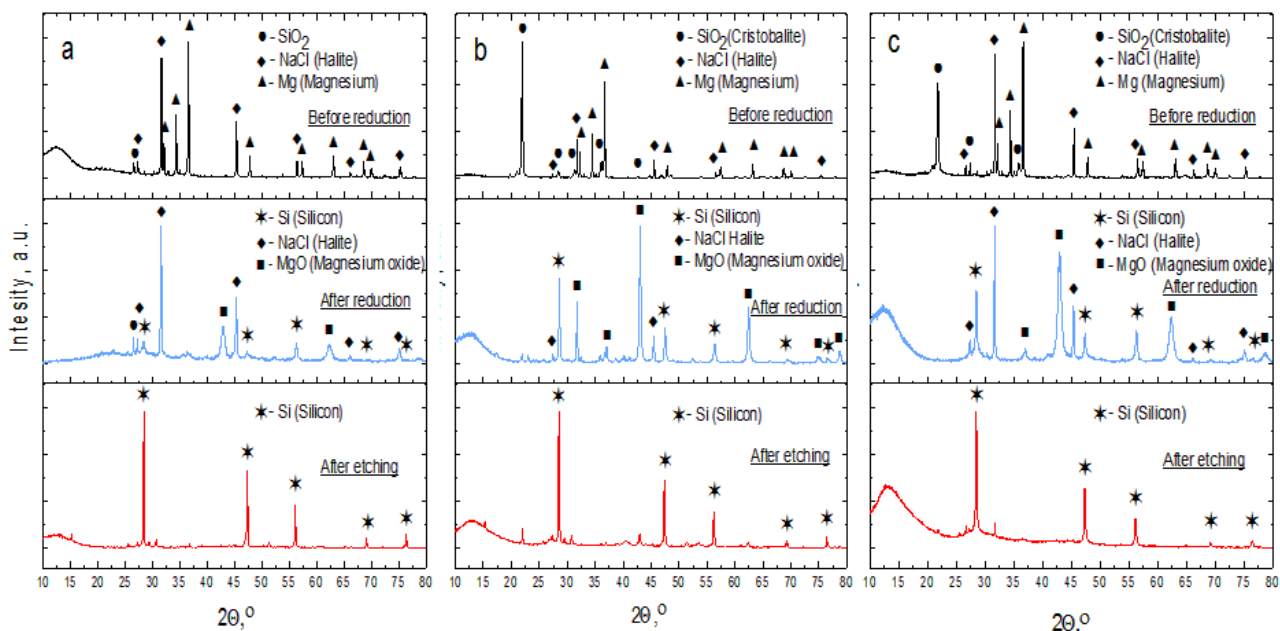
Figure 19 XRD patterns of powders before and after magnesiothermic reduction a) Pristine b) Roasted c) Calcined

To better understand the effects of thermal pre-treatments of silica on recovered Si-based materials, the morphology of the silicon powders where studied. The microstructural images of silicon obtained from the different silica precursor show the destructive nature of the highly exothermic displacement reaction, although quite significant differences in their morphology can be deduced. Even with the use of a heat scavenger, the extent of damage to the neatly formed nanoporous structure of diatom-derived silica is evident. The calcined powder offered the least structural damage in the recovered silicon with silicon@pristine diatom-derived silica showing the most structural damage as shown in Figure 20.
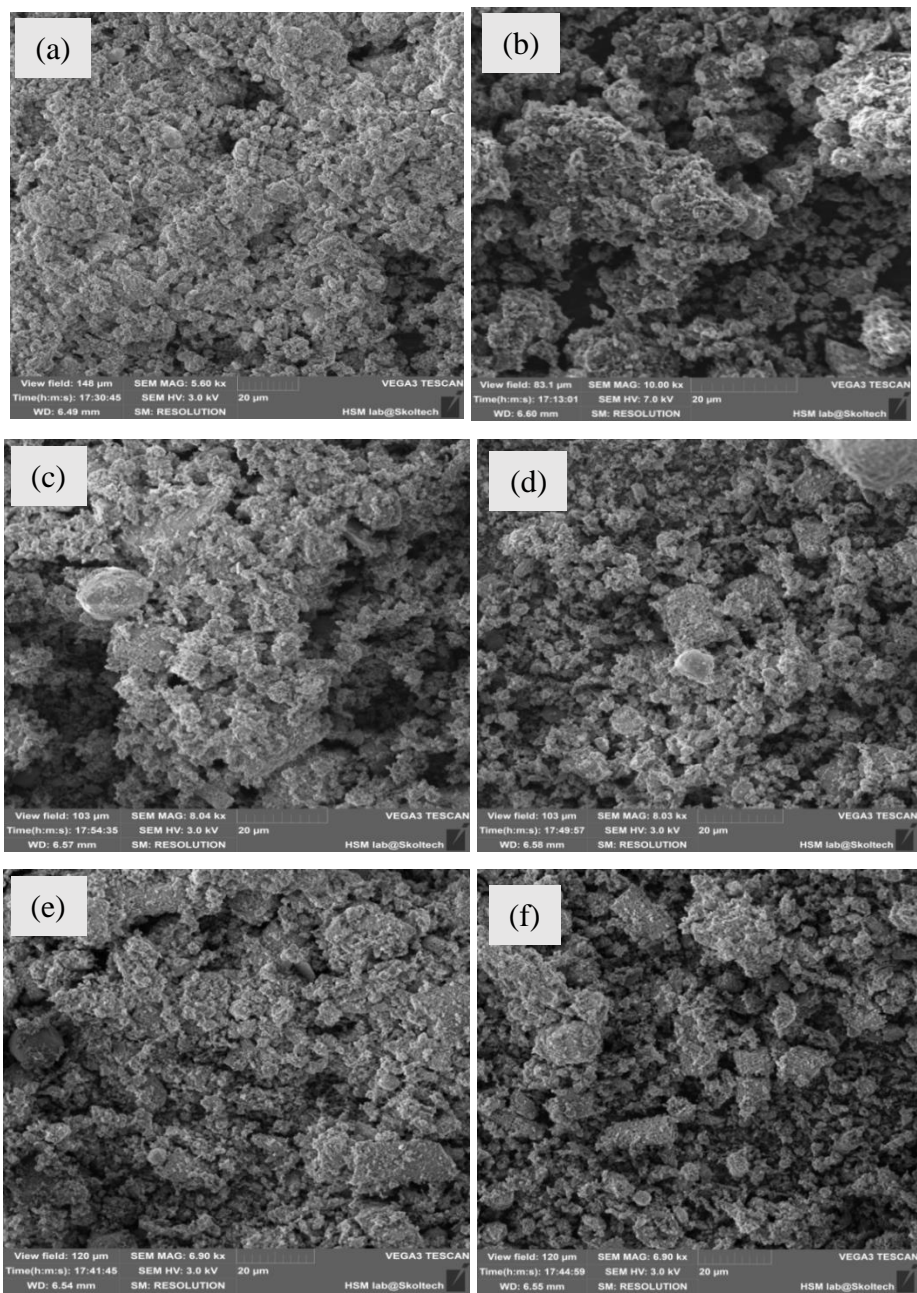
Figure 20 SEM images of recovered Si powder from their respective silica precursors (a and b) pristine (c and d) roasted and (e and f) calcined

Another useful materials characterization technique used to confirm the presence of silicon and reveal inherent difference between the different silicon powders was Raman Spectroscopy measurement. The Raman spectra of the silicon powders showed

first order Raman peaks at approximately 507cm^{-1}, 513cm^{-1} and 501cm^{-1} for the si@pristine, si@roasted and si@calcined diatom-derived silica powders respectively as shown in Figure 21. No significant variations were observed for the second order Raman peaks of the three powders. Even though the sharp Raman peaks shows the crystalline nature of the nanostructured silicon, the differences in peak positions can be related to the level of crystallinity in the silicon sample. Si@roasted showed the highest state of purity as it was the closest to the Raman peak position of high-purity mono-crystalline silicon at 521cm^{-1} peak position while nanostructured silicon from the calcined had the peak position furthest from this value. These results suggest that si@roasted shows the highest level of crystallinity as it is the closest to the Raman peak of high purity monocrystalline silicon.
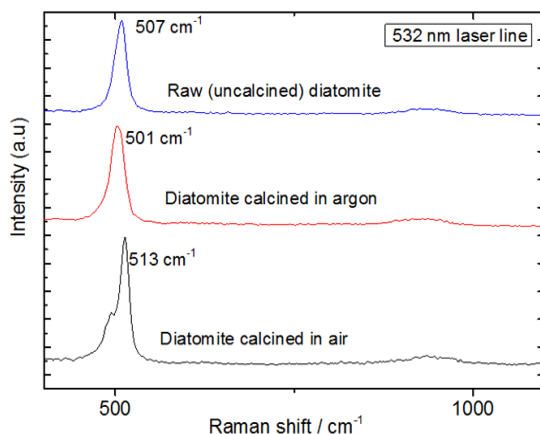
Figure 21 Raman spectra of silicon recovered from different diatom-derived silica precursors

4.2.2 Electrochemical charge/discharge curves of Recovered Silicon

The electrochemical cycling of recovered silicon and their bulk counterpart was studied and results presented in Figure 22. Unsurprisingly, the bulk silicon anode exhibited rapid capacity loss, very typical of this silicon type. This is a well-known phenomenon in bulk silicon anodes which is attributed to huge volume expansions during charge/discharge cycles. These volume expansions (~ 300%) results in cracking and delamination and subsequently leads to poor performance. Silicon based anode

78

synthesized from the calcined diatom-derived silica showed better electrochemical cycling by providing high capacity retention. Clearly, the nanostructured architecture offers better structural stability compared with bulk silicon. The nanostructured Si anode displayed a high discharge capacity of 1000mAhg^{-1}, an order of magnitude higher than the bulk Si anode (100mAhg^{-1}) after 20 charge/discharge cycles. The nano-Si and bulk Si anodes had columbic efficiencies well above 97%. The electrochemical performances shown here agree well with previously reported performance of bulk and nano-Si negative electrodes.
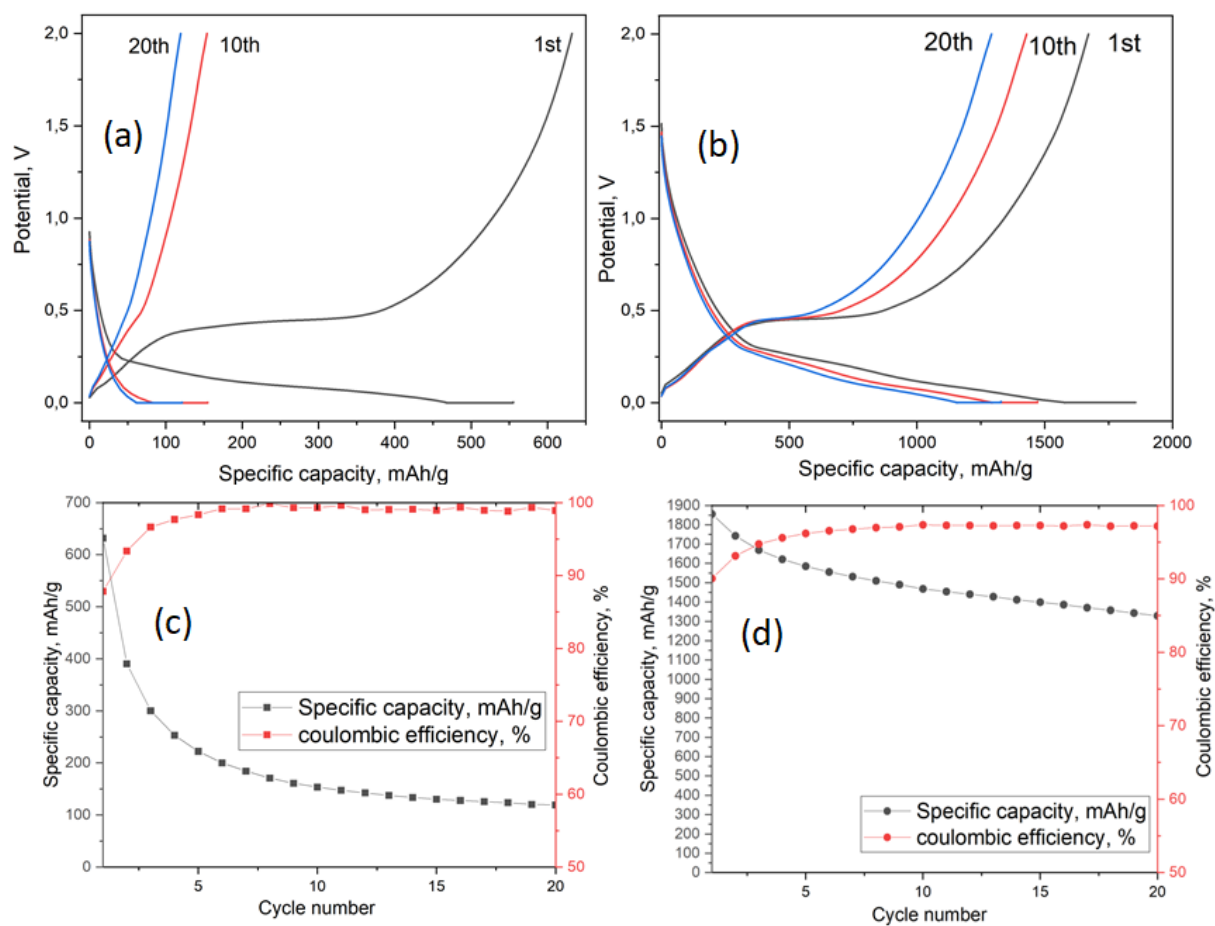
Figure 22 Charge/ discharge cycles and columbic efficiencies of silicon anodes (a and c) bulk silicon (b and d) silicon recovered from calcined diatom-derived silica

The recovery of silicon with nanoscale morphologies from diatom-derived silica shows promising prospects as far as the search for high energy density anodes are concerned. Preliminary electrochemical performance of recovered Si and bulk Si-based anodes clearly shows the effects of Si microstructure on the battery properties. What is more, this section demonstrates the effects of thermally-induced phase transformation in the Si-O system on the powder characteristics and morphology of the recovered Si powder. Based on these findings, calcined diatom-derived silica precursor emerges as the most suitable candidate as far as the recovery of silicon with superior nanoscale morphologies is concerned. This calcined diatom-derived silica powder also presents the lowest on-set and peak exothermic MRR temperature that could ultimately reduce the local temperature during the reduction reaction. A significant reduction in the designated reduction temperature could promote structural control and limit the formation of unwanted by-products.

Chapter 5 Porous Si Consolidates and Nanocomposite Si/a-C Anti-Reflective Coatings

5.1 In situ formed Silicon nanoflakes

Creating nano- or micro- porous silicon surfaces has attracted a lot of attention over the last decade due to their fascinating properties compared with their bulk counterparts. In addition to these interesting properties, nanostructured surfaces provide a unique pathway for further functionalization to counter setbacks in optical, optoelectronic, energy harvesting, storage and sensing applications by providing suitable surface morphologies and features. For these reasons, the quest for facile and cost effective ways to synthesize nanostructured Si surfaces is highly sought after. This part of the present study explored an unconventional route (magnesiothermic reduction of silica) to create nanostructured silicon surfaces as earlier shown in Figure 4. The resulting thin Si coating had a close visual resemblance with BSi as shown in Figure 23a.

5.1.1 Microstructure of Silicon nanoflakes

A photograph of the modified silicon wafer surface after the preliminary *in situ* reduction reaction is presented in Figure 23e. Microstructural images of the modified surface, otherwise known as silicon nanoflakes are shown in Figure 24a–f. From the microstructural images an array of irregular peaks and valleys can be seen, which is dissimilar to the regular pattern normally associated with BSi. In addition to the highly rugged surface of the modified surface, a specific highly ordered feature of the retained from the precursor diatom-derived silica can be seen as shown is Figure 24d. The nanoporous nature of this ordered feature is shown in Figure 24e,f with a pore size of around 450nm. Further EDS analysis of the microstructures shown in Figure 25 confirmed the presence of silicon with minor traces of magnesium.
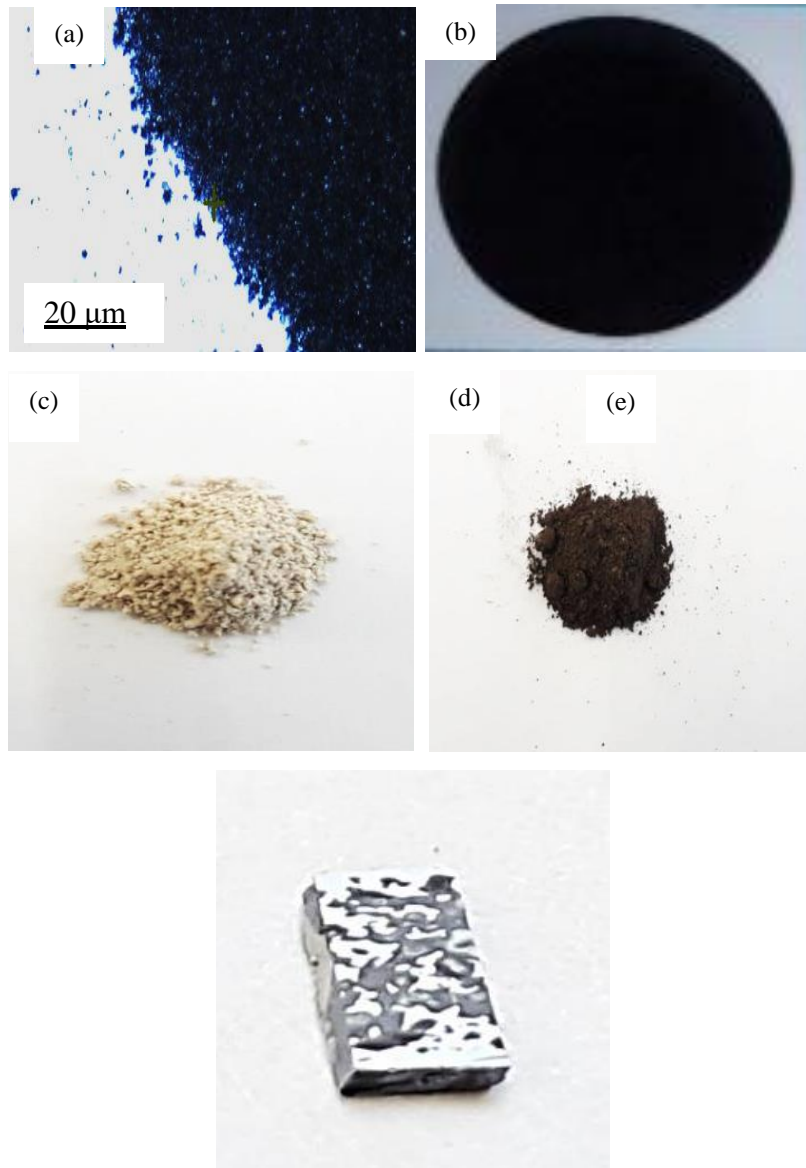
Figure 23 Optical image of texture silicon surfaces (in dark) and bright part as bare Si wafer surface (a) this work (b) BSi produced via laser treatment reported in previous literature (Silicon plate with dimension 25x25 mm) [95] Photograph of (c) reaction mixture before reduction, (d) remaining loose powder after reduction (e) silicon substrate surface after the reduction
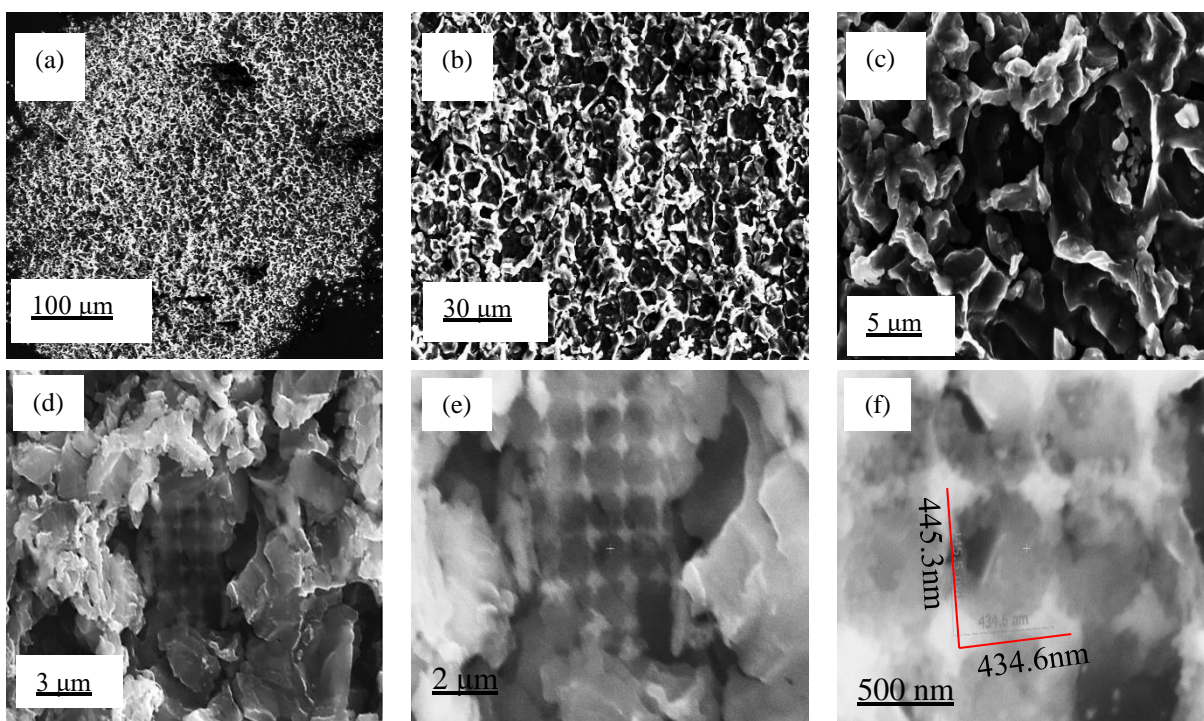
Figure 24 SEM images of the as-etched Si nanoflakes: (a) very low magnification surface view, (b) low magnification surface view, (c) large magnification surface view, (d) specific highly ordered feature, (e) large magnification of a specific highly ordered feature, and (f) nanoporous nature of a specific highly ordered feature.

In Figure 25d and e, SEM images of the adhesion scratch test of the nanocrystalline Si coating on Si wafer substrate are presented which shows good bonding was achieved, resulting in a 'ploughing' response without any spalling off of the coating. The initial thickness of the silicon nanoflakes as estimated from FIB analysis was 5.7μm. The microstructural images of the coating cross-section are shown in Figure 26a-d. The cross-sections show irregular peaks and valleys of the silicon nanoflakes. Also, very few flakes possessed some nanoporous details from the precursor diatomite powder. On the contrary, there existed micropores and cavities between flakes of different layers and orientations.
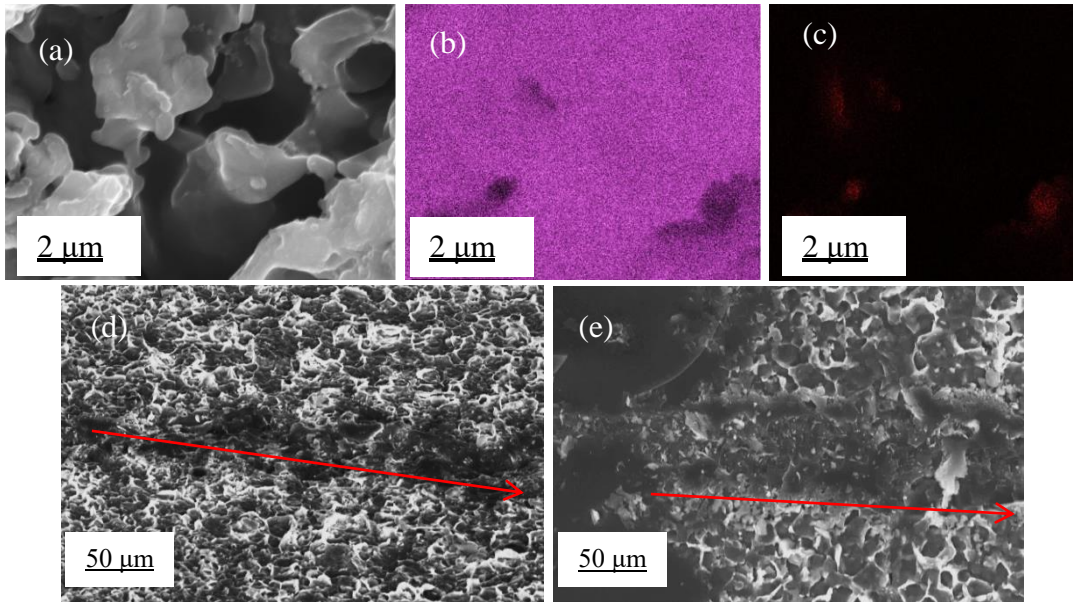
Figure 25 EDS elemental mapping (a) SEM image of nanoflakes, (b) Si, (c) Mg < 1% average and SEM images of the as-etched silicon nanoflakes (a) scratch path through silicon nanoflakes at low magnification (b) scratch path silicon nanoflakes at high magnification (red arrow showing scratch path)
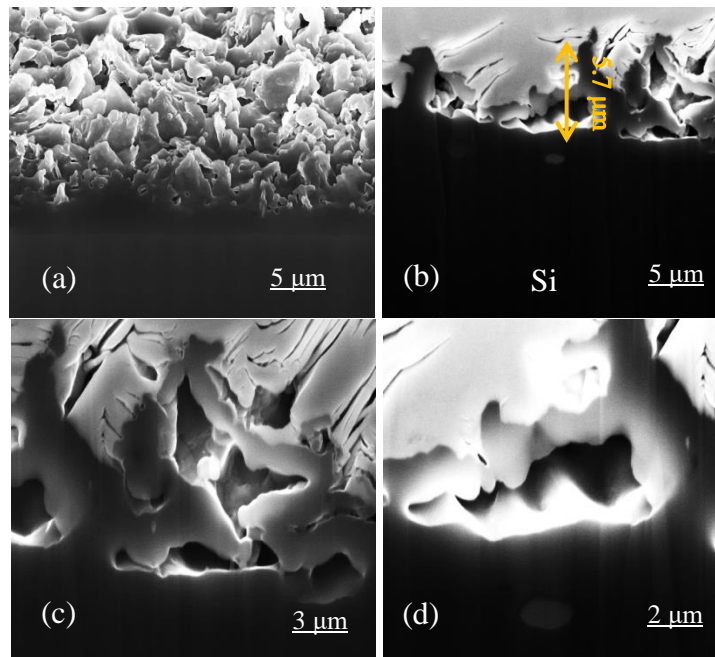
Figure 26 FIB-SEM cross-sectional images of silicon nanoflakes (a) low magnification without Pt coating (b) low magnification with Pt coating (c) large magnification showing micro-pores and cavities (d) magnified SEM image of cross-section

5.1.2 Phase Composition of Si nanoflakes

The XRD pattern of the as-purified silicon nanoflakes clusters formed directly on the single crystalline silicon wafer substrate is shown is shown in Figure 27. From the diffraction pattern, no contribution from the substrate was seen since all Bragg conditions were not fulfilled. The diffraction peaks of silicon were observed, however, characterized by high backgrounds and low intensity peaks associated with nano-crystalline and/or amorphous nature of the silicon nanoflakes.

A number of reaction routes are possible in the direct formation of the silicon nanoflakes. In the MRR, the main reaction was between silica and magnesium as shown in Equation 1 and Figure 1. However, the possibility of forming Mg_2Si between the silicon wafer and magnesium was also likely in this synthesis route. In the event of Mg_2Si formation, a continuous reduction of the closest SiO_2 particles by Mg_2Si was likely to occur. Mclean et al. reports of a high yield in silicon achieved at a higher temperature with an Mg stoichiometric ratio increased above 2:1 [70]. The increased Mg stoichiometric ratio favored the formation of Mg_2Si. As a result, more silicon was produced through the solid state reduction of unreacted SiO_2 by Mg_2Si as shown in Equation 2.
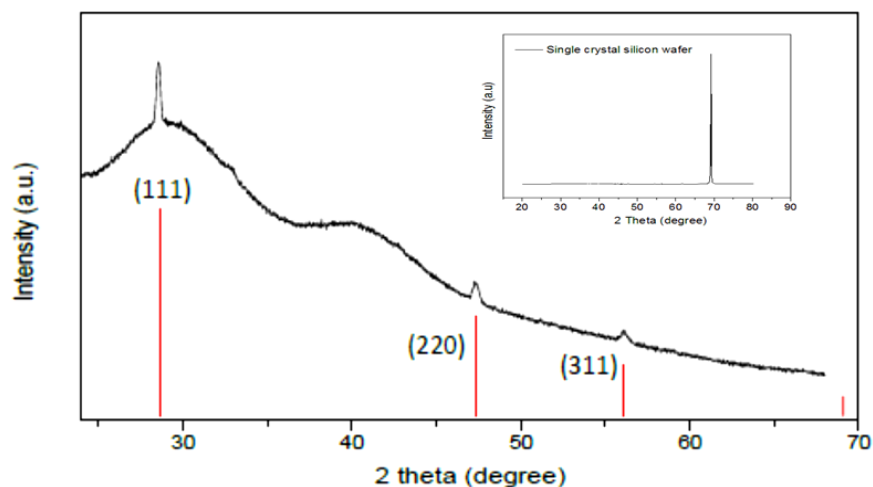
Figure 27 XRD pattern of the as-etched silicon nanoflakes. Inset: XRD pattern of the n-type silicon wafer with orientation (001)

In this case however, Mg:SiO$_2$ molar ratio of 1.25:1 shows that the possible Mg$_2$Si formation was not due to a higher Mg stoichiometric ratio above 2:1. Rather, a direct contact between the Si substrate and Mg particles might lead to the formation of Mg$_2$Si as shown in Figure 6. The Mg$_2$Si formed in such a case is then likely to reduce surrounding SiO$_2$ particles as shown in Equation 2.

5.1.3 Raman Spectra of Silicon nanoflakes

The Raman spectra of both monocrystalline silicon and silicon nanoflakes are shown in Figure 28. Both first and second order scattering of silicon are observed in the spectra. The intensities however differ. Raman intensity of the silicon nanoflakes was relatively higher than that of peaks from bulk silicon.
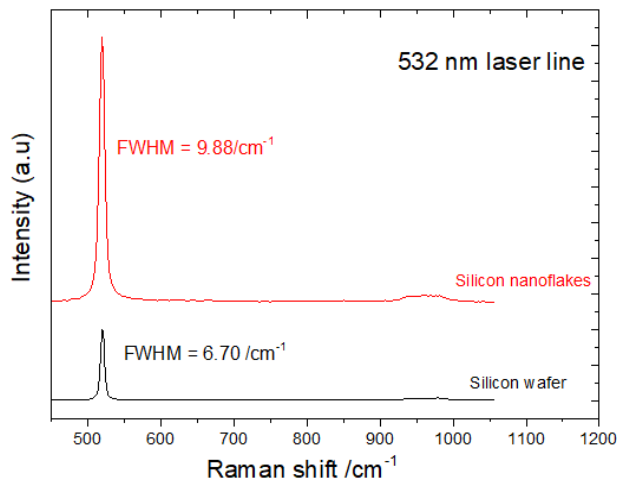
Figure 28 Raman spectra of silicon wafer and the as-etched textured Si surface (silicon nanoflakes)

This could be related to the effects of nanolayers of ultrathin silicon flakes formed after the Magnesiothermic reduction reaction. Raman intensities studies of MoS$_2$ monolayers by Li et al showed that intensities of the monolayers were relatively higher than the bulk MoS$_2$ and varied arbitrarily according to the number of layers [117]. Also,

86

Zuo et al reported that, Raman enhancement was observed from conical cavity arrays [118]. They attributed this phenomenon to the significant Raman enhancement of molecules on the cavity walls. Cross-sectional analysis of the silicon nanoflakes via FIB milling showed the presence of pores as seen in Figure 26. These factors may account for the huge difference in intensities between silicon nanoflakes and the silicon wafer surface.

5.1.4 Atomic Force Microscopy Studies of Silicon nanoflakes

The topography and surface potential measurements of silicon nanoflakes are presented in Figures 29 and 30. As already shown in the SEM microstructural images and FIB sections, there is a significant variation in the thickness of the silicon nanoflakes formed. These variations are further confirmed by AFM topography. The underlying silicon wafer substrate of n-type conductivity had electrical resistivity between 3.6-5.3 ohm-cm.
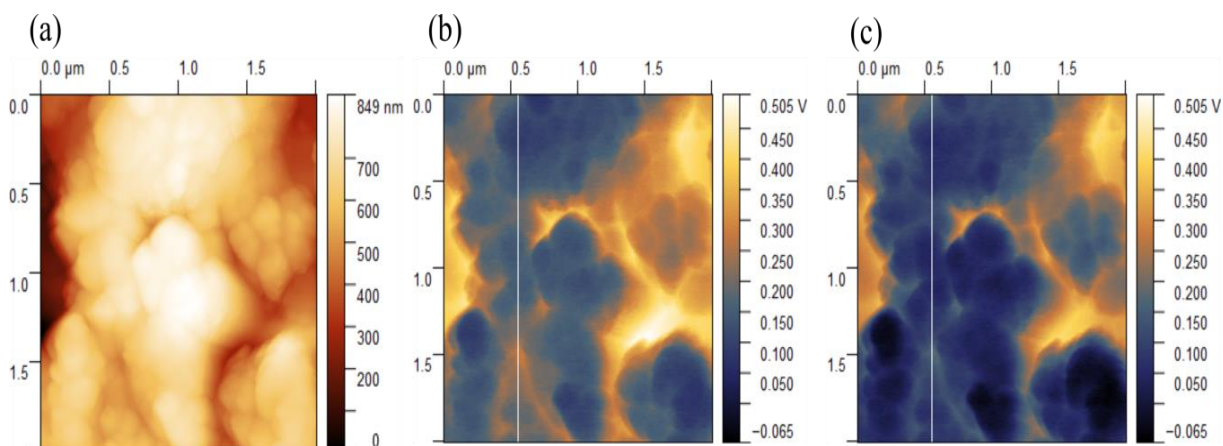
Figure 29 (a) AFM topography and (b) KPFM map of the as-etched silicon nanoflakes under dark conditions (c) KPFM map of silicon nanoflakes under illumination condition
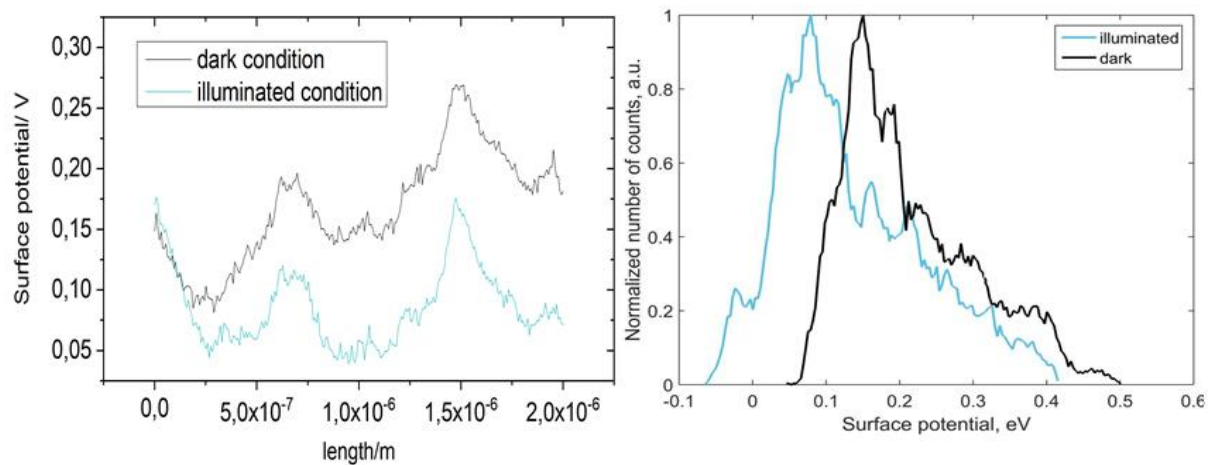
Figure 30 Graph of (a) the V_{CPD} profiles of the as-etched silicon nanoflakes under dark and illumination conditions and (b) V_{CPD} distribution

The surface potential measurement was performed to understand the doping type of the silicon nanoflakes. The formation of a depletion region in a p–n junction is known to suppress the recombination of electrons and holes generated upon excitation with photons from a light source. Measured surface potential values are related with the work function of materials, which also relates directly to the doping type of a semiconductor. Under super band gap illumination, band bending of the depleted surface decreases, which may be detected by a shift of surface photovoltage. This shift is opposite for n- and p-type semiconductors. Although, our results (Figures 29 and 30) might suggest that the silicon nanoflakes were n-type, the dopant in this case was not easily identified. Food grade diatomite powders (such as used in this research) are known to contain trace elements of phosphorus [120] at concentration below the detection limit of the EDS analysis. The diffusion of a dopant from the substrate into the nanoflakes is also a route for doping of in situ synthesized nanoporous silicon.

88

5.1.5 Optical Properties of Silicon nanoflakes

The silicon nanoflakes recovered from pristine diatom-derived silica suppressed light reflection to less than 15% in the infrared region compared to the 45% light reflection from the c-Si wafer surface. Like black silicon, silicon nanoflakes simultaneously enhance light trapping. The reported surface reflection for different black silicon surfaces produced via different routes is between 5-32% in the visible and near infra-red range of the electromagnetic spectrum [95]. The optical properties of the silicon nanoflakes compare favourably with black silicon and shows similar light trapping mechanism. In the case of black silicon, the peaks and valleys are known to be responsible for the enhanced light absorption, as incident photons are reflected into the peaks and absorbed by the materials. The reflectivity of materials as reported by Stephens and Cody [119], are greatly reduced by light trapping through multiple reflections. With the Si nanoflakes, both irregular peaks and valleys and some pores contribute to the overall decrease in surface reflection of the silicon wafer. The initial optical property measurement was limited to the infrared region due to coverage range of the device. In subsequent optical property measurements, light absorption and reflection were measured in the visible and near-infrared regions.

5.2 Bi-layered Functional Coatings

The section presents results on the optimization of the in situ reduction process together with the facile phase separation process to create bi-layer textured Si and amorphous carbon nanocomposite

5.2.1 Optimization of the *in situ* MRR of diatom-derived silica on silicon substrate

Following the successful creation of a silicon coating with nano-to-micro-scale morphologies directly on a silicon substrate via the *in situ* magnesiothermic reduction of diatom-derived silica, it became imperative to optimize the procedure to address all

setbacks of this technique. Despite the early successes reported, the final product had significant impracticable features such as non-uniform and cluster-like silicon coatings on the substrate. These characteristics of the textured Si coating were not suitable for further functionalization of the silicon nanoflakes and subsequent studies of the properties. To address these setbacks, the kinetics of the *in situ* magnesiothermic reduction of diatom-derived silica was studied. Summary of the kinetics study is provided in Table 8. It must be noted that, a heat scavenger (NaCl) was not used in the kinetics study. From the table 8, uniform silicon coatings were obtained after the magnesiothermic reduction of diatom-derived silica with mass ratios ($Mg:SiO_2$) 1.5:1 and 2:1 at $750^{o}C$ for 6 hours. The synthesis at $450^{o}C$ yielded no silicon coating at all, regardless of the Mg/SiO_2 mass ratio. At temperatures $550^{o}C$ and $650^{o}C$, the reaction yielded different products (Si or Mg_2Si) with specific characteristics depending on the Mg/SiO_2 mass ratio. Based on these findings, the surface of silicon substrates were successfully modified with silicon nanoflakes as shown in Figure 31d. The silicon coating was uniform and covered the entire wafer surface. These results are desirable for further functionalization with active materials and subsequent material properties and performance measurements.

Table 8. Summary of kinetics study of the *in situ* MRR of diatom-derived silica

Mass ratio _Mg/SiO_2	$450^{o}C$	$550^{o}C$	$650^{o}C$	$750^{o}C$
0.5:1	-	-	Tiny islands of Si coating	Tiny islands of Si coating
1:1	-	Islands of Mg2Si coating	Islands Si coating	Islands Si coating
1.5:1	-	Uniform Mg2Si coating	Uniform Mg2Si coating	**Uniform Si coating**
2:1	-	Uniform Mg2Si coating	Uniform Mg2Si coating	**Uniform Si coating**
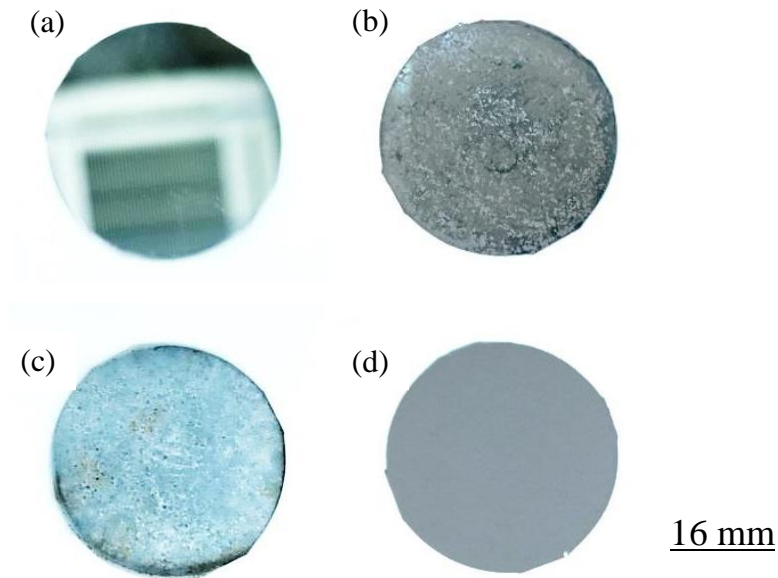
Figure 31 Surface of silicon substrate before and after the *in situ* magnesiothermic reduction of silica (a) mirror-like silicon wafer surface before surface modification (b) cluster of silicon flakes (c) uniform Mg2Si after optimization (d) uniform silicon nanoflakes after optimization (coin diameter of 16mm)

5.2.2 Phase Composition of Bi-layer Textured Si and amorphous nanocomposite

The highly exothermic reaction between Mg and SiO_2 leads to several feasible outcomes, notably Si, Mg_2Si, MgO, and Mg_2SiO_4 [36]. The formation of these products highly depends on the tunable reaction conditions such as reaction temperature, time and mixing ratio [36]. The textured surfaces showed the presence of a single phase, Si, formed on the single crystalline Si wafer surfaces from XRD analysis. Although this reaction is mostly accompanied with by-product MgO, Mg_2Si, and unreacted SiO_2, no traces of these phases were detected in the diffraction pattern in Figure 32. The high intensity peaks shown in Figure 32(ii) suggests the textured silicon surface is nanocrystalline with 28.4^o, 47.3^o, 56.1^o, and 76.4^o reflections, corresponding to (111), (220), (311) and (331) planes of diamond-structured silicon. Also featured in the

diffraction pattern is an intense peak at 69.2^{o}, associated with the reflection from the (400) plane of the c-Si substrate shown in Figure 32(ii). The absence of MgO diffraction peaks on the textured silicon wafer surface, which might not be detected by XRD analysis if present in trace quantity, confirms the key role of the intermediate Mg_2Si phase formation.

The deliberate formation of Mg_2Si followed by air oxidation to obtain Si and minor quantity of MgO was previously reported by Liang et al [81,121]. In these studies [81,121], they reported a greater yield in Si and simultaneous decrease in the MgO content with almost no unreacted SiO_2 after the synthesis process. This is unlike the direct SiO_2 to Si magnesiothermic reductions, where less Si yield is recorded due to the presence of leftover SiO_2, by-product MgO and unwanted Mg_2Si [59,69,76,122]. Although, the pre-formed Mg_2Si is crucial in achieving a uniform nanostructured silicon coating, there are huge concerns of Mg contamination of the substrate and the textured Si coating. To obtain high purity Si coatings, a purification process involving 1M HCl, 5% HF and distilled water washing was carried out successively. This could effectively remove unwanted by-product, but trace amounts trapped within the depth of the textured-Si film may remain unwashed. The porous carbon film formed following the carbonization of the PAN showed two broad peaks centered at 31° and 42°, which are close to the characteristic peaks of activated carbon at peaks position 24° and 42°, and correspond to the reflection from planes (002) and (100) as presented in Figure 32(i) [123]. The hump confirms the amorphous state of the porous carbon film. Notable from the XRD pattern in Figure 32(i) is the huge shift from the reference peak position $2\theta= 24^{o}$ to 31°, which some accounts attributed to a thermodynamically driven structural rearrangement from a highly disordered state to short-range order as the interplanar distances between the (002) planes decrease [124].
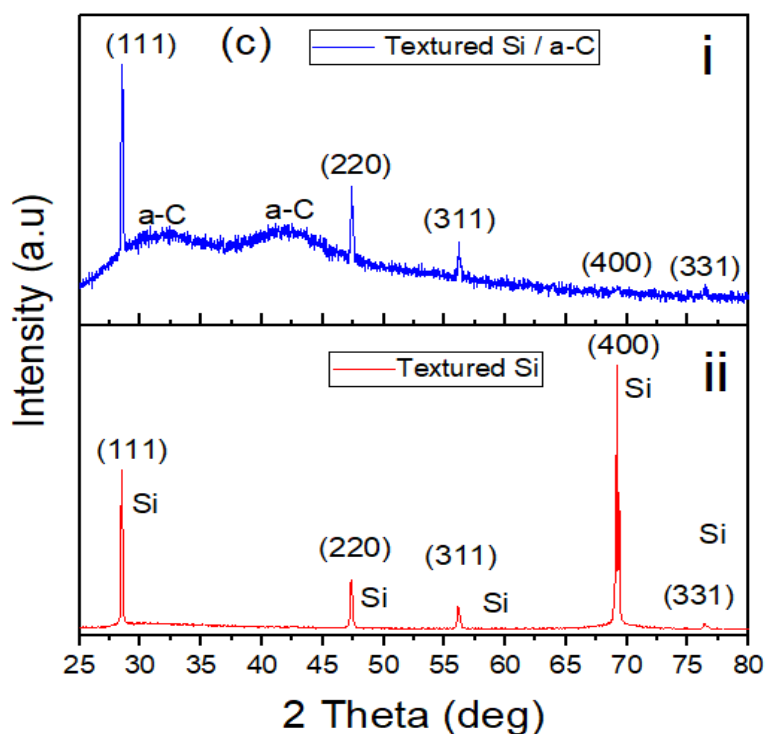
Figure 32 XRD patterns of (i) textured Si and (ii) Si/a-C nanocomposite coatings

5.2.3 Raman spectroscopy textured Si and amorphous carbon nanocomposite

The presence of a Si coating formed directly after the reduction reaction was further confirmed by results from Raman spectroscopy measurements presented in Figure 33. Besides verifying a single Si phase in the *in situ* formed coating, with first and second order peaks appearing at 520 and 965 cm^{-1}, the peak intensity of the textured silicon and c-Si substrate varied arbitrarily. What is more, a significant variation in the peak width between the two silicon types was recorded and estimated to be 6.9cm^{-1} for c-Si and 7.4 cm^{-1} for the textured Si. Discrepancies with Raman peak characteristics could be attributed to a number of factors [125]. Raman spectroscopy provides enough sensitivity to distinguish between crystalline and amorphous forms of materials, especially in silicon technology, where it is used as a quality control measure.

Variations in Raman peak positions generally inform the deviation from a single crystalline state. For silicon, an intense first order Raman peak position 520.5cm^{-1} is

93

typical of the c-Si, and divergences from this point are attributed to either a polycrystalline or amorphous state. Among the two silicon types, the amorphous form shows a greater deviation from the reference c-Si peak position. Amorphous silicon features a broad Raman peak around 480cm^{-1}, thus a clear indication that the textured silicon has a somewhat long-range order, representing a crystalline state. The crystalline nature of the silicon coating is equally confirmed from XRD results, presented in Figure 32(ii). Interestingly, the XRD results provide more information about the crystallinity type, suggesting a polycrystalline state. The remarkable disparity between the peak width of the silicon coating and c-Si is further proof of the polycrystalline nature of the textured silicon due to the presence of grain boundaries as defects. The presence of such defects will shorten the photon lifetime and eventually broaden the peak width.

Raman spectra of the coated silicon nanoflakes, confirmed the presence of a carbon coating formed after the carbonization of PAN, featuring peaks at 1347 and 1583cm^{-1}, which correspond to the D ("disorder") and G ("graphite") of highly amorphous graphite carbon [126].
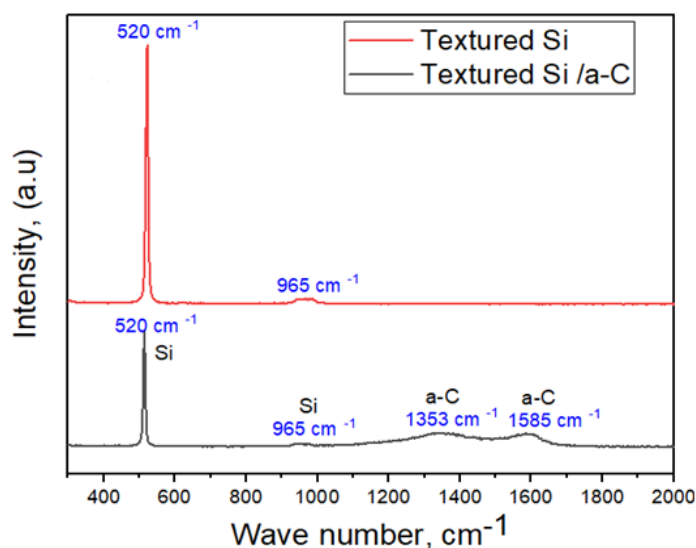
Figure 33 Raman spectra of textured Si and Si/a-C nanocomposite

An additional feature around 2700cm^{-1} corresponding to the 2D peak was observed at wavenumbers beyond 1000cm^{-1}. Carbon, in particular, has been hugely studied with

Raman spectroscopy, as it has the potential to distinguish between the various carbon types. As a way to understand the crystalline or disordered character of the carbon type, a dimensionless parameter, *R*-value, which is the ratio of the peak intensity of the D-band (I_d) to the G-band (I_g). From previous accounts, a high *R*-value symbolizes a high disorder, thus a lower crystallinity. The calculated I_d/I_g ratio of the various carbon films are presented in Table 2, and suggest somewhat amorphous continuous and porous carbon films formed after carbonization of PAN. The R-value for the a-C films on the c-Si surface remained unchanged for the continuous and porous carbon films, unlike the films on the textured silicon surfaces. For the textured silicon surfaces, the *R*-value of the carbon film decreased slightly from the continuous to porous films as indicated in Table 2. Although the reasons for this minor decline remain unclear, the polycrystalline nature and the varying strain levels as a result of the extremely rugged surface of the underlying textured silicon could account for this.

5.2.4 Microstructural Studies of textured Si and amorphous carbon nanocomposite

In Figure 34, the microstructural images of the textured silicon surfaces from diatom-derived silica and silica nano-balls are shown. The fractal structures best described as an array of irregular hills and valleys are characteristic of the silicon nanoflakes detailed in the previous sections. The extent of similarity between the microstructures of the preliminary and the optimized silicon coatings confirm the repetitive nature of this protocol in directly forming nanostructured Si coatings on wafer surfaces. Additionally, similar morphology was obtained even with a different silica precursor. All these results affirm the reproducibility of this technique. Aside from the similar rugged surface, the reaction terminated with the creation of micro-pores and cavities within the textured silicon films presented in Figure 35, again comparable to the early results.
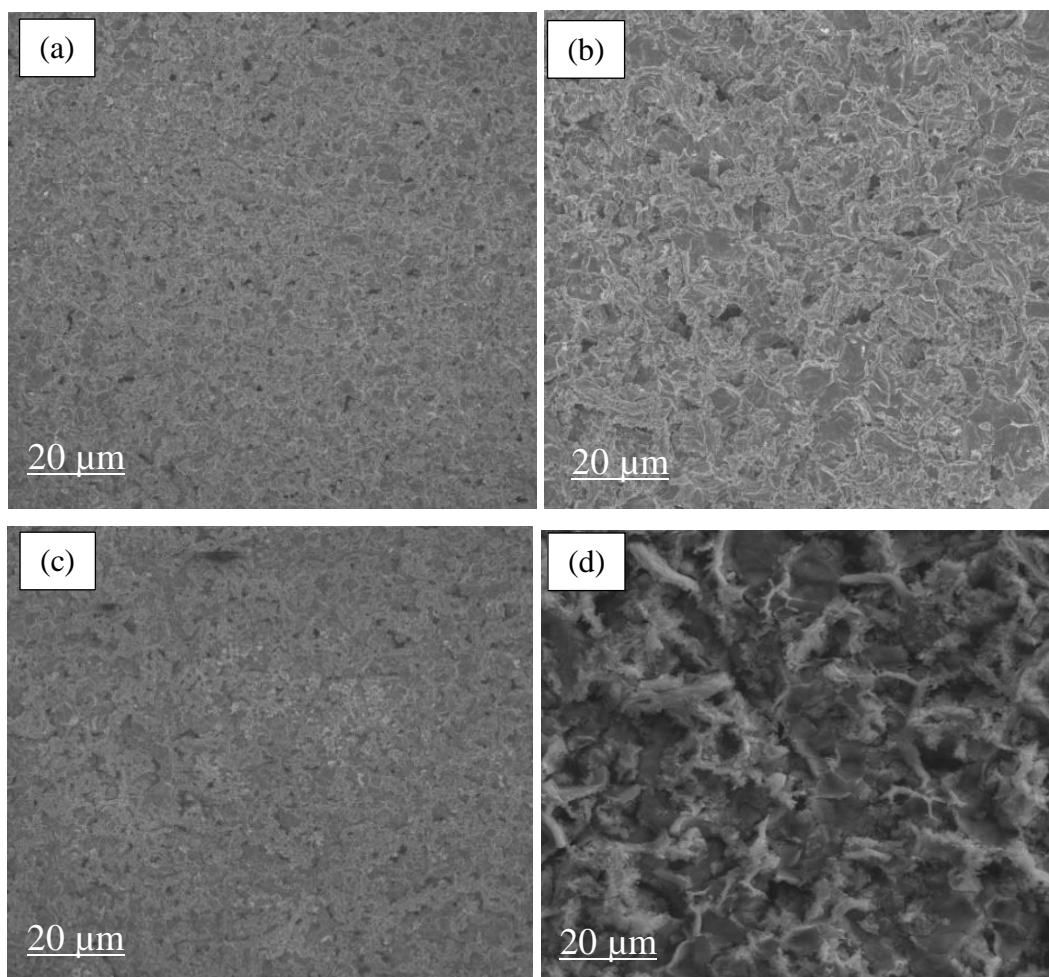
Figure 34 SEM images of textured Si (silicon nanoflakes) synthesized from (a and b) silica nanoballs (c and d) diatom-derived silica

From Figure 34cd, there is no evidence of the nanopores retained from the precursor diatom-derived silica powder, likewise no nanospheres from the silica in Figure 34ab. The highly exothermic MRR coupled with the intermittent nature of the reaction could be too aggressive for the nanoscale morphology. Unlike the preliminary attempt, where NaCl was used to scavenge excess heat, the optimized work excluded the inorganic salt. This could account for the absence of nanoscale features described in the early study. A firm contact between both silicon types (substrate and textured film) was revealed as indicated in Figure 35(a-d).

96
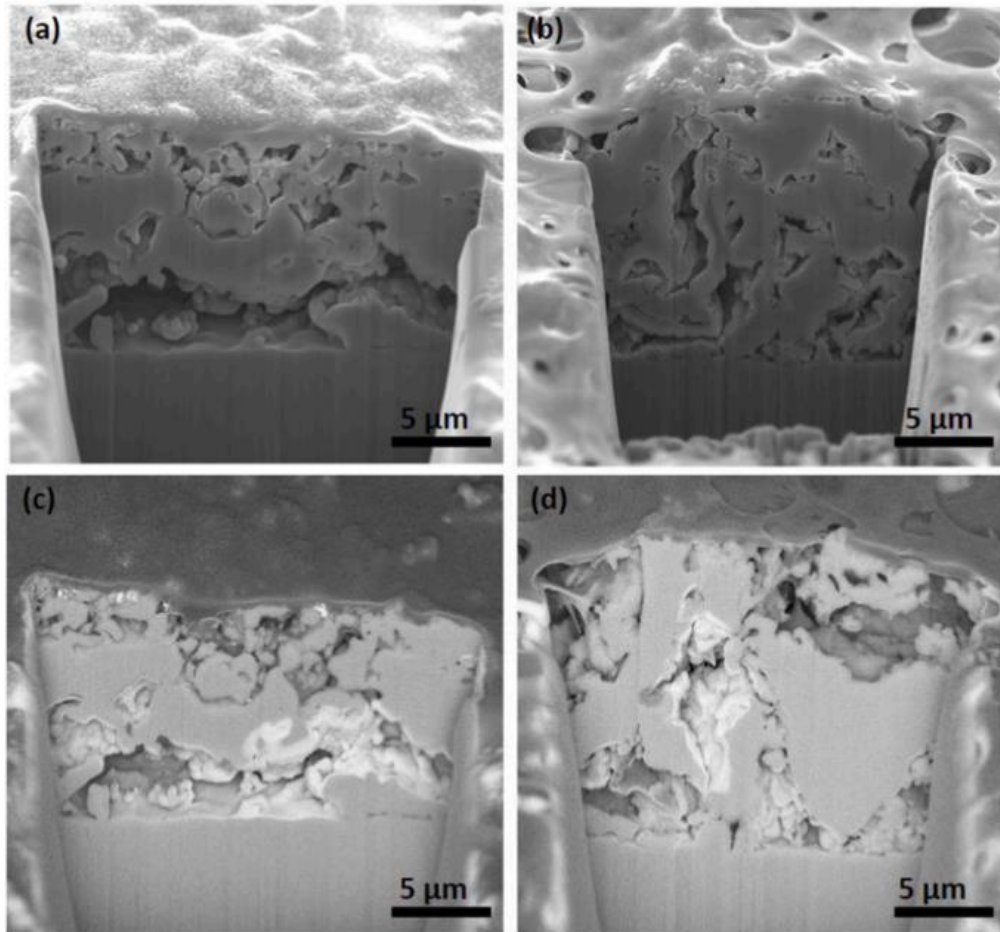
Figure 35 Microstructural images (a) and (c) Secondary and backscattered FIB-SEM images of Textured Si/a-C nanocomposite (continuous carbon film), (b) and (d) Secondary and backscattered FIB-SEM image of Si/a-C(1:1) nanocomposite (porous carbon film).

The early results showed similar firm bond between the *in situ* formed silicon nanoflakes and the silicon substrate surface via FIB-SEM studies. In a bid to complement the optical properties of the textured silicon surface, amorphous carbon thin film was created on the surface of the former. The carbon layer was prepared in two forms; as a continuous and as a porous film to understand the effect of structure on the optical properties. Carbon thin film with micro-to-nanoporous morphology was synthesized via the widely known phase separation technique. This was achieved through the phase separation between TEOS and PAN in their respective solvents. By means of

pipetting, a solution of (PAN and TEOS in their respective solvent) was dropped on the textured and bulk surfaces and dried on a hot plate to evaporate the solvent. The dried PAN film was rinsed in 5% HF to remove the silica micro- and nanospheres. This eventually led to a porous PAN film on the Si surfaces. Finally, an amorphous carbon film was formed following a carbonization process at 850∘C for 3 h. It is worthy to note that, the etching and carbonization stages are critical in determining the final structure of the carbon film. It was observed that when carbonization preceded the HF acid etching, the film remained continuous, with silica spheres firmly attached to the carbon matrix as shown in Figure 36a,d. The reverse however, delivered neatly formed porous carbon films shown in Figure 36b,c,e,f. We conclude that the preferred approach to produce a porous carbon coating is by etching the dried film, followed by the carbonization process. This notable structural difference could be attributed to the degree of attachment of the silica spheres to both PAN and a-C. Just after the phase separation process, triggered by the solvent drying step, silica spheres are loosely dispersed in the PAN matrix. Hence there is little resistance to removing them via HF acid washing, which eventually leads to a porous PAN film as a suitable precursor for a porous carbon film. Oppositely, when the carbonization process is executed prior to the acid etching step, there is strong resistance and very little access to the silica spheres firmly dispersed in the carbon matrix

The estimated average pore size for the porous carbon surfaces, a-C(1:1) and a-C(3:1), are 2.02μm and 2.17μm respectively. The pores were formed following the acid washing of the silica micro- to nanospheres formed during the phase separation between PAN and TEOS, unlike the continuous a-C film. As expected, the size of the pores decreased, following an increase in the mixing ratio of the PAN solution to the TEOS solution, irrespective of the substrate.
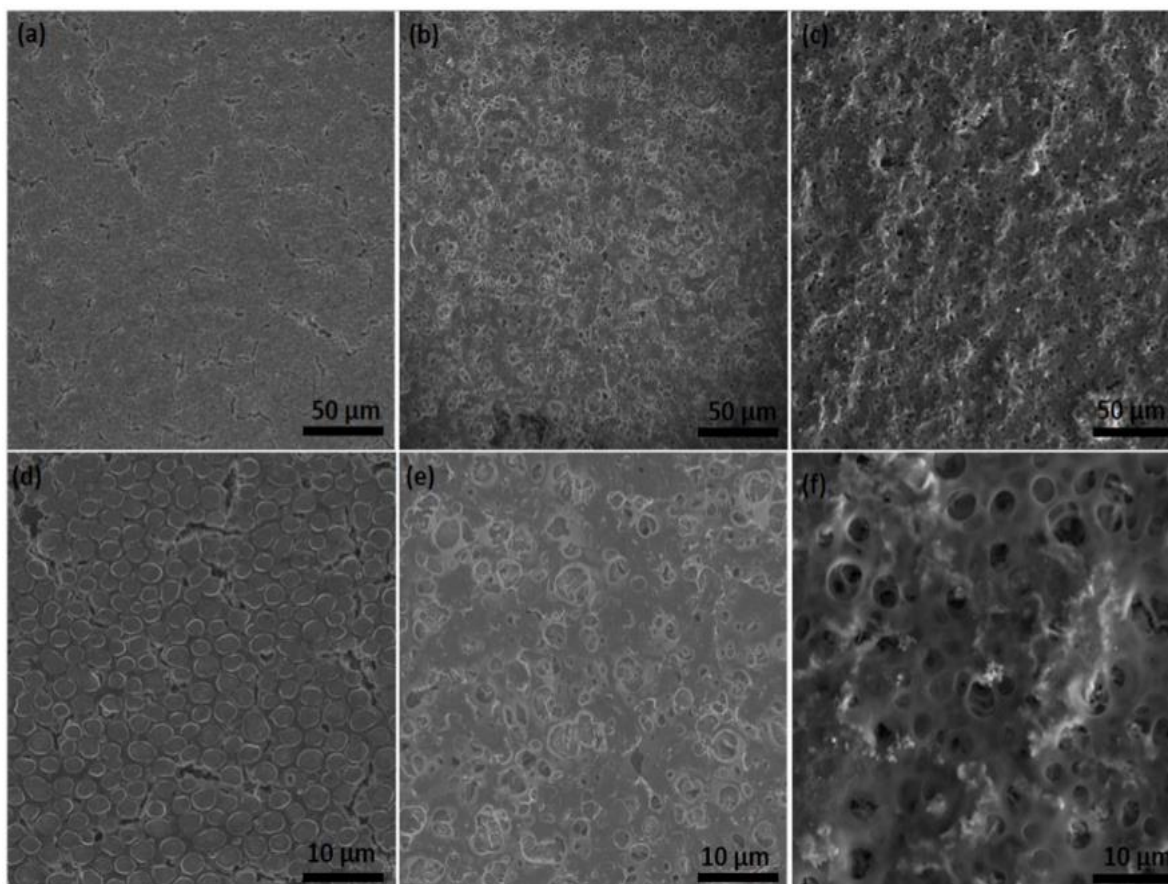
Figure 36 SEM images of possible Si/a-C nanocomposite coatings obtained via different etching and carbonization regimes (a and d) when etching proceeded carbonization (bcef) when carbonization proceeded etching

The average pore size was estimated using the program ImageJ by introducing a brightness threshold and performing basic particle analysis. The pores are treated as pseudo-ellipses, with the area and the major axis length provided in Figure 37. The histograms show distribution of the size parameters of pores observed in samples Si/a-C(1:1) and Si/a-C(3:1). The change of relative concentrations of a-C(1:1) to a-C(3:1) seems to only have a very small effect on the size of the deeper pores. However, it can be seen that [1:1] shows presence of larger shallower pores. It must be mentioned that this technique is strictly applicable to pores on the surface, and as such pores in the depth of

the a-C film cannot be accounted for. The thickness of the a-C film was estimated to be 0.6µm and the backscattered SEM images provided further contrast between textured Si and the former.
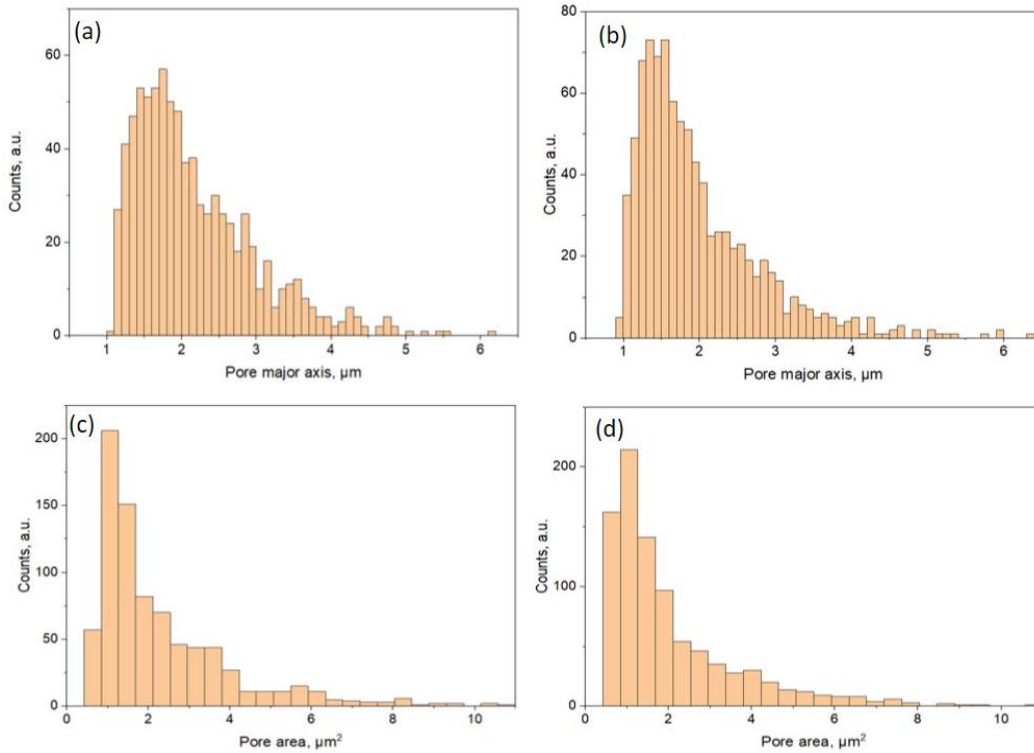
Figure 37 Pore size distribution of porous carbon films on textured Si (a) and (c) pore size and area of Si/a-C(1:1), and (b) and (d) pore size and area of Si/a-C(3:1)

5.2.5 Optical Properties of textured Si and amorphous carbon nanocomposite

Investigation of the absorption, reflectance and transmission responses of the samples was performed using an integrating sphere. All studied samples originated as standard pieces of a p-doped silicon wafer polished only on one side. Then some samples were covered with textured recovered from silica nanospheres (Si@SB), and some with nanostructured silicon recovered from diatomaceous earth (Si@DE). Both standard wafers and nanostructured surfaces were also investigated after the deposition of a thin film of amorphous carbon with different surface morphologies provided in Table 2.

Standard wafers exhibit some level of absorption in the visible range and then a sharp drop of absorption around 1100nm, which is due to photons having energies below silicon bandgap and therefore not being absorbed. The absorption in the IR range is not, however, zero, which is due to the silicon being p-doped, which allows some photons with energies below bandgap to still be absorbed.

It can be observed that across the whole spectral range a layer of nanostructures on the surface causes an increase in absorption. This is a result of the rougher surface causing significant scattering. Scattering causes some light to propagate at angles different from the normal to the surface and encounter a thicker mass of silicon. This also can lead to total internal reflection (TIR), which again results in the light being absorbed rather than transmitted or reflected away from the surface. With an a-C film deposited, the absorption of the resulting sample increases, and in the IR range it may drastically increase as the a-C film does not exhibit the same IR transparency as silicon. The rough nanostructured surface exhibits a synergetic interaction with the deposition of an a-C film, because the scattered light is absorbed in the a-C film more easily.

All the surfaces investigated showed distinct light response to the entire spectral range measured in this study. In Figure 38a, the absorption spectra of the three main surfaces, namely: c-Si, Si@DE and Si@SB, together with their modifications, are presented. The result presented in Figure 38a shows an improvement of visible light absorption for the polished silicon wafer surface after the surface texturing step via an *in situ* silica reduction process. The textured Si surfaces from both silica precursors (DE and SB) exhibited similar light absorption, a significant improvement over the c-Si surface. Such improvements in light absorption of silicon wafers have been previously reported [127-130] and are mostly associated with nanostructured surfaces, particularly BSi. The drastic increase in light absorption and a simultaneous decrease in the surface reflectance of nanostructured silicon wafer surface has been hugely attributed to an increase in the total internal reflection facilitated by nanostructures in the form of an array of multiple peaks and valleys. Unlike the typical BSi, which has regular peaks and valleys, the textured silicon from both silica precursors showed somewhat irregular structure.
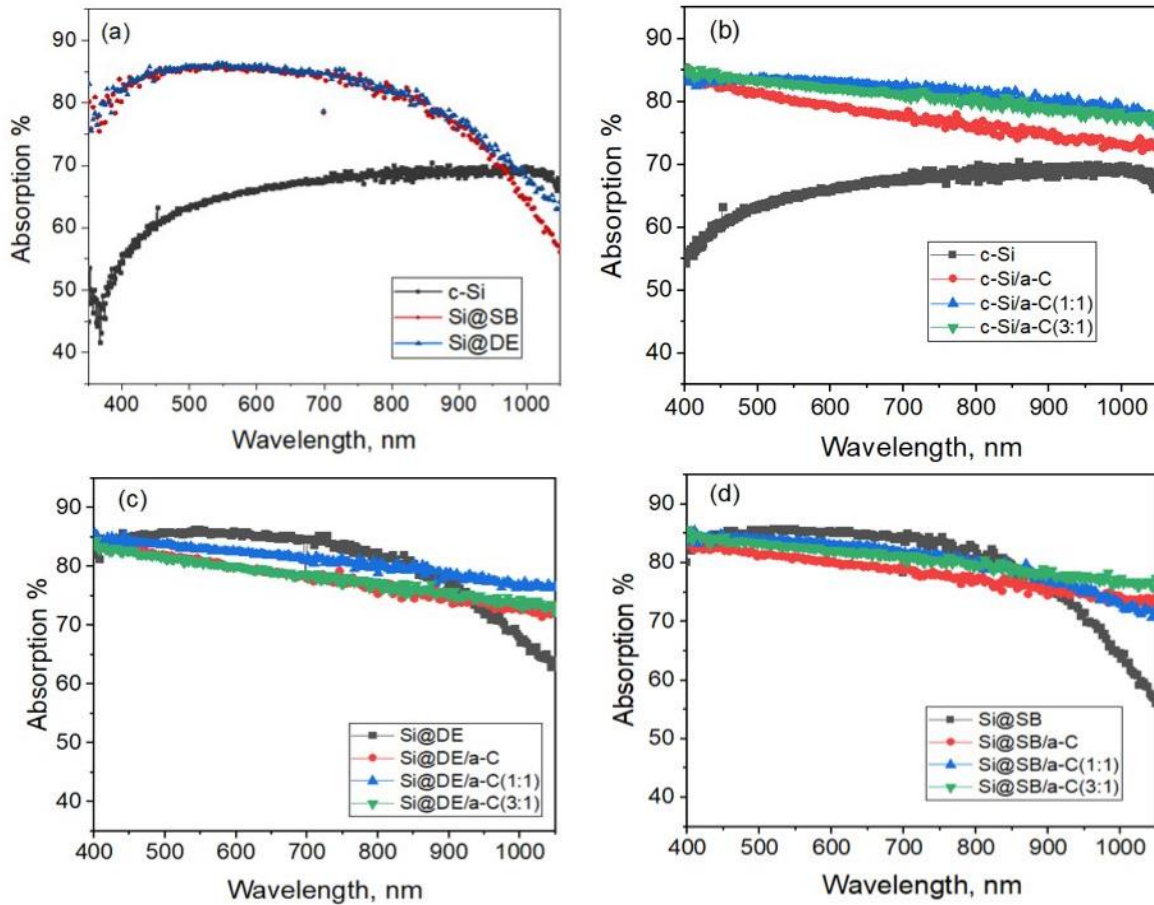
Figure 38 Absorption spectra in the visible and near IR range (400-1050nm) (a) Textured Si and c-Si surfaces, (b) c-Si and different a-C modifications, (c) Textured Si from DE and different a-C modifications and (d) Textured Si from silica nanoballs and different a-C modifications

The simultaneous increase in absorption and decrease in surface reflectance can be attributed to this irregular patterned surface, and is identical to the early results. Noticeably, the improved absorption dropped at near IR wavelengths (800-1000 nm) for both textured surfaces, necessitating further functionalization. In view of this setback, additional modifications were made on both textured silicon and the c-Si wafer surfaces, with the later serving as a reference sample. These modifications, in 3 forms, are presented in Table 2, together with their notations and *R*-value of the a-C coating. Interestingly, after modifying the textured silicon and c-Si surfaces, several improvements were recorded. Firstly, the rather sharp decline in light absorption for the

textured Si surfaces at near IR wavelengths changed to a steady decline, thus delivering light absorption between 70-80% at wavelengths (800-1000nm) as presented in Figure 38c and d. For the a-C modified c-Si surfaces, a remarkable increase in light absorption (75-85%) in the visible range was measured. Also, a steady decline in light absorption in the IR-region was observed for the a-C modified c-Si surfaces. Most importantly, noticeable differences in absorption were observed for the different carbon structures on the both c-Si and textured Si surfaces, namely *a-C*, *a-C(1:1)* and *a-C(3:1)*. The porous a-C coated surfaces (*a-C(1:1)* and *a-C(3:1)*) showed slightly better absorption than the continuous coating in the visible range, and this difference was quite profound for the c-Si sample as presented in Figure 38(b-d). Regardless of the structure type, further surface modification with a-C showed better light absorption in the IR region for all the samples.

In Figure 39, the absorption spectra of all the samples at longer wavelengths are provided. As mentioned before, the incredibly high surface absorption of textured silicon wafer surfaces such as BSi is limited only to the visible and near-IR wavelengths [126]. In this work, the same performance was observed for the textured silicon surfaces synthesized from either precursor. The textured polycrystalline Si coating showed a drastic decline in light absorption in the IR region. Likewise, the bare c-Si surface showed very low absorption in the IR region (1200-1700nm). The textured Si surface produced from silica nanospheres (Si@SB) showed a higher absorption than the counterpart diatomaceous earth (Si@DE) in the IR region (1200-1700nm) as shown in Figure 39b and c. This could be attributed to the slightly different surface profile of the textured silicon coating due to the different precursors. Different surface profiles of the textured silicon coating will lead to distinct scattering ability. It is worth pointing out that the performance of the a-C modifications at longer wavelengths was dependent on the surface profile of the substrates. For the a-C modified c-Si surfaces, a steep decline in IR absorption was observed as shown in Figure 39a. Surprisingly, for the a-C modified textured Si surfaces, a steadier decline in IR absorption was observed as presented in Figure 39b and c. This intriguing difference in IR absorption for a-C coating on different

surface profiles (c-Si and textured Si) suggest a synergy between surface texturization and anti-reflective coatings.
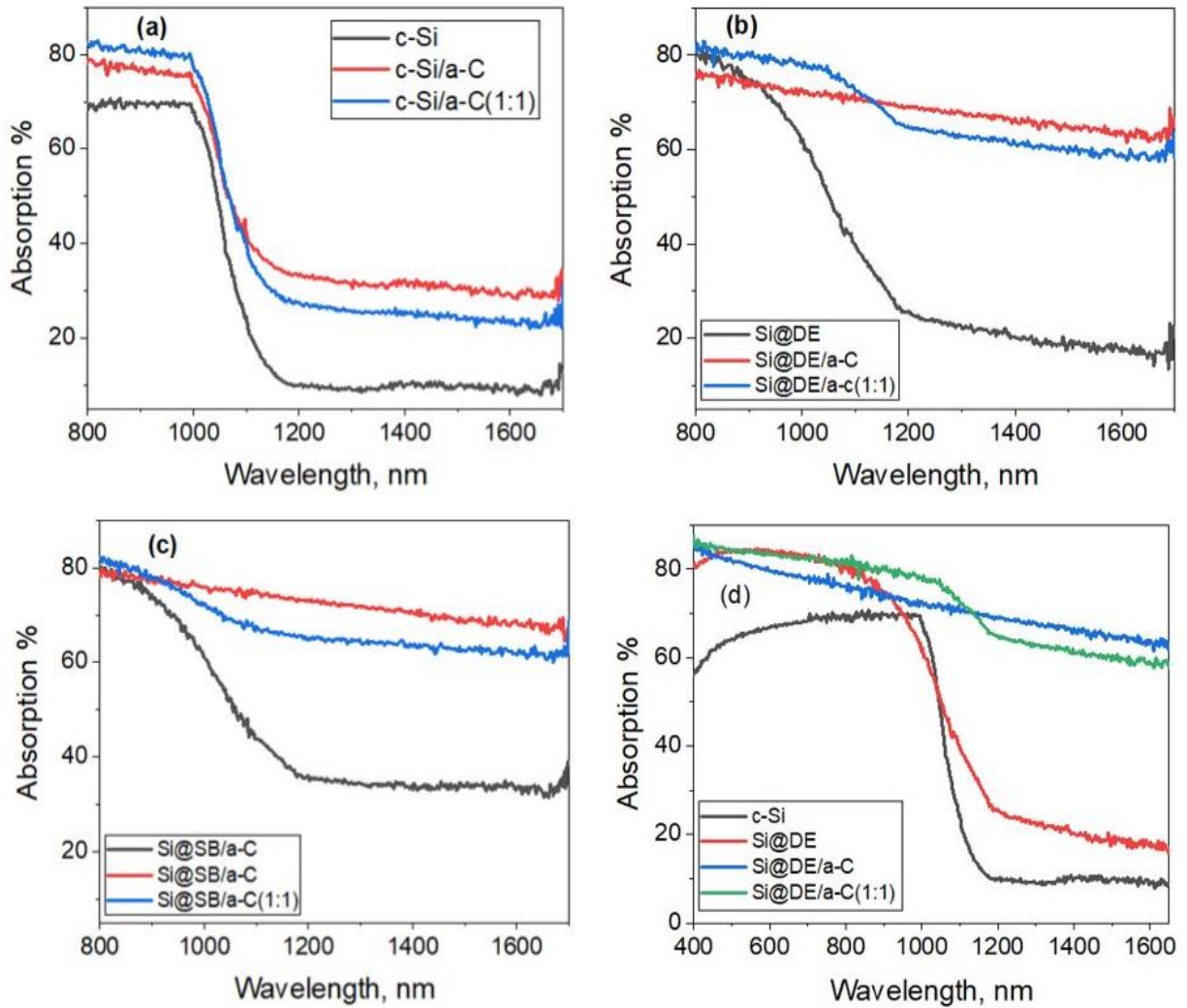
Figure 39 Absorption spectra at higher wavelengths (near IR and IR) (a) c-Si and different a-C modifications, (b) Textured Si from DE and different a-C modifications, (c) Textured Si from silica nanoballs and different a-C modifications, and (d) absorption spectra of different surfaces at each stage of fabrication

In order to achieve reasonable absorption at long wavelengths, a combination of nanostructured surfaces and anti-reflective coating seem to be the most practicable solution. Modifying the surface of c-Si wafer with a-C can provide increased absorption

in the visible range, but very low absorption at long wavelengths suggests this may not be an ideal path to achieve reasonable broadband absorption. In a recent study by Shah et al [126], a similar approach was used to improve the surface reflectivity of BSi over wide spectral range. Likewise, the textured Si surface in this work, their BSi samples showed high surface reflectance in near IR and IR wavelengths. As a result, a carbon-based anti-reflective coating, specifically pyrolytic carbon (PyC) film was deposited on BSi. The BSi+PyC surface delivered low surface reflection (0.5 %) in the IR region (1000-2000 nm) unlike the BSi alone (around 80%) [126]. The simultaneous decrease in surface reflection and increase in absorption in the IR band was attributed to the synergy between the two layers; the BSi traps incident light due to its anti-reflective ability and consequently absorbed by the PyC film.

In the current study, the textured Si surfaces display similar characteristics as BSi, by trapping light, which is subsequently absorbed by the amorphous carbon film. This mechanism has been likened to the previous attempts made with strongly doped silicon [129]. Here [129], increased absorption of the trapped light by the substrate silicon is attributed to the excess number of free electrons as a result of the strong doping. This explains the poor absorption for the carbon-coated c-Si samples in the IR band. Little to no light is trapped for absorption due to the absence of a textured layer. The impeccable synergy between texturized Si surface and anti-reflection coating/films was previously reported by Silva et al [131]. In their work [131], they reported a remarkable increase in short circuit current density (higher than 40 %) via the combination of texturization and several anti-reflective coatings. Both textured silicon wafer surfaces investigated by Shah and Silva et al [126,131] were obtained via conventional routes, although structural difference are likely due to different synthesis conditions. In this work, the textured Si wafer surfaces were obtained via a non-conventional approach.

Regardless of the approach and the anti-reflective coating used, the effectiveness of a textured silicon/anti-reflective bi-layer coating proved irrefutable. While this presents a major path to tackle unwanted surface reflections and deliver high broadband absorption, the need to understand and exploit the role hierarchical structural

modifications on the optical properties of such bi-layers remains a top priority. Except for the type of carbon, synthesis process and thickness of both textured Si and anti-reflective coatings, there is little to no information about the effects of structural modifications of the carbon coating on the optical properties of silicon based solar cells and related optical systems. As earlier indicated, all the carbon films studied were continuous/non-porous.

5.2.6 Effects of Porosity on Optical Properties

The study of both continuous and porous amorphous carbon AR coatings has shown that structural modifications in the carbon-based film could lead to significant changes in the optical properties. The fact that the individual films perform at their best in different regions (visible and IR range) is further evidence of optical property dependence on surface morphology. The porous AR coatings showed better absorption in the visible range than the continuous films regardless of the substrate (bare Si or textured Si). In particular, the absorption spectra of the porous surfaces showed somewhat noticeable dependence on the pore size. The carbon film with bigger pore size showed slightly better light absorption in the visible and near IR range (400-1000nm). The possibility of tuning the pore size via the phase separation technique means an optimal porosity can be obtained for the best light absorption of this AR coating type. The synthesis of porous films is not a new design route as far as AR coatings are concerned, although this has not been fully explored for carbon-based materials. In a number of accounts [132-146], porous SiO_2, ZnO, Al_2O_3, MgF_2 and TiO_2 films were studied for their potential application as anti-reflective coatings. The introduction of nanopores has been regarded as an ideal way to improve the optical properties of AR coatings.

Generally speaking, nanopores are considered to offer a low refractive index AR coating compared to their bulk counterpart. In a recent report, Xia et al [135], investigated the optical properties of continuous and porous sol-gel acid catalyzed silica coatings on borosilicate glass (BK-7). Their study revealed a near total light transmission for BK-7 glass with a porous silica coating (99.64%), which represented a 5% extra transmittance compared to the continuous silica coating ($\approx$ 95%). Typical BK-7 glass has

a light transmittance of 91.8% in the visible spectral range. Interestingly, when the packing order of the silica particles increased, a corresponding decrease in the light transmission was observed, potentially due to the decrease in the porosity. A lot of studies devoted to porous SiO_2 coatings on glass have been recorded in the past few years [136-140] as efforts to improve the performance in optical, optoelectronic and solar applications lingers.

The relationship between nanoporous structures and optical properties is further evidenced in a study by Kumar et al [147], where the transmittance of both bulk and porous polyethylene terephthalate (PET) was investigated. As expected, the transmittance of the PET sample increased from 89% (bulk) to as high as 94% (porous on one side). Treating both sides of PET to obtain porous networks on either surface triggered an additional increase in transmittance ($\approx$ 99%). Another interesting result which substantiates the link between porous structures and optical properties is captured in a recent study by Gupta et al [146]. Here [146], they achieved an impressive light observation for zinc oxide nanowires (ZnO NW) via porosities. As far as practical applications are concerned, especially, in photodetectors, ZnO is considered a candidate material only in the UV-range, as a result of its wide band gap, limiting its applications in the visible range.

A lot of studies have succeeded in improving the optical properties of ZnO in the visible range, via doping and heterojunction structures [148-150] but the recent approach, through induced-porosities offers a much more simplistic and cost-effective path [146]. By inducing porosities in the already desired ZnO NW configuration, Gupta et al [146] successfully extended light absorption to the visible range of the EM spectrum. Furthermore, longer wavelength absorption was observed for ZnO NW with the highest porosities. Indeed, this breakthrough was majorly attributed the multiple light scattering sites presented by the pores and the roughened surfaces. Another logical reason for this is the difference in the refractive indices of the material and the pores (air, n=1), which eventually leads to a desirable effective refractive index for the porous ZnO NW. The effect of porosities on optical properties is further verified in a study by Suzuki et al

[151]. Here [151], they observed higher light absorption for copper and iron substrates with porous surfaces than the substrates with mirror-polished surfaces, which was attributed to multiple light reflection and absorption on the pore surface. Regardless of the material class, organic, inorganic or metallic, porosities improved the optical properties to a large extent. Despite the abundance of literature suggesting the introduction of porosities as a realistic path to improve optical properties, very little attempt has been made with carbon-based materials.

In an isolated study, Nikola et al [152] investigated the antireflective ability of a hierarchical single-walled carbon nanotube (SWCNT) coating with a void fraction of 48%. Their nanoporous SWCNT coating succeeded in reducing the high total reflectance of bulk silicon surface (27-70%) in the UV-VIS-NIR (ultraviolet-visible-near infrared) to 14-33%. As with other reports discussed, the low refractive index played a pivotal role in suppressing the surface reflectance coupled with the high absorption coefficient of the SWCNT. Apart from inducing porosities in existing AR coatings, naturally porous materials may offer low refractive index films for antireflection applications. Chen et al [143] investigated the anti-reflective ability of zeolite, as a direct replacement for porous amorphous silica, since the naturally mesoporous material offers better mechanical strength than the later. Their zeolite AR coating showed impressive anti-reflection properties coupled with a reasonable mechanical strength [143]. These accounts provide beyond any reasonable doubt, the effectiveness of porosities in the overall enhancement of optical properties. This same trend is shown in the current study, where the thin porous a-C coating drastically improved the absorption in the broadband range. The minute difference in absorption for the porous surfaces (3:1/1:1) in this work could be attributed to: the additional scattering and a smaller effective refractive index for the surface with slightly bigger pores.

5.2.7 Absorption at Longer Wavelengths

Another interesting observation in the present study is the significant difference in absorption recorded for the continuous and porous AR surfaces. At longer wavelengths (1200-1700nm), the continuous film showed better absorption than the porous surface

irrespective of the substrate. In the VIS range (400-800nm), absorption is highly dependent on the textured silicon layer and not the a-C film, as previously indicated in a work by Shah et al [126]. As such, the textured Si surfaces alone showed better absorption than with the different carbon surfaces. It is in the same region that the surface with bigger pores (*a C 1:1*) shows slightly higher absorption than surfaces with small pores (*a-C 3:1*) and continuous film (*a-C*).

As earlier mentioned, this may be due to increased multiple scattering and the smaller effective refractive index for the big pore surfaces. However, at IR wavelengths (1200-1700 nm), a higher absorption is recorded for nanocomposite bi-layer coating with the continuous carbon film. As far as absorption at longer wavelengths is concerned, both bulk silicon wafer surface and textured silicon showed poor performance. It has already been established that improved absorption in the carbon coated nanostructured Si surfaces is largely due to light interaction and subsequent absorption by the carbon film at the textured Si surface [126]. For this mechanism to be effective, a continuous carbon coating, free from pores and voids, is desirable. The presence of pores and/or voids in the carbon coating will lead to a direct interaction between incident light and the textured Si wafer, which is immediately transmitted and lost as schematically shown in Figure 40.

For this reason, as far as light absorption in the IR region as concerned, AR coating without porosities is desirable. In contrast, porous AR coatings appear to offer high absorption in the visible range and may be useful for applications restricted to this range. Designing a hybrid (porous and continuous) carbon thin film could significantly improve broad band absorption since both structures could complement the other. The facile route presented in this study is promising for the development of low-cost and non-toxic solar cells considering the eco-friendly and low –cost materials and synthesis processes involved. Also, such structures can be promising for multispectral photodetectors owing to their tunable broadband absorption ability. The distinct broadband absorption behavior of the textured Si surface and the porous and continuous bi-layer nanocomposite structures can utilized in optoelectronic devices for the detection of UV, visible and near-IR light signals. The facile and low cost approach to obtain these

structures presents a way to produce economical photosensors for multi-color light sensing, imaging, spectroscopy and optical communications [153].
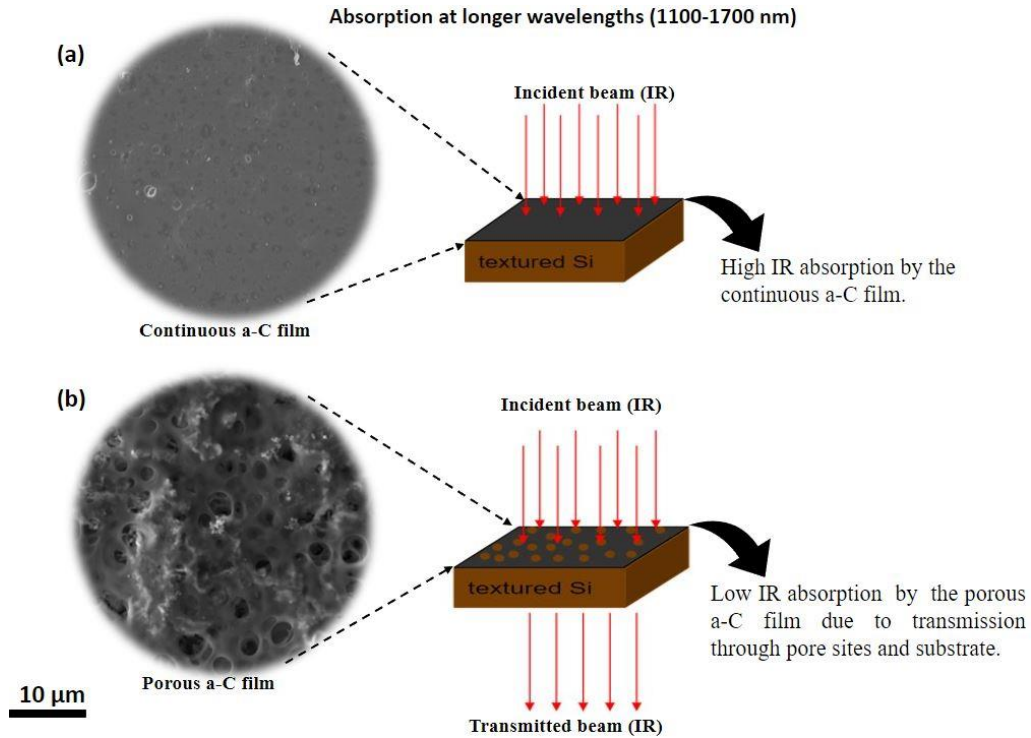
Figure 40 Longer wavelength absorption in different textured Si/a-C nanocomposites (a) effective absorption facilitated by the continuous amorphous carbon film, and (b) low IR absorption due to light transmission through pore sites (porous a-C)

5.2.8 Optical Energy Band Gap of Textured Si and Si/a-C Nanocomposite Surfaces

The optical band gap of the obtained multi-layered structures was estimated using the Tauc Plot method. For the purposes of this estimation, the multilayered structures were treated as a single structure, since meaningful separation of doped Si wafer contribution from the structure as a whole is not feasible. Origin 2021b software was used to build plots. Fitting the linear part of the Tauc curve gave adjusted R-Square fitting parameter above 0.999. The estimated optical band gaps for the doped silicon

wafers used, the same wafers covered with Si@DE and wafers covered with a composite Si@DE and a-C (1:1) were found to be 1.14, 1.2 and 1.17 eV accordingly as presented in Fig. 9. For the wafer covered with S@DE/a-C composite, there is no indication of an optical band gap present, which is consistent with the absorption not exhibiting any observable dips. The enhancement in optical energy band gap of S@DE could be a classic case of quantum confinement effect [154-157] or compressive strain driven by the textured Si coating capable of inducing direct-indirect band gap transition [158]
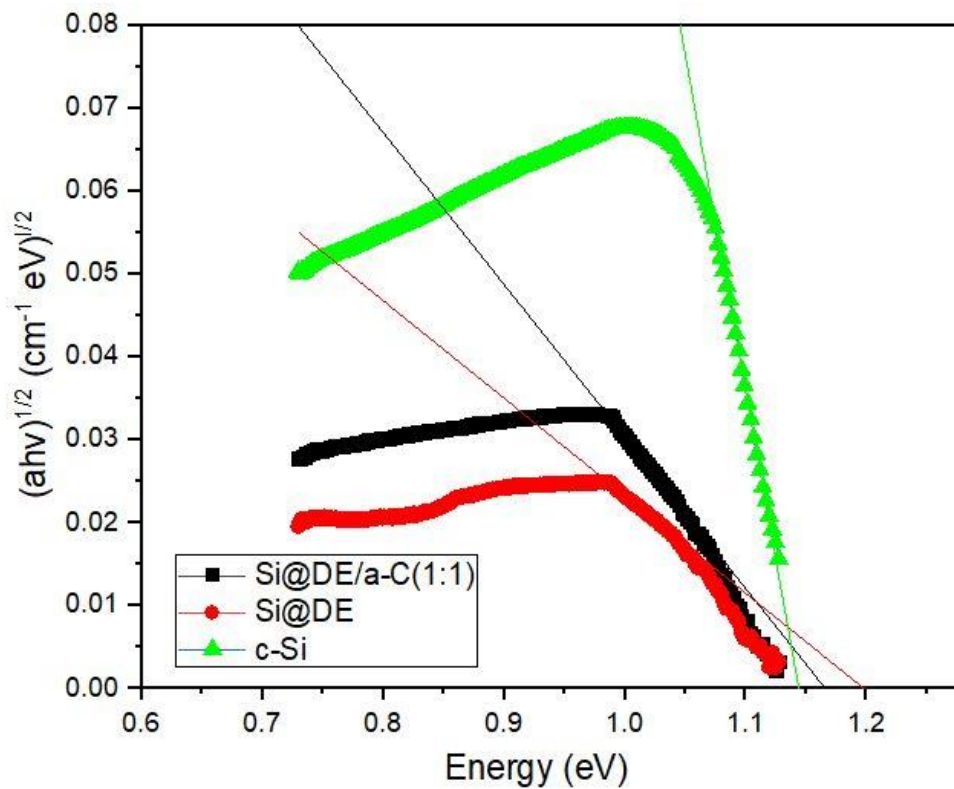
Figure 41 Optical energy band gap of c-Si, textured Si (Si@DE) and textured Si@DE/a-c(1:1) bi-layer nanocomposite.

Chapter 6. Outlook

In materials science, thermal pre-treatments are widely known for their applications in metal and alloy development, building and supporting materials for thermal energy storage, filter aids and absorbents. The full-scale implementation of pre-heat treatments benefits from the in-depth understanding of such processes through many years of scientific research. The preliminary results captured in this study complements already existing facts about thermal pre-treatments and bring to light very key aspects of the effects of such procedures on chemical and physical properties of materials. The possibility of controlling and inducing noticeable modifications in the powder characteristics of diatom-derived silica and recovered silicon via thermally induced phase transformations in the Si-O system is promising for the synthesis of nanostructured silicon-based materials.

An indirect beneficiary of the results from the present study is the filtration industry where diatom-derived silica is used as filter aids. Generally diatom-derived silica is roasted to unclog pores and remove impurities before use but this often leads to significant color changes in the powder. To prevent coloration of the filtrates as a result of the colored diatom-derived silica filter aids, fluxes are normally used during roasting. As earlier presented, coloration could be effectively reduced by controlling the heating environment without compromise to pore cleansing and impurity removal. The amount of fluxes used in the pre-treatment of diatom-derived silica aids could be reduced drastically when effectively combined with calcination to reduce cost of operation.

With the growing attention given to diatom-derived silica and other silica types as negative electrode for Li-ion batteries, understanding the electrochemical behavior of amorphous and crystalline forms is important for optimizing anodes based on these materials. The present results show a clear dependence between the structure and powder characteristics of silica and electrochemical performance. Further experimental work is required in future studies to elucidate the lithiation process in the crystalline and amorphous forms of silica. As a convertible oxide, lithiation in silica leads to reversible and irreversible reactions that produce silicon, lithium oxide and silicates. The

composition of these compounds influences the electrochemical performance such as specific gravity and stability. As such an in-depth study these reaction pathways and phases formed in different silica forms will provide better understanding of the lithiation mechanism and subsequently lead to optimal performance. Finally, further electrochemical studies of pristine and heat treated diatom-derived silica anodes should proceed with post-lithiation studies using state of the art characterization techniques to understand the underlying differences in the morphology, chemical and physical changes between the two silica forms after cycling against lithium.

Another critical aspect of the new results shows the dependence between morphology preservation during the chemical reduction of siliceous materials to silicon and the structure and powder properties of precursor silica used. The in-situ thermal analysis of the MRR of crystalline and amorphous silica powders revealed significantly different on-set and peak exothermic temperatures which suggest quite dissimilar reaction kinetics for both silica forms. The different on-set temperatures could be exploited to synthesize nanostructured silicon powders at temperatures unique to particular silica types. In future studies, the pristine and heat treated diatom-derived silica powders will be reduced at the peak exothermic temperatures measured during the *in situ* thermal studies of their respective MRR to silicon. After the silica reduction, the powder properties and morphology of the recovered silicon powders will be analyzed and subsequently studied as a negative electrode for Li-ion batteries.

The porous Si consolidate synthesized via the *in situ* MRR of diatom-derived silica on silicon substrates presents a facile and cost-effective approach to texture silicon wafer surfaces to reduce optical losses and equally provide a platform for active materials for functional applications. Another potential application of the textured Si surface is as an anode for Li-ion batteries due to their micro- to- nano-structures. Other silicon consolidates in the form of nano-pillars and micro-towers have been previously studied as anode materials for Li-ion batteries [159,160] and showed better electrochemical performance than their bulk counterparts. It will be interesting to examine the electrochemical performance of textured Si and Si/a-C nanocomposite bi-layer as they

offer relatively cost-effective, facile and eco-friendly way to obtain nanostructured Si anodes for battery applications.

The straightforward synthesis of silicon powder and *in situ* creation of nanostructured silicon coating clearly offers a low-cost approach compared to conventional methods of producing Si nanostructures as such as pyrolization of silane, metal-assisted chemical etching, laser treatments, chemical vapor deposition, cryo-mediated exfoliation of metallurgical silicon to Si nano-sheets [161-163]. However, the initial cost comparison of the approach outlined here and currently existing techniques is quite challenging taking into account the scarcity of information and variation in the prices of energy supply and raw materials used in these processes. That notwithstanding, the appreciation of the cost difference could originate from the expensive set and time required to produce large quantities. In practical terms, the approach presented here requires an argon-filled furnace for both heat treatments and MRR processes. Depending on the size of the heating chamber, large scale amounts of silicon powder and textured can be produced. Moreover the direct MRR of diatom-derived silica relies of chemical solvent such as HCl and HF for purification purposes. The creation of porous anti-reflective amorphous carbon coating via the phase separation technique also requires less expensive chemical and laboratory set-up.

Chapter 7. Conclusions

The present study has unraveled fascinating effects in the Si-O system which could advance the development of efficient chemical reductions methods for the production of desired silicon-based materials. Silicon powders with nano-scale morphology were successfully synthesized from pristine and heat treated diatom-derived silica precursors via the magnesiothermic reduction reaction. Preliminary results show that thermally induced transformations have significant effects on the powder characteristics of pristine diatom-derived silica and the resulting changes are observed in the recovered silicon product as well. These changes were also found to be dependent on the heating environment. In all, calcination or roasting of diatomite did not destroy the porous structure entirely. Roasting resulted in powders with increased average particle size. A slight decrease in particle size for the calcined powder was observed. Not only does the heating environment affect the particle size and the structure of the product silicon, it also affects the crystallinity of the silicon formed and the crystallite size of the product silicon. The recovered silicon with the highest level of crystallinity was obtained from the roasted powder. However, the smallest silicon crystallite size, a desired requirement for lithium battery applications was obtained from the calcined powder. As such, the calcined diatom-derived silica based anode material showed the best electrochemical performance. Likewise the calcined diatom-derived silica precursor, anode materials prepared from the roasted diatom-derived silica powder show superior electrochemical cycling when compared with the anode from the pristine powder. The negative electrodes prepared from the crystalline powders showed discharge capacities of 340mAhg^{-1} (calcined) and 255mAhg^{-1} (roasted), while their pristine counterpart displayed discharge capacity of 168mAhg^{-1}. The recovered Si powder from the calcined diatom-derived silica showed superior electrochemical performance when tested a negative electrode. The nano-Si anode showed a discharge capacity an order of magnitude higher than bulk-Si anodes. As far as the kinetics of their individual magnesiothermic reduction reactions are concerned, the heat treated powders offered lower onset and exothermic

peak temperatures than the pristine powder. What is more, the calcined powder was reduced at a slightly lower temperature compared to the roasted counterpart. It is quite clear the extent of effects thermally-induced transformations play and these results could help provide guidelines for selecting the most ideal precursor diatom-derived silica for the synthesis of silicon based materials for energy related applications.

The metallothermic reduction of diatom-derived silica to silicon has been successfully extended to the creation of nanostructured silicon coatings. Silicon nanoflakes formed directly on the silicon wafer possessed very intricate details of the precursor diatomite powder to some extent. The as-produced silicon nanoflakes reduced surface reflection of silicon wafer surface and simultaneously increased absorption significantly. The reflectivity of the silicon nanoflakes are comparable to the range of surface reflection reported for BSi. Although metal contamination from Mg in the form of Mg_2Si, are possible, a follow-up self-etching of this unwanted product could also occur through the solid state reduction of SiO_2. This can increase the silicon yield and self-control the thermite reaction. The high purity Si nanoflakes formed via the *in situ* MRR of diatomite was confirmed by results from EDS and Raman spectroscopy. A preliminary adhesion scratch test also confirmed a good bonding of the silicon nanoflakes to the surface of the substrate silicon wafer. The initial difficulties of controlling the thickness and the non-uniformity of the nanostructured silicon formed were successfully addressed through kinetics study.

The development of such low cost and facile textured surfaces is crucial for optimizing the light-matter interaction of optical devices and the results captured in this work adds up to the existing progress made so far in this area. Just like BSi, light absorption due to increased total internal reflection on the textured surface was only limited to a narrow range (visible light) and required further functionalization with a carbon-based film to obtain textured Si/a-C nanocomposite AR coatings. Porous and continuous a-C carbon thin films were successfully synthesized on the textured Si surface via the phase separation between TEOS and PAN solutions. The bi-layer textured

Si/amorphous carbon nanocomposite was confirmed in XRD, SEM and Raman spectroscopy measurements. The outcomes are listed as following:

    i. The porous and continuous a-C modified surface showed a steadier absorption than c-Si and textured Si surfaces.

    ii. All the Si/a-C nanocomposites (c-Si and textured Si) with porous surfaces showed higher absorption than the continuous surface in the visible and near-IR range (400-1100nm) due to additional scattering sites and a small effective refractive index resulting from the pores.

    iii. At longer wavelengths (1200-1700nm), light absorption in the Si/a-C nanocomposites was dependent on the surface topography of the substrate (c-Si and textured Si). A steep decline in absorption was observed for all the a-C modified c-Si surfaces. For all the textured Si/a-C samples, just a narrow drop in absorption. This was attributed to the synergistic connection between the carbon film and the textured Si surface, where incident light is scattered by the highly irregular surface of textured Si and subsequently absorbed by the carbon film.

    iv. The porous nanocomposite surfaces exhibited lower absorption than the continuous ones at longer wavelengths (1200-1700nm), irrespective of the substrate (c-Si and textured Si). For the synergistic link between the carbon film and the silicon substrate to be effective, a continuous film is required. This prevents direct contact between the silicon substrate and the incident light which could be lost through transmission. Apart from preventing direct interaction of IR radiation with the Si substrate, the continuous carbon film is also needed to absorb light that scattered by the substrate at the Si and carbon interface.

    v. Even though carbon-based films show promising anti-reflective abilities, applying such coating directly on c-Si does not guarantee wide-band absorption. Textured Si surface is more suited for carbon-based AR coatings and potentially other ones. Also, depending on the application, either porous or continuous AR carbon coating shows superiority in different regions of the EM spectrum.

This approach and materials used offer an alternative route to the nanostructuring of silicon wafer surfaces for functional applications.

Bibliography

[1] K. C. Condie in K. H. Wedepohl (ed.): Handbook of Geochemistry, vol. II-2, Springer, Berlin 1970, Section 14

[2]Flörke, O. W., Graetsch, H. A., Brunk, F., Benda, L., Paschen, S., Bergna, H. E., ... & Schiffmann, D. (2000). Silica. *Ullmann's Encyclopedia of Industrial Chemistry*.

[3] Kosterev, A. A., Tittel, F. K., Serebryakov, D. V., Malinovsky, A. L., & Morozov, I. V. (2005). Applications of quartz tuning forks in spectroscopic gas sensing. *review of scientific instruments*, *76*(4), 043105.

[4] Ferreira, G. N., Da-Silva, A. C., & Tomé, B. (2009). Acoustic wave biosensors: physical models and biological applications of quartz crystal microbalance. *Trends in biotechnology*, *27*(12), 689-697.

[5] Davila, L. P., Risbud, S. H., & Shackelford, J. F. (2008). Quartz and silicas. In *Ceramic and glass materials* (pp. 71-86). Springer, Boston, MA.

[6] Blau, P. J. (2001). *Compositions, functions, and testing of friction brake materials and their additives* (No. ORNL/TM-2001/64). Oak Ridge National Lab.(ORNL), Oak Ridge, TN (United States).

[7] Holleman, A. F., Wiberg, E., & Wiberg, N. (2001). *Inorganic chemistry*. Academic press.

[8]Wenham, S. R., & Green, M. A. (1996). Silicon solar cells. *Progress in Photovoltaics: Research and Applications*, *4*(1), 3-33.

[9] Heywang, W., & Zaininger, K. H. (2004). Silicon: the semiconductor material. In *Silicon* (pp. 25-42). Springer, Berlin, Heidelberg.

[10] Ohara, S., Suzuki, J., Sekine, K., & Takamura, T. (2004). A thin film silicon anode for Li-ion batteries having a very large specific capacity and long cycle life. *Journal of power sources*, *136*(2), 303-306.

[11] Koynov, S., Brandt, M. S., & Stutzmann, M. (2006). Black nonreflecting silicon surfaces for solar cells. *Applied physics letters*, *88*(20), 203107.

[12] Hochbaum, A. I., Chen, R., Delgado, R. D., Liang, W., Garnett, E. C., Najarian, M., ... & Yang, P. (2008). Enhanced thermoelectric performance of rough silicon nanowires. *Nature*, *451*(7175), 163-167.

[13] Jung, S. C., Choi, J. W., & Han, Y. K. (2012). Anisotropic volume expansion of crystalline silicon during electrochemical lithium insertion: an atomic level rationale. *Nano letters*, *12*(10), 5342-5347.

[14] Boukamp, B. A., Lesh, G. C., & Huggins, R. A. (1981). All-solid lithium electrodes with mixed-conductor matrix. *Journal of the Electrochemical Society*, *128*(4), 725.

[15] Schierning, G. (2014). Silicon nanostructures for thermoelectric devices: A review of the current state of the art. *physica status solidi (a)*, *211*(6), 1235-1249.

[16] Boukai, A. I., Bunimovich, Y., Tahir-Kheli, J., Yu, J. K., Goddard Iii, W. A., & Heath, J. R. (2008). Silicon nanowires as efficient thermoelectric materials. *nature*, *451*(7175), 168-171.

[17] Zong, P. A., Makino, D., Pan, W., Yin, S., Sun, C., Zhang, P., ... & Koumoto, K. (2018). Converting natural diatomite into nanoporous silicon for eco-friendly thermoelectric energy conversion. *Materials & Design*, *154*, 246-253.

[18] Y. Nishimoto and K. Namba, Investigation of texturization for crystalline silicon solar cells with sodium carbonate solutions, *Sol. Energy Mater. Sol. Cells*, 2000 Apr 1, **61**(4), 393–402

[19] J. Yoo, Reactive ion etching (RIE) technique for application in crystalline silicon solar cells, *Sol. Energy*, 2010 Apr 1, **84**(4), 730–734

[20] D. Z. Dimitrov and C. H. Du, Crystalline silicon solar cells with micro/nano texture, *Appl. Surf. Sci.*, 2013 Feb 1, **266**, 1–4

[21] X. Liu, P. R. Coxon, M. Peters, B. Hoex, J. M. Cole and D. J. Fray, Black silicon: fabrication methods, properties and solar energy applications, *Energy Environ. Sci.*, 2014, **7**(10), 3223–3263

[22] M. Otto, M. Algasinger, H. Branz, B. Gesemann, T. Gimpel, K. Füchsel, T. Käsebier, S. Kontermann, S. Koynov, X. Li and V. Naumann, Black silicon photovoltaics, *Adv. Opt. Mater.*, 2015 Feb, **3**(2), 147–164

[23] Lv, T. Zhang, P. Zhang, Y. Zhao and S. Li, Review application of nanostructured black silicon, *Nanoscale Res. Lett.*, 2018 Dec, **13**(1), 1–10

[24] Stratton, F. P., Chang, D. T., Kirby, D. J., Joyce, R. J., Hsu, T. Y., Kubena, R. L., & Yong, Y. K. (2004, August). A MEMS-based quartz resonator technology for GHz applications. In *Proceedings of the 2004 IEEE International Frequency Control Symposium and Exposition, 2004.* (pp. 27-34). IEEE.

[25] Lu, C., & Czanderna, A. W. (Eds.). (2012). *Applications of piezoelectric quartz crystal microbalances*. Elsevier.

[26] Grima, J. N., Gatt, R., Alderson, A., & Evans, K. E. (2005). On the origin of auxetic behaviour in the silicate α-cristobalite. *Journal of Materials Chemistry*, *15*(37), 4003-4005.

[27] Zheng, R., Ren, Z., Gao, H., Zhang, A., & Bian, Z. (2018). Effects of calcination on silica phase transition in diatomite. *Journal of Alloys and Compounds*, *757*, 364-371.

[28] Blanco, M. V., Renman, V., Vullum-Bruer, F., & Svensson, A. M. (2020). Nanostructured diatom earth SiO 2 negative electrodes with superior electrochemical performance for lithium ion batteries. *RSC advances*, *10*(55), 33490-33498.

[29] Aggrey, P., Salimon, A. I., Abdusatorov, B., Fedotov, S. S., & Korsunsky, A. M. (2020). The structure and phase composition of nano-silicon as a function of calcination conditions of diatomaceous earth. *Materials Today: Proceedings*, *33*, 1884-1892.

[30] Zhang, Y. X., Huang, M., Li, F., Wang, X. L., & Wen, Z. Q. (2014). One-pot synthesis of hierarchical MnO2-modified diatomites for electrochemical capacitor electrodes. *Journal of Power Sources*, *246*, 449-456.

[31] Ediz, N., Bentli, İ., & Tatar, İ. (2010). Improvement in filtration characteristics of diatomite by calcination. *International Journal of Mineral Processing*, *94*(3-4), 129-134.

[32] Sun, Z., Zhang, Y., Zheng, S., Park, Y., & Frost, R. L. (2013). Preparation and thermal energy storage properties of paraffin/calcined diatomite composites as form-stable phase change materials. *Thermochimica Acta*, *558*, 16-21.

[33] Xia, Y., Li, F., Jiang, Y., Xia, M., Xue, B., & Li, Y. (2014). Interface actions between TiO2 and porous diatomite on the structure and photocatalytic activity of TiO2-diatomite. *Applied surface science*, *303*, 290-296.

[34] Xu, B., & Li, Z. (2013). Paraffin/diatomite composite phase change material incorporated cement-based composite for thermal energy storage. *Applied energy*, *105*, 229-237.

[35] Qian, T., Li, J., & Deng, Y. (2016). Pore structure modified diatomite-supported PEG composites for thermal energy storage. *Scientific reports*, *6*(1), 1-14.

[36] Entwistle, J., Rennie, A., & Patwardhan, S. (2018). A review of magnesiothermic reduction of silica to porous silicon for lithium-ion battery applications and beyond. *Journal of Materials Chemistry A*, *6*(38), 18344-18356.

[37] Blanco, M. V., Renman, V., Vullum-Bruer, F., & Svensson, A. M. (2020). Nanostructured diatom earth SiO 2 negative electrodes with superior electrochemical performance for lithium ion batteries. *RSC advances*, *10*(55), 33490-33498.

[38] Xing, A., Tian, S., Tang, H., Losic, D., & Bao, Z. (2013). Mesoporous silicon engineered by the reduction of biosilica from rice husk as a high-performance anode for lithium-ion batteries. *RSC advances*, *3*(26), 10145-10149.

[39] Meng, G. W., Cui, Z., Zhang, L. D., & Phillipp, F. (2000). Growth and characterization of nanostructured β-SiC via carbothermal reduction of SiO2 xerogels containing carbon nanoparticles. *Journal of crystal growth*, *209*(4), 801-806.

[40] Qian, J. M., Wang, J. P., Qiao, G. J., & Jin, Z. H. (2004). Preparation of porous SiC ceramic with a woodlike microstructure by sol-gel and carbothermal reduction processing. *Journal of the European Ceramic Society*, *24*(10-11), 3251-3259.

[41] Weimer, A. W., Nilsen, K. J., Cochran, G. A., & Roach, R. P. (1993). Kinetics of carbothermal reduction synthesis of beta silicon carbide. *AIChE Journal*, *39*(3), 493-503.

[42] Xing, Z., Lu, J., & Ji, X. (2018). A brief review of metallothermic reduction reactions for materials preparation. *Small Methods*, *2*(12), 1800062.

[43] Aggrey, P., Nartey, M., Kan, Y., Cvjetinovic, J., Andrews, A., Salimon, A. I., ... & Korsunsky, A. M. (2021). On the diatomite-based nanostructure-preserving material synthesis for energy applications. *RSC advances*, *11*(51), 31884-31922.

[44] Setiawan, W. K., & Chiang, K. Y. (2021). Crop residues as potential sustainable precursors for developing silica materials: a review. *Waste and Biomass Valorization*, *12*(5), 2207-2236.

[45] Korsunsky, A. M., Sapozhnikov, P. V., Everaerts, J., & Salimon, A. I. (2019). Nature's neat nanostructuration: The fascinating frustules of diatom algae. *Materials Today*, *22*.

[46] Sağlam, Ö., Işıkber, A. A., Tunaz, H., Er, M. K., Bahadır, F., & Şen, R. (2017). Preliminary checking of some Turkish diatomaceous earth similarities with commercial diatomaceous earths under scanning electron microscope (SEM). *Tekirdağ Ziraat Fakültesi Dergisi*.

[47] Tang, X., Wen, G., & Song, Y. (2018). Novel scalable synthesis of porous silicon/carbon composite as anode material for superior lithium-ion batteries. *Journal of Alloys and Compounds*, *739*, 510-517.

[48] Wang, J., Liu, D. H., Wang, Y. Y., Hou, B. H., Zhang, J. P., Wang, R. S., & Wu, X. L. (2016). Dual-carbon enhanced silicon-based composite as superior anode material for lithium ion batteries. *Journal of Power Sources*, *307*, 738-745.

[49] Li, C., Wang, M., Xie, B., Ma, H., & Chen, J. (2020). Enhanced properties of diatomite-based composite phase change materials for thermal energy storage. *Renewable Energy*, *147*, 265-274.

[50] Konuklu, Y., Ersoy, O., Erzin, F., & Toraman, Y. Ö. (2019). Experimental study on preparation of lauric acid/microwave-modified diatomite phase change material composites. *Solar Energy Materials and Solar Cells*, *194*, 89-94.

[51] Wang, M. S., Fan, L. Z., Huang, M., Li, J., & Qu, X. (2012). Conversion of diatomite to porous Si/C composites as promising anode materials for lithium-ion batteries. *Journal of Power Sources*, *219*, 29-35.

[52] Campbell, B., Ionescu, R., Tolchin, M., Ahmed, K., Favors, Z., Bozhilov, K. N., ... & Ozkan, M. (2016). Carbon-coated, diatomite-derived nanosilicon as a high rate capable Li-ion battery anode. *Scientific Reports*, *6*(1), 1-9.

[53] Zhang, Y. X., Li, F., Huang, M., Xing, Y., Gao, X., Li, B., ... & Guan, Y. M. (2014). Hierarchical NiO moss decorated diatomites via facile and templated method for high performance supercapacitors. *Materials Letters*, *120*, 263-266.

[54] Li, K., Liu, X., Zheng, T., Jiang, D., Zhou, Z., Liu, C., ... & Losic, D. (2019). Tuning MnO_2 to FeOOH replicas with bio-template 3D morphology as electrodes for high performance asymmetric supercapacitors. *Chemical Engineering Journal*, *370*, 136-147.

[55] Szczech, J. R., & Jin, S. (2008). Mg_2Si nanocomposite converted from diatomaceous earth as a potential thermoelectric nanomaterial. *Journal of Solid State Chemistry*, *181*(7), 1565-1570.

[56] Korsunsky, A. M., Bedoshvili, Y. D., Cvjetinovic, J., Aggrey, P., Dragnevski, K. I., Gorin, D. A., ... & Likhoshway, Y. V. (2020). Siliceous diatom frustules–A smart nanotechnology platform. *Materials Today: Proceedings*, *33*, 2032-2040.

[57] Xu, B., & Li, Z. (2014). Paraffin/diatomite/multi-wall carbon nanotubes composite phase change material tailor-made for thermal energy storage cement-based composites. *Energy*, *72*, 371-380.

[58] Yılmaz, B., & Ediz, N. (2008). The use of raw and calcined diatomite in cement production. *Cement and Concrete Composites*, *30*(3), 202-211.

[59] Bao, Z., Weatherspoon, M. R., Shian, S., Cai, Y., Graham, P. D., Allan, S. M., ... & Sandhage, K. H. (2007). Chemical reduction of three-dimensional silica micro-assemblies into microporous silicon replicas. *Nature*, *446*(7132), 172-175.

[60] Gallego-Gómez, F., Ibisate, M., Golmayo, D., Palomares, F. J., Herrera, M., Hernández, J., ... & López, C. (2011). Light emission from nanocrystalline Si inverse opals and controlled passivation by atomic layer deposited Al_2O_3. *Advanced Materials*, *23*(44), 5219-5223.

[61] Richman, E. K., Kang, C. B., Brezesinski, T., & Tolbert, S. H. (2008). Ordered mesoporous silicon through magnesium reduction of polymer templated silica thin films. *Nano letters*, *8*(9), 3075-3079.

[62] Khripin, C. Y., Pristinski, D., Dunphy, D. R., Brinker, C. J., & Kaehr, B. (2011). Protein-directed assembly of arbitrary three-dimensional nanoporous silica architectures. *Acs Nano*, *5*(2), 1401-1409.

[63] Zhang, Y., & Huang, J. (2011). Hierarchical nanofibrous silicon as replica of natural cellulose substance. *Journal of Materials Chemistry*, *21*(20), 7161-7165.

[64] Yoo, J. K., Kim, J., Jung, Y. S., & Kang, K. (2012). Scalable fabrication of silicon nanotubes and their application to energy storage. *Advanced Materials*, *24*(40), 5452-5456.

[65] Lai, Y., Thompson, J. R., & Dasog, M. (2018). Metallothermic reduction of silica nanoparticles to porous silicon for drug delivery using new and existing reductants. *Chemistry–A European Journal*, *24*(31), 7913-7920.

[66] Cho, D., Kim, M., Hwang, J., Park, J. H., Joo, Y. L., & Jeong, Y. (2015). Facile synthesis of porous silicon nanofibers by magnesium reduction for application in lithium ion batteries. *Nanoscale research letters*, *10*(1), 1-8.

[67] Xie, J., Wang, G., Huo, Y., Zhang, S., Cao, G., & Zhao, X. (2014). Nanostructured silicon spheres prepared by a controllable magnesiothermic reduction as anode for lithium ion batteries. *Electrochimica Acta*, *135*, 94-100.

[68] Chen, K., Bao, Z., Du, A., Zhu, X., Wu, G., Shen, J., & Zhou, B. (2012). Synthesis of resorcinol–formaldehyde/silica composite aerogels and their low-temperature conversion to mesoporous silicon carbide. *Microporous and Mesoporous Materials*, *149*(1), 16-24.

[69] Liu, X., Gao, Y., Jin, R., Luo, H., Peng, P., & Liu, Y. (2014). Scalable synthesis of Si nanostructures by low-temperature magnesiothermic reduction of silica for application in lithium ion batteries. *Nano Energy*, *4*, 31-38.

[70] Larbi, K. K., Barati, M., & McLean, A. (2011). Reduction behaviour of rice husk ash for preparation of high purity silicon. *Canadian Metallurgical Quarterly*, *50*(4), 341-349.

[71] Liu, N., Huo, K., McDowell, M. T., Zhao, J., & Cui, Y. (2013). Rice husks as a sustainable source of nanostructured silicon for high performance Li-ion battery anodes. *Scientific reports*, *3*(1), 1-7.

[72] Wu, H., Du, N., Shi, X., & Yang, D. (2016). Rational design of three-dimensional macroporous silicon as high performance Li-ion battery anodes with long cycle life. *Journal of Power Sources*, *331*, 76-81.

[73] Shi, L., Wang, W., Wang, A., Yuan, K., & Yang, Y. (2016). Understanding the impact mechanism of the thermal effect on the porous silicon anode material preparation via magnesiothermic reduction. *Journal of Alloys and Compounds*, *661*, 27-37.

[74] Chen, W., Fan, Z., Dhanabalan, A., Chen, C., & Wang, C. (2011). Mesoporous silicon anodes prepared by magnesiothermic reduction for lithium ion batteries. *Journal of The Electrochemical Society*, *158*(9), A1055.

[75] Batchelor, L., Loni, A., Canham, L. T., Hasan, M., & Coffer, J. L. (2012). Manufacture of mesoporous silicon from living plants and agricultural waste: an environmentally friendly and scalable process. *Silicon*, *4*(4), 259-266.

[76] Luo, W., Wang, X., Meyers, C., Wannenmacher, N., Sirisaksoontorn, W., Lerner, M. M., & Ji, X. (2013). Efficient fabrication of nanoporous Si and Si/Ge enabled by a heat scavenger in magnesiothermic reactions. *Scientific reports*, *3*(1), 1-7.

[77] Wang, W., Favors, Z., Ionescu, R., Ye, R., Bay, H. H., Ozkan, M., & Ozkan, C. S. (2015). Monodisperse porous silicon spheres as anode materials for lithium ion batteries. *Scientific reports*, *5*(1), 1-6.

[78] Li, C., Liu, C., Wang, W., Mutlu, Z., Bell, J., Ahmed, K., ... & Ozkan, C. S. (2017). Silicon derived from glass bottles as anode materials for lithium ion full cell batteries. *Scientific reports*, *7*(1), 1-11.

[79] Favors, Z., Wang, W., Bay, H. H., Mutlu, Z., Ahmed, K., Liu, C., ... & Ozkan, C. S. (2014). Scalable synthesis of nano-silicon from beach sand for long cycle life Li-ion batteries. *Scientific reports*, *4*(1), 1-7.

[80] Liu, S., Liu, B., Yao, Y., Dong, P., & Zhao, S. (2016). Effect of pore structures on the electrochemical performance of porous silicon synthesized from magnesiothermic reduction of biosilica. *Journal of Wuhan University of Technology-Mater. Sci. Ed.*, *31*(5), 965-971.

[81] Liang, J., Li, X., Hou, Z., Zhang, W., Zhu, Y., & Qian, Y. (2016). A deep reduction and partial oxidation strategy for fabrication of mesoporous Si anode for lithium ion batteries. *ACS nano*, *10*(2), 2295-2304.

[82] Sim, S., Oh, P., Park, S., & Cho, J. (2013). Critical thickness of SiO 2 coating layer on Si anode materials for Li-ion batteries. *Adv. Mater*, *25*(32), 4498-4503.

[83] Lepoivre, F., Larcher, D., & Tarascon, J. M. (2016). Electrochemical activation of silica for enhanced performances of Si-based electrodes. *Journal of The Electrochemical Society*, *163*(13), A2791.

[84] Choi, S., Bok, T., Ryu, J., Lee, J. I., Cho, J., & Park, S. (2015). Revisit of metallothermic reduction for macroporous Si: compromise between capacity and volume expansion for practical Li-ion battery. *Nano Energy*, *12*, 161-168.

[85] Sternad, M., Forster, M., & Wilkening, M. (2016). The microstructure matters: breaking down the barriers with single crystalline silicon as negative electrode in Li-ion batteries. *Scientific Reports*, *6*(1), 1-8.

[86] Sternad, M., Hirtler, G., Sorger, M., Knez, D., Karlovsky, K., Forster, M., & Wilkening, H. M. R. (2022). A Lithium-Silicon Microbattery with Anode and Housing Directly Made from Semiconductor Grade Monocrystalline Si. *Advanced Materials Technologies*, *7*(3), 2100405.

[87] Ali, I., Tippabhotla, S. K., Radchenko, I., Al-Obeidi, A., Stan, C. V., Tamura, N., & Budiman, A. S. (2018). Probing stress states in silicon nanowires during electrochemical lithiation using in situ synchrotron X-ray microdiffraction. *Frontiers in Energy Research*, *6*, 19.

[88] Lee, I. J., Paik, U., & Park, J. G. (2013). Solar cell implemented with silicon nanowires on pyramid-texture silicon surface. *Solar Energy*, *91*, 256-262.

[89] Chen, Q., Liu, Y., Wang, Y., Chen, W., Wu, J., Zhao, Y., & Du, X. (2019). Optical properties of a random inverted pyramid textured silicon surface studied by the ray tracing method. *Solar Energy*, *186*, 392-397.

[90] Iyengar, V. V., Nayak, B. K., More, K. L., Meyer III, H. M., Biegalski, M. D., Li, J. V., & Gupta, M. C. (2011). Properties of ultrafast laser textured silicon for photovoltaics. *Solar Energy Materials and solar cells*, *95*(10), 2745-2751.

[91] Zhu, S., Sun, H., Liu, X., Zhuang, J., & Zhao, L. (2017). Room-temperature NH3 sensing of graphene oxide film and its enhanced response on the laser-textured silicon. *Scientific reports*, *7*(1), 1-8.

[92] Moshnikov, V. A., Gracheva, I., Lenshin, A. S., Spivak, Y. M., Anchkov, M. G., Kuznetsov, V. V., & Olchowik, J. M. (2012). Porous silicon with embedded metal oxides for gas sensing applications. *Journal of non-crystalline solids*, *358*(3), 590-595.

[93] Sun, N., Ma, X., Su, Y., Jiang, P., Zou, Y., & Zhou, D. (2019). TiN thin film electrodes on textured silicon substrates for supercapacitors. *Journal of The Electrochemical Society*, *166*(15), H802.

[94] Shaik, D. P., Rosaiah, P., & Hussain, O. M. (2019). Fabrication of the Mn3O4 thin film electrodes by electron beam evaporation for supercapacitor applications. *Journal of Electroanalytical Chemistry*, *851*, 113409.

[95] Liu, X., Coxon, P. R., Peters, M., Hoex, B., Cole, J. M., & Fray, D. J. (2014). Black silicon: fabrication methods, properties and solar energy applications. *Energy & Environmental Science*, *7*(10), 3223-3263.

[96] Guillen, G. R., Pan, Y., Li, M., & Hoek, E. M. (2011). Preparation and characterization of membranes formed by nonsolvent induced phase separation: a review. *Industrial & Engineering Chemistry Research*, *50*(7), 3798-3817.

[97] Kuo, C. Y., Lin, H. N., Tsai, H. A., Wang, D. M., & Lai, J. Y. (2008). Fabrication of a high hydrophobic PVDF membrane via nonsolvent induced phase separation. *Desalination*, *233*(1-3), 40-47.

[98] Tanaka, T., & Lloyd, D. R. (2004). Formation of poly (L-lactic acid) microfiltration membranes via thermally induced phase separation. *Journal of membrane science*, *238*(1-2), 65-73.

[99] Gu, M., Zhang, J., Wang, X., Tao, H., & Ge, L. (2006). Formation of poly (vinylidene fluoride)(PVDF) membranes via thermally induced phase separation. *Desalination*, *192*(1-3), 160-167.

[100] Lee, J. P., Choi, S., & Park, S. (2012). Preparation of silica nanospheres and porous polymer membranes with controlled morphologies via nanophase separation. *Nanoscale research letters*, *7*(1), 1-7.

[101] Branz, H. M., Yost, V. E., Ward, S., Jones, K. M., To, B., & Stradins, P. (2009). Nanostructured black silicon and the optical reflectance of graded-density surfaces. *Applied Physics Letters*, *94*(23), 231121.

[102] Savin, H., Repo, P., Von Gastrow, G., Ortega, P., Calle, E., Garín, M., & Alcubilla, R. (2015). Black silicon solar cells with interdigitated back-contacts achieve 22.1% efficiency. *Nature nanotechnology*, *10*(7), 624-628.

[102] Xia, Y., Liu, B., Liu, J., Shen, Z., & Li, C. (2011). A novel method to produce black silicon for solar cells. *Solar energy*, *85*(7), 1574-1578.

[103] Ma, L. L., Zhou, Y. C., Jiang, N., Lu, X., Shao, J., Lu, W., ... & Hou, X. Y. (2006). Wide-band "black silicon" based on porous silicon. *Applied physics letters*, *88*(17), 171907.

[104] Wang, Y., Liu, Y. P., Liang, H. L., Mei, Z. X., & Du, X. L. (2013). Broadband antireflection on the silicon surface realized by Ag nanoparticle-patterned black silicon. *Physical Chemistry Chemical Physics*, *15*(7), 2345-2350.

[105] Lu, Y. T., & Barron, A. R. (2013). Nanopore-type black silicon anti-reflection layers fabricated by a one-step silver-assisted chemical etching. *Physical Chemistry Chemical Physics*, *15*(24), 9862-9870.

[106] Zhao, Z., Li, P., Wei, Y., Lu, C., Tan, X., & Liu, A. (2014). 17.3% efficient black silicon solar cell without dielectric antireflection coating. *Solar energy*, *110*, 714-719.

[107] Ren, Z., Gao, H., Zhang, H., & Liu, X. (2014). Effects of fluxes on the structure and filtration properties of diatomite filter aids. *International Journal of Mineral Processing*, *130*, 28-33.

[108] Ibrahim, S. S., & Selim, A. Q. (2010). Producing a micro-porous diatomite by a simple classification-calcinations process. *The Journal of Ore Dressing*, *12*(23), 24-32.

[109] Kan, Y., Salimon, A. I., Sapozhnikov, P. V., Somov, P. A., Everaerts, J., & Korsunsky, A. M. (2019). On the fabrication of diatomite earth-based ceramics with multiscale porosity. In *Lecture Notes in Engineering and Computer Science* (pp. 310-317).

[110] Ersoy, O., Rençberoğlu, M., Karapınar Güler, D., & Özkaya, Ö. F. (2022). A Novel Flux That Determines the Physico-Chemical Properties of Calcined Diatomite in Its Industrial Use as a Filler and Filter Aid: Thenardite (Na2SO4). *Crystals*, *12*(4), 503.

[111] Jing, C., Liu, X., Liu, X., Jiang, D., Dong, B., Dong, F., ... & Zhang, Y. (2018). Crystal morphology evolution of Ni–Co layered double hydroxide nanostructure towards high-performance biotemplate asymmetric supercapacitors. *CrystEngComm*, *20*(46), 7428-7434.

[112] Inglethorpe, S. D. J., Morgan, D. J., Highley, D. E., & Bloodworth, A. J. (1993). *Industrial Minerals laboratory manual: bentonite*. British Geological Survey, Mineralogy and Petrology Group.

[113] Hollemann, A. F., & Wiberg, E. (1985). Lehrbuch der Anorganischen Chemie, 91.-100. Aufl., S. 1189.

[114] Di, F., Wang, N., Li, L., Geng, X., Yang, H., Zhou, W., ... & An, B. (2021). Coral-like porous composite material of silicon and carbon synthesized by using diatomite as self-template and precursor with a good performance as anode of lithium-ions battery. *Journal of Alloys and Compounds*, *854*, 157253.

[115] Le, Q. J., Wang, T., Tran, D. N., Dong, F., Zhang, Y. X., & Losic, D. (2017). Morphology-controlled MnO 2 modified silicon diatoms for high-performance asymmetric supercapacitors. *Journal of Materials Chemistry A*, *5*(22), 10856-10865.

[116] Sun, Z., Bai, C., Zheng, S., Yang, X., & Frost, R. L. (2013). A comparative study of different porous amorphous silica minerals supported TiO2 catalysts. *Applied Catalysis A: General*, *458*, 103-110.

[117] Li, H., Zhang, Q., Yap, C. C. R., Tay, B. K., Edwin, T. H. T., Olivier, A., & Baillargeat, D. (2012). From bulk to monolayer MoS2: evolution of Raman scattering. *Advanced Functional Materials*, *22*(7), 1385-1390.

[118] Zuo, Z., Zhang, S., Wang, Y., Guo, Y., Sun, L., Li, K., & Cui, G. (2019). Effective plasmon coupling in conical cavities for sensitive surface enhanced Raman scattering with quantitative analysis ability. *Nanoscale*, *11*(38), 17913-17919.

[119] Stephens, R. B., & Cody, G. D. (1977). Optical reflectance and transmission of a textured surface. *Thin Solid Films*, *45*(1), 19-29.

[120] Ikusika, O. O., Mpendulo, C. T., Zindove, T. J., & Okoh, A. I. (2019). Fossil shell flour in livestock production: A Review. *Animals*, *9*(3), 70.

[121] Liang, J., Li, X., Hou, Z., Guo, C., Zhu, Y., & Qian, Y. (2015). Nanoporous silicon prepared through air-oxidation demagnesiation of Mg 2 Si and properties of its lithium ion batteries. *Chemical Communications*, *51*(33), 7230-7233.

[122] Liu, N., Huo, K., McDowell, M. T., Zhao, J., & Cui, Y. (2013). Rice husks as a sustainable source of nanostructured silicon for high performance Li-ion battery anodes. *Scientific reports*, *3*(1), 1919.

[123] Shang, H., Lu, Y., Zhao, F., Chao, C., Zhang, B., & Zhang, H. (2015). Preparing high surface area porous carbon from biomass by carbonization in a molten salt medium. *RSC advances*, *5*(92), 75728-75734.

[124] Wang, Y., Feng, Z., Zhu, W., Gariépy, V., Gagnon, C., Provencher, M., ... & Zaghib, K. (2018). High capacity and high efficiency maple tree-biomass-derived hard carbon as an anode material for sodium-ion batteries. *Materials*, *11*(8), 1294.

[125] Kumar, R., Sahu, G., Saxena, S. K., Rai, H. M., & Sagdeo, P. R. (2014). Qualitative evolution of asymmetric Raman line-shape for nanostructures. *Silicon*, *6*, 117-121.

[126] Shah, A., Stenberg, P., Karvonen, L., Ali, R., Honkanen, S., Lipsanen, H., ... & Kaplas, T. (2016). Pyrolytic carbon coated black silicon. *Scientific reports*, *6*(1), 25922.

[127] Nakaya, H., Nishida, M., Takeda, Y., Moriuchi, S., Tonegawa, T., Machida, T., & Nunoi, T. (1994). Polycrystalline silicon solar cells with V-grooved surface. *Solar energy materials and solar cells*, *34*(1-4), 219-225.

[128] Park, H., Kwon, S., Lee, J. S., Lim, H. J., Yoon, S., & Kim, D. (2009). Improvement on surface texturing of single crystalline silicon for solar cells by saw-damage etching using an acidic solution. *Solar Energy Materials and Solar Cells*, *93*(10), 1773-1778.

[129] Steglich, M., Lehr, D., Ratzsch, S., Käsebier, T., Schrempel, F., Kley, E. B., & Tünnermann, A. (2014). An ultra-black silicon absorber. *Laser & Photonics Reviews*, *8*(2), L13-L17.

[130] Yoo, J. S., Parm, I. O., Gangopadhyay, U., Kim, K., Dhungel, S. K., Mangalaraj, D., & Yi, J. (2006). Black silicon layer formation for application in solar cells. *Solar energy materials and solar cells*, *90*(18-19), 3085-3093.

[131] Da Silva, D. S., Côrtes, A. D. S., Oliveira Jr, M. H., Motta, E. F., Viana, G. A., Mei, P. R., & Marques, F. C. (2011). Application of amorphous carbon based materials as antireflective coatings on crystalline silicon solar cells. *Journal of Applied Physics*, *110*(4), 043510.

[132] Mahadik, D. B., Lakshmi, R. V., & Barshilia, H. C. (2015). High performance single layer nano-porous antireflection coatings on glass by sol–gel process for solar energy applications. *Solar Energy Materials and Solar Cells*, *140*, 61-68.

[133] Hiller, J. A., Mendelsohn, J. D., & Rubner, M. F. (2002). Reversibly erasable nanoporous anti-reflection coatings from polyelectrolyte multilayers. *Nature materials*, *1*(1), 59-63.

[134] Mizoshita, N., Ishii, M., Kato, N., & Tanaka, H. (2015). Hierarchical nanoporous silica films for wear resistant antireflection coatings. *ACS applied materials & interfaces*, *7*(34), 19424-19430.

[135] Xia, B., Luo, J., Li, Y., Yang, B., & Zhang, S. (2017). Preparation of sponge-like porous SiO 2 antireflective coatings with excellent environment-resistance by an acid-catalysed sol–gel method. *RSC advances*, *7*(43), 26834-26838.

[136] Agustín-Sáenz, C., Sánchez-García, J. Á., Machado, M., Brizuela, M., Zubillaga, O., & Tercjak, A. (2018). Broadband antireflective coating stack based on mesoporous silica by acid-catalyzed sol-gel method for concentrated photovoltaic application. *Solar Energy Materials and Solar Cells*, *186*, 154-164.

[137] Gurav, A. B., Latthe, S. S., Kappenstein, C., Mukherjee, S. K., Rao, A. V., & Vhatkar, R. S. (2011). Porous water repellent silica coatings on glass by sol–gel method. *Journal of Porous Materials*, *18*, 361-367.

[138] Wu, G., Wang, J., Shen, J., Yang, T., Zhang, Q., Zhou, B., ... & Zhang, F. (2000). A novel route to control refractive index of sol-gel derived nano-porous silica films used as broadband antireflective coatings. *Materials Science and Engineering: B*, *78*(2-3), 135-139.

[139] Vincent, A., Babu, S., Brinley, E., Karakoti, A., Deshpande, S., & Seal, S. (2007). Role of catalyst on refractive index tunability of porous silica antireflective coatings by sol− gel technique. *The Journal of Physical Chemistry C*, *111*(23), 8291-8298.

[140] Cai, S., Zhang, Y., Zhang, H., Yan, H., Lv, H., & Jiang, B. (2014). Sol–gel preparation of hydrophobic silica antireflective coatings with low refractive index by base/acid two-step catalysis. *ACS applied materials & interfaces*, *6*(14), 11470-11475.

[141] Chen, J., Wang, B., Yang, Y., Shi, Y., Xu, G., & Cui, P. (2012). Porous anodic alumina with low refractive index for broadband graded-index antireflection coatings. *Applied optics*, *51*(28), 6839-6843.

[142] Stetsenko, M., Pullano, S. A., Margitych, T., Maksimenko, L., Hassan, A., Kryvyi, S., ... & Fiorillo, A. S. (2019). Antireflection enhancement by composite nanoporous zeolite 3A–carbon thin film. *Nanomaterials*, *9*(11), 1641.

[143]Chen, C. H., Li, S. Y., Chiang, A. S., Wu, A. T., & Sun, Y. S. (2011). Scratch-resistant zeolite anti-reflective coating on glass for solar applications. *Solar energy materials and solar cells*, *95*(7), 1694-1700.

[144] Raut, H. K., Dinachali, S. S., Ansah-Antwi, K. K., Ganesh, V. A., & Ramakrishna, S. (2013). Fabrication of highly uniform and porous MgF2 anti-reflective coatings by polymer-based sol–gel processing on large-area glass substrates. *Nanotechnology*, *24*(50), 505201.

[145] Rad, A. S., Afshar, A., & Azadeh, M. (2020). Anti-reflection and self-cleaning meso-porous TiO2 coatings as solar systems protective layer: Investigation of effect of porosity and roughness. *Optical Materials*, *107*, 110027.

[146] Gupta, K., Lin, J. T., Wang, R. C., & Liu, C. P. (2016). Porosity-induced full-range visible-light photodetection via ultrahigh broadband antireflection in ZnO nanowires. *NPG Asia Materials*, *8*(9), e314-e314.

[147] Kumar, A., Yerva, S. V., & Barshilia, H. C. (2016). Broadband and wide angle anti-reflective nanoporous surface on poly (ethylene terephthalate) substrate using a single step plasma etching for applications in flexible electronics. *Solar Energy Materials and Solar Cells*, *155*, 184-193.

[148] Zhan, Z., Zheng, L., Pan, Y., Sun, G., & Li, L. (2012). Self-powered, visible-light photodetector based on thermally reduced graphene oxide–ZnO (rGO–ZnO) hybrid nanostructure. *Journal of Materials Chemistry*, *22*(6), 2589-2595.

[149] Zheng, Z., Gan, L., Li, H., Ma, Y., Bando, Y., Golberg, D., & Zhai, T. (2015). A fully transparent and flexible ultraviolet–visible photodetector based on controlled electrospun ZnO-CdO heterojunction nanofiber arrays. *Advanced Functional Materials*, *25*(37), 5885-5894.

[150] Zhu, L., Li, C., Li, Y., Feng, C., Li, F., Zhang, D., ... & Ruan, S. (2015). Visible-light photodetector with enhanced performance based on a ZnO@ CdS heterostructure. *Journal of Materials Chemistry C*, *3*(10), 2231-2236.

[151] Suzuki, M., Yamamoto, T., Katayama, Y., Kuwata, S., & Tanaka, T. (2012). Light absorption by metals with porous surface layer formed by oxidization–reduction treatment. *Materials Transactions*, *53*(9), 1556-1562.

[152] De Nicola, F., Hines, P., De Crescenzi, M., & Motta, N. (2016). Moth-eye effect in hierarchical carbon nanotube anti-reflective coatings. *Carbon*, *108*, 262-267.

[153] Kacha, K., Djeffal, F., Ferhati, H., Bendjerad, A., Benhaya, A., & Saidi, A. (2022). Broadband spectral photodetector based on all-amorphous ZnO/Si heterostructure incorporating Ag intermediate thin-films. *Optical Materials*, *130*, 112578.

[154] Firooz, A. A., Mirzaie, R. A., & Kamrani, F. (2018). Effect of morphological ZnO nanostructures on the optical and decolorization properties. *Journal of Structural Chemistry*, *59*, 739-743.

[155] Yu, J., Gao, J., Xue, F., Yu, X., Yu, H., Dong, X., ... & Cao, G. (2015). Formation mechanism and optical characterization of polymorphic silicon nanostructures by DC arc-discharge. *RSC Advances*, *5*(84), 68714-68721.

[156] Takagahara, T., & Takeda, K. (1992). Theory of the quantum confinement effect on excitons in quantum dots of indirect-gap materials. *Physical Review B*, *46*(23), 15578.

[157] Kang, Z., Tsang, C. H. A., Zhang, Z., Zhang, M., Wong, N. B., Zapien, J. A., ... & Lee, S. T. (2007). A polyoxometalate-assisted electrochemical method for silicon nanostructures preparation: from quantum dots to nanowires. *Journal of the American Chemical Society*, *129*(17), 5326-5327.

[158] Kim, U., Kim, I., Park, Y., Lee, K. Y., Yim, S. Y., Park, J. G., ... & Choi, H. J. (2011). Synthesis of Si nanosheets by a chemical vapor deposition process and their blue emissions. *Acs Nano*, *5*(3), 2176-2181.

[159] Height, H. E., Apblett, C. A., & Collins, S. D. (2016, April). Chemically Etched Silicon Nanowires As Anodes for Lithium-Ion Batteries. In *Electrochemical Society Meeting Abstracts 229* (No. 2, pp. 348-348). The Electrochemical Society, Inc..

[160] Sternad, M., Forster, M., & Wilkening, M. (2016). The microstructure matters: breaking down the barriers with single crystalline silicon as negative electrode in Li-ion batteries. *Scientific Reports*, *6*(1), 1-8.

[161] Ge, M., Rong, J., Fang, X., & Zhou, C. (2012). Porous doped silicon nanowires for lithium ion battery anode with long cycle life. *Nano letters*, *12*(5), 2318-2323.

[162] Vlad, A., Reddy, A. L. M., Ajayan, A., Singh, N., Gohy, J. F., Melinte, S., & Ajayan, P. M. (2012). Roll up nanowire battery from silicon chips. *Proceedings of the National Academy of Sciences*, *109*(38), 15168-15173.

[163] Putwa, S., Curtis, I. S., & Dasog, M. (2023). Nanostructured silicon photocatalysts for solar-driven fuel production. *Iscience*, *26*(4).